UNIVERSITY OF COPENHAGEN
FACULTY OF SCIENCE

PhD thesis

Caroline Lindberg

Growth of Ag-seeded III-V nanowires and TEM characterization

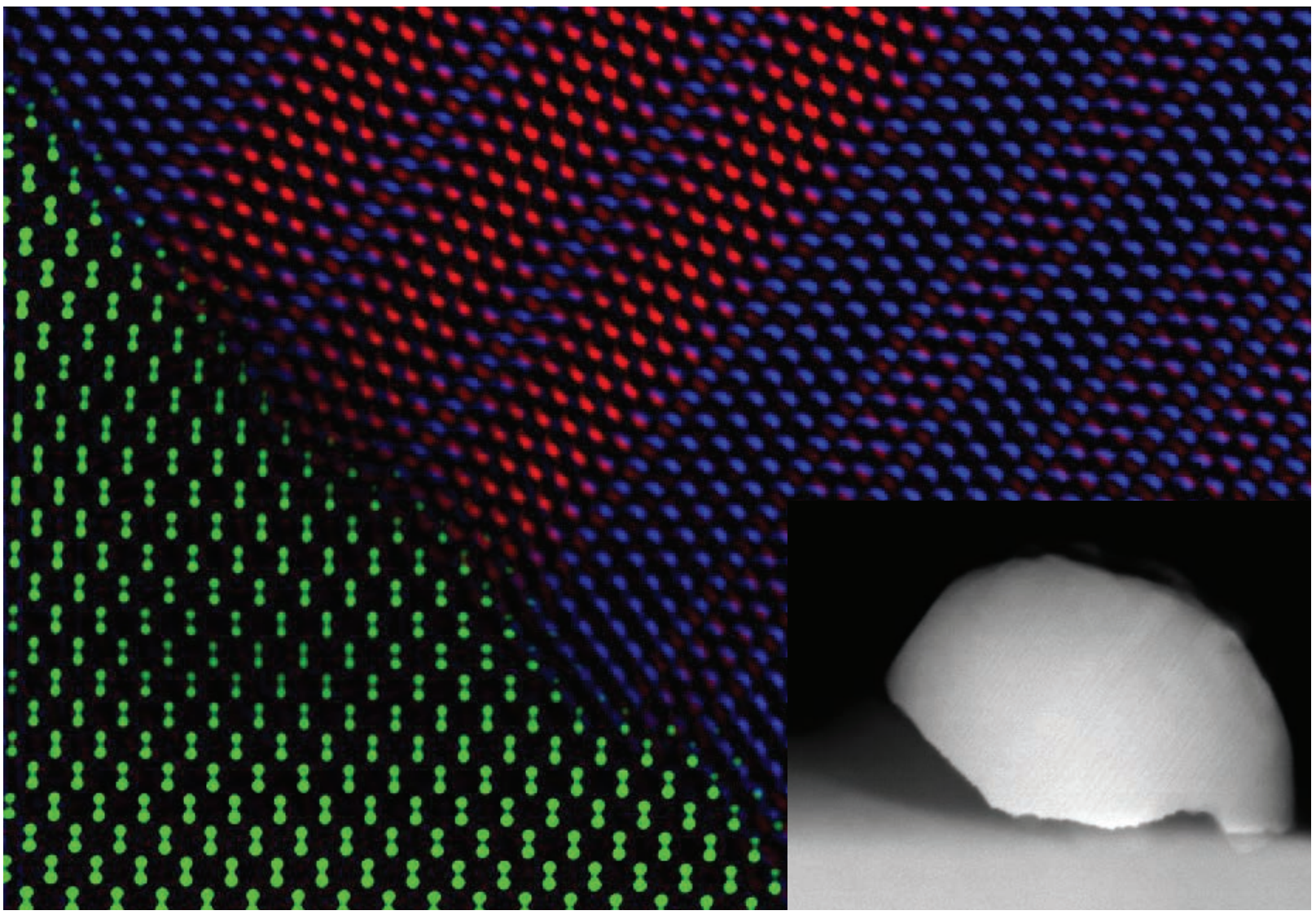

Supervisors: Jessica Bolinsson & Jesper Nygård
Submitted on: March 2017

This thesis has been submitted to the PhD school of The Faculty of Science, University of Copenhagen, Denmark

Front page: Large image, falsely colored, deconvoluted Cs corrected HAADF-STEM image over a newly nucleated GaAs nanowire and the Ag seed particle on a GaAs(100) substrate. Small image, TEM overview over the same nanowire. In courtesy of Jordi Arbiol, Institut Català de Nanociència i Nanotecnologia (ICN2), Bellaterra, Catalonia, Spain, the images are acquired at the Advanced Microscopy Laboratory (LMA) in Institute of Nanoscience of Aragon (INA), Zaragoza, Spain.

Growth of Ag-seeded III-V nanowires and TEM characterization

Caroline Lindberg

PhD thesis

Center for Quantum Devices

&

Nano Science Center

Niels Bohr Institute

Faculty of Science

Copenhagen University

Academic Advisors

Pr. Jesper Nygård & Dr. Jessica Bolinsson

March 2017

Abstract

This thesis deals with growth and characterization of GaAs and InAs nanowires. Today Au nanoparticle-seeding together with self-catalyzing are the dominating techniques to grow III-V nanowires with molecular beam epitaxy. In this thesis we instead investigate the possibility to use Ag as seed particle for growth of GaAs and InAs nanowires. The aim with the experiments performed has been to conclude whether Ag can be used to nucleate and grow nanowires on III-V substrates with molecular beam epitaxy. To investigate this we have performed growths of GaAs nanowires on GaAs(111)B and GaAs(100) substrates as well as growths of InAs nanowires on InAs(111)B substrates. We have used a wide range of the basic growth parameters, such as temperature, As-pressure and group III-flux, in order to find good growth conditions for the Ag-seeded nanowires. The overall growths have been evaluated with SEM and, when appropriate, the density and the vertical yield were obtained. The crystal structures for the grown nanowires have been investigated with TEM. We have also performed additional growths to further understand exactly how the nanowire growth proceeds as well as to understand the limitations of using Ag as a seed particle.

The last chapter presents our results from combining TEM and Raman spectroscopy to evaluate the possibility to use Raman spectroscopy to find stacking faults and crystal defects in GaAs and InAs wurtzite nanowires. We performed TEM on both InAs nanowires and GaAs nanowires to deduce the stacking fault/crystal defect density and the results were then compared to Raman spectroscopy on the nanowires.

Svenskt abstrakt

Denna avhandling handlar främst om växt och karaktärisering av GaAs- och InAs-nanotrådar. De vanligaste metoderna för att växa nanotrådar med molecular beam epitaxy är att antingen använda Au som katalysator eller en självkatalyserande metod där en partikel av det aktuella grupp III-materialet används som katalyspartikel. I den här avhandlingen har vi undersökt möjligheten att använda Ag för att initiera och växa GaAs- och InAs-nanotrådar. För att identifiera en lyckad kombination av växtparametrar har alla de vanligaste växtparametrarna varierats. Dessa inkluderar växttemperaturen, As-trycket och grupp III-flödet. SEM har använts för en övergripande analys av nanotrådarna och när det varit relevant har SEM använts både för att bestämma densiteten och andelen vertikala nanotrådar på de olika proverna. TEM har använts för att finna kristallstrukturen för de olika nanotrådarna. Vi har också utfört ytterligare växter särskilt inriktade mot att öka förståelsen för hur Ag-katalyserade nanotrådar växer och för att förstå eventuella begränsningar.

Sista kapitlet handlar om hur man kan kombinera TEM och Raman-spektroskopi för att undersöka om Raman-spektroskopi kan användas för att hitta kristalldefekter i InAs- och GaAs-nanotrådar av wurtzitstruktur. Vi utförde TEM på både InAs- och GaAs-nanotrådar. TEM-bilderna användes för att analysera densiteten på kristalldefekterna. Resultaten från TEM:et jämfördes senare med resultaten från Raman-spektroskopin.

Contents

Acknowledgement

There are many people that I would like to thank for the last three years. Firstly, I would like to thank my supervisors Jesper Nygård and Jessica Bolinsson for letting me do this work, always prepared to listen to what I have to say and give their particular insights. I would especially like to thank Jessica for letting me work in the Ag-project. I would also like to thank Rawa Tanta for always having the possibility to come to your office and chat over a cup of tea or coffee and talk about all the special things it means to be a PhD student. Your friendship is very valuable to me. I would also like to thank Shiv, Nader and Claus for always taking the time to discuss the science, techniques and the machines including all the instrument's possibilities and limitations. A special thank you goes to all our HR people; your support in all practical matters and official documents are indispensable, I would waste so much more time on travel bills and similar without you. I would also like to thank everyone else at Qdev that I have ever discussed science with, taken a coffee with or just chat with.

Within the projects I would like to thank Alexander Whiticar, Jessica Bolinsson and Anders Björlig for a great collaboration within the Ag-seeded nanowires projects. And thank you Erik for the time spent in Risø for teaching me the CM20 microscope and for answering all my questions about TEM. That I did not have time to fully use your expertise is one of my regrets.

For my wonderful time in Barcelona I would like to thank Jordi Arbiol for letting me visit your lab and for providing me with a deeper knowledge on the possibilities with TEM and TEM techniques. Also thank you for letting me join you in Zaragoza, Spain; the images acquired there are probably my favourites during my whole PhD. Also thanks to Martha Sara Martí Sánchez for all the lovely TEM images and showing me how you are analyzing TEM data in your group. I would also like to thank Fransisco Belarre without whom the cross-section samples would not exist. I truly enjoyed my visit in your labs.

I would also like to thank all my friends outside of Copenhagen for your support and encouements. Outside of science I would like to thank my family for always being there when things are tough and always liking me for exactly the person that I am. I would also like to thank everyone at Malmö Budoklubb, thank you for always giving me a break from research and theories, and literally letting me kick away my frustrations every now and then. A special thank you goes to Zakaria for always being such a good friend.

Lastly, thank you my wonderful -soon to be husband- Christian; in many ways this is not my work but ours! I am so thankful for your support during these years. For the hours you have discussed and proof read my thesis and posters. Especially I would like to thank you for your thoruogh support and unconditional belief in me.

Chapter 1

Introduction

With the work presented in this thesis I am finishing my PhD at Copenhagen University. The thesis is divided into two separate parts; in the first part I will explain some relevant theories and techniques for nanowire growth. This includes chapter 2 where I will explain some of the basic concepts behind particle-seeded nanowire growth and how we can fabricate the particles used. I will also explain the theory behind molecular beam epitaxy. In chapter 3, I will explain how scanning electron microscopy and transmission electron microscopy work and why electron microscopy is important in the nanoscience field. The second part of the thesis presents the results from some of the different projects that I have been involved in during my time as a PhD student. In chapter 4, I present results on Ag-seeded GaAs nanowire growth. In chapter 5, I present our results on Ag-seeded InAs nanowire growth and lastly in chapter 6, I present some results for the project where we investigate how Raman spectroscopy can be used to evaluate the density of crystal defects in InAs and GaAs nanowires. But first things first, why are we intrested in nanowires and their seed particles at all?

Nanowires are small rods with a diameter in the size range of ten to hundreds of nanometers while the third dimension (the length) can be several micrometers. The small dimensions of nanowires make them highly interesting for today's semiconductor industry in the active search for smaller and smaller electronic components and many proof-of-principle devices have already been shown. For example, III-V nanowires have been used in optoelectronics devices [1, 2], transistors in different configurations [3, 4] and gas sensing devices [5, 6, 7]. Except for the electronics industry III-V nanowires have also proven useful in biological applications [8, 9].

Some common instruments for controlled epitaxial growth of III-V nanowires are molecular beam epitaxy (MBE) [10, 11], chemical beam epitaxy (CBE) [12] and metal-organic-vapor-phase-epitaxy (MOVPE) [13, 14]. All of the different techniques have their own possibilities and limitations. For example the MBE, with its good vaccuum and the absence of precursors, is a very clean system which keeps any contamination to a minimum. MOVPE, which utilizes precursors, is a dirtier system but it is also cheaper and have a higher throughput than the MBE [15].

Today III-V nanowires are grown with mainly three different approaches. The most common is particle-seeded growth with, most often, a Au nanoparticle as seed. The other two approaches are selective area epitaxy (SEA), where parts of the substrate are covered in order to promote lateral growth at the other areas, and self-catalyzed (SC)

nanowires where the group III material is used as seed particle [16]. The use of Au as seed particle has prove to be a good way to control both the crystal structure, diameter and the position of the nanowires [16]. Unfortunately Au still has some drawbacks. Au forms deep hole trapping defects in both bulk Si [17] and Si nanowires [18]. This is a problem since Si is the most commonly used material in the electronics today and the defects affect the electronic properties yielding that Au is forbidden in MOSFET processing [16]. It has also proved difficult to control the crystal direction of the growth; III-V nanowires generally prefer the <111>B growth direction and other growth directions are rare [19].

Recently the possibility to use other, foreign particles than Au has attracted more interest [16]. Using other particles than Au might solve the problem with trapping defects in Si when integrating the nanowire field to the existing semiconductor industry. It might also open up new growth parameters and thereby new properties of the nanowires [16]. One advantage that has already been proven possible with other other seed particles is controlled growth of nanowires in other directions than the common <111>B. Pd-seeded InAs nanowires have been shown to grow in the <110> [20] and <111>A [21, 22] directions. Fe-seeded GaAs nanowhiskers can grow in the <100> and <110> directions [23]. One desirable property is growth of vertical III-V nanowires on (100) substrates. The (100) substrates are attractive since this is the most common substrate in the electronics industry today. Even though a high yield (> 80 %) of vertical Au-seeded III-V nanowires on (100) substrates has been demonstrated [24, 25], an even higher yield of vertical nanowires usually requires either special surface treatments [14, 26] or tuning of the catalyst droplet [27]. Growing nanowires in more exotic directions can also be an easy way to control the crystal structure. This since the switching between wurtzite and zincblende is strongly correlated with the <111> direction [2]. New seed materials might also open up for easier growth of higher order crystal structures such as 4H [28]. Incorporation of magnetic seed-particles, such as Mn, into the nanowire has also been suggested to lead to magnetic nanowires [29].

Alloys of Au and Ag have also shown interesting result., Chou et al. [30] optimize the growth time and reservoir effect by switching from a vapor-liquid-solid growth mechanism to a vapor-solid-solid growth mechanism within the growth. Also since the reservoir effect is dependent on the amount of nanowire material dissolved in the seed particle it has been suggested that the reservoir effect can be decreased by changing the seed particle [31].

Ag as a material has similar properties to Au. Both metals are noble with a face centered cubic crystal structure and a relatively high melting temperature (962°C and 1064°C respectively) [32, 33]. Since the exact reason for Au being such a good material for seeeding nanowires is still not known [34] Ag is, with its similar properties to Au, a good metal to evaluate as seed material. Already today a few reports that utilize Ag for growth of nanowires have been published. MBE grown InAs nanowires with Ag as seed particle have been reported on at least two occasions [35, 36]. CBE grown patterned InSb nanowires directly on InSb(111)B substrates have shown better results with Ag as seed particle than with Au under similar growth conditions [37]. Ag has also been shown to seed InP nanowires with MOVPE [38]. For single compound nanowires of Si CVD grown nanowires with Ag as seed material have also been demonstrated [39, 40]. Not only do these reports show that a wide range of materials can be seeded by Ag particles, all the common growth techniques, MBE, CBE and CVD, are also represented. Using the laser ablation method for growth of nanowires Ag has also been used to seed GaO nanowires [41] although no images for the Ag-seeded nanowires are presented in the referenced

article. These results are strongly indicative that Ag is indeed a promising material for nanowire growth and worth investigating further in order to understand the possibilities and limitations of particle-seeded nanowire growth.

We hope that by investigating new seed materials new possibilities for nanowire growth will open up and that it can help increase the general understanding of how and why nanowires grow.

My contribution

In the Ag-seeded GaAs nanowire project (chapter 4) I have been involved in all steps of the experiments. I have prepared substrates, performed some of the growths, performed SEM analysis for mainly the high temperature GaAs(100) samples and parts of the As series. I have also performed most of the TEM of the growths on (111)B substrates. I have co-authored the paper and been involved in discussions and interpretation of the data. Besides myself, Jessica Bolinsson[1] has performed growths and SEM, Alexander Whiticar[1] SEM and Kimberly Dick Thelander[2,3] TEM.

For the cross-section samples (chapter 4) in Barcelona I planned the growth time series and I took part in the cross-section preparations together with Fransisco Belarre[4] and Sara Martí Sánchez [4]. The TEM images was acquired jointly with Jordi Arbiol[4] and Sara Martí Sánchez[4]. I performed all the analyses on the TEM data.

In the Ag-seeded InAs nanowire project (chapter 5) I operated the MBE for the annealing experiments while co-supervising Anders Bjørlig [1] who performed the SEM analysis, including the SEM analysis for some of the early growths [42]. I planned and performed all the growth experiments, and I also performed most of the SEM analysis on the nanowire growth experiments. The TEM images are acquired jointly with Sara Martí Sánchez[4].

In the Raman project (chapter 6) I was responsible for the TEM part. I performed the low magnification images on the Philips CM20 microscope and analyzed the images Sebastian Lehmann[2] acquired on the JEOL 3000F microscope at Lund University. I also co-authored the paper and took part in writing the paper. Rawa Tanta[1] acquired and analyzed all the Raman data and images.

Except for the projects presented in this thesis I have also fabricated planar chips for electropolymerisation, worked with bonding of nanowires for electropolymerisation and characterized InAs nanowires for nanowire-cell interaction. All these projects were performed through a collaboration with Karen Martinez[5] group at Nano-Science Center & Department of Science at Copenhagen University. I have also performed TEM work on InAs/III-As core-shell nanowires and InAs nanowires with an Al shell.

[1] Center for Quantum Devices and & Nano-Science Center, Niels Bohr Institute, University of Copenhagen, Copenhagen, Denmark

[2] Solid State Physics and NanoLund, Lund University, Lund, Sweden

[3] Center for Analysis and Synthesis, Lund University, Lund, Sweden

[4]Institut Català de Nanociència i Nanotecnologia (ICN2), Bellaterra, Barcelona, Catalonia, Spain

[5]Bionanotechnology and Nanomedicine Laboratory, Department of Chemistry and Nanoscience Center, University of Copenhagen, Copenhagen, Denmark

List of Papers

I. **Silver as Seed-Particle Material for GaAs Nanowires–Dictating Crystal Phase and Growth Direction by Substrate Orientation**
Caroline Lindberg, Alexander Whiticar, Kimberly A. Dick, Niklas Sköld, Jesper Nygård and Jessica Bolinsson, *Nano Letters*, 2016, 16, 2181–2188

II. **Raman Spectroscopy in the detection of stacking fault density in InAs and GaAs nanowires**
Rawa Tanta, Caroline Lindberg, Sebastian Lehmann, Jessica Bolinsson, Miguel R. Carro-Temboury, Kimberly A. Dick, Tom Vosch, Thomas Sand Jespersen and Jesper Nygård, *Preprint*

Chapter 2

Growth of III-V semiconductor nanowires

This chapter explains the basic techniques and theories behind growth of III-V semiconductor nanowires using Molecular Beam Epitaxy (MBE). The first part 2.1 explains how the MBE works. It also contains a short description of our system and the procedures performed before growth in order to keep the vacuum integrity of the system. In this part Reflection High-Energy Electron Diffraction (RHEED), which is a way to characterize the MBE sample during layer or nanowire growth, is also explained. Part 2.2 deals with the general theory of epitaxial growth while part 2.3 explains the specific growth theory behind particle-assisted nanowire growth in MBE. Part 2.4 and part 2.5 explain the different ways of creating nanoparticles for nanowire growth and the relevant crystal structures in III-V nanowires, respectively.

2.1 Molecular Beam Epitaxy

The first part in this section will explain the basic setup behind MBE. All information has been adapted from the books Molecular Beam Epitaxy Fundamentals and Current Satus by M. H. Herman and H. Sitter [43] and Molecular Beam Epitaxy: Principles and Applications by G. Biasol and L. Sorba [15] unless otherwise stated. The second part of 2.1 presents the setup and procedure related to our specific MBE system.

The MBE technique was first developed in the 1960s in order to grow high quality semiconductor epitaxial thin films. The crystal growth in the MBE takes place in an Ultra High Vaccuum (UHV) growth chamber and the basic principles are fairly simple. Effusion cells, each containing a certain element, are directed towards the sample where the growth is taking place, see the growth chamber in Figure 2.1. When the effusion cells are heated the element inside will start to evaporate. Due to the UHV inside the growth chamber the mean free path of the evaporated molecules or atoms will be longer than the distance between the effusion cell and the substrate preventing the atoms from interacting with each other. This will create an atom or molecular beam (rather than a gas) which is directed towards the substrate. All the effusion cells are individually heated since the temperature of the effusions cell controls the atom/molecular beam flux. Different effusion cells are used for different elements depending on vapor pressure and reactivity, but most common is simply a boron nitride crucible heated radiatively. For

the group V element the effusion cells are a bit different consisting of a sublimator zone and a cracker zone. The cracker zone is a higher temperature region which "cracks" the V_4 molecules to V_2 molecules, a difference which could have a considerable effect on the growth of the thin film.

Aside from the classical solid-source MBE other techniques have been developed such as metalorganic MBE (MO MBE) and chemical beam epitaxy (CBE).

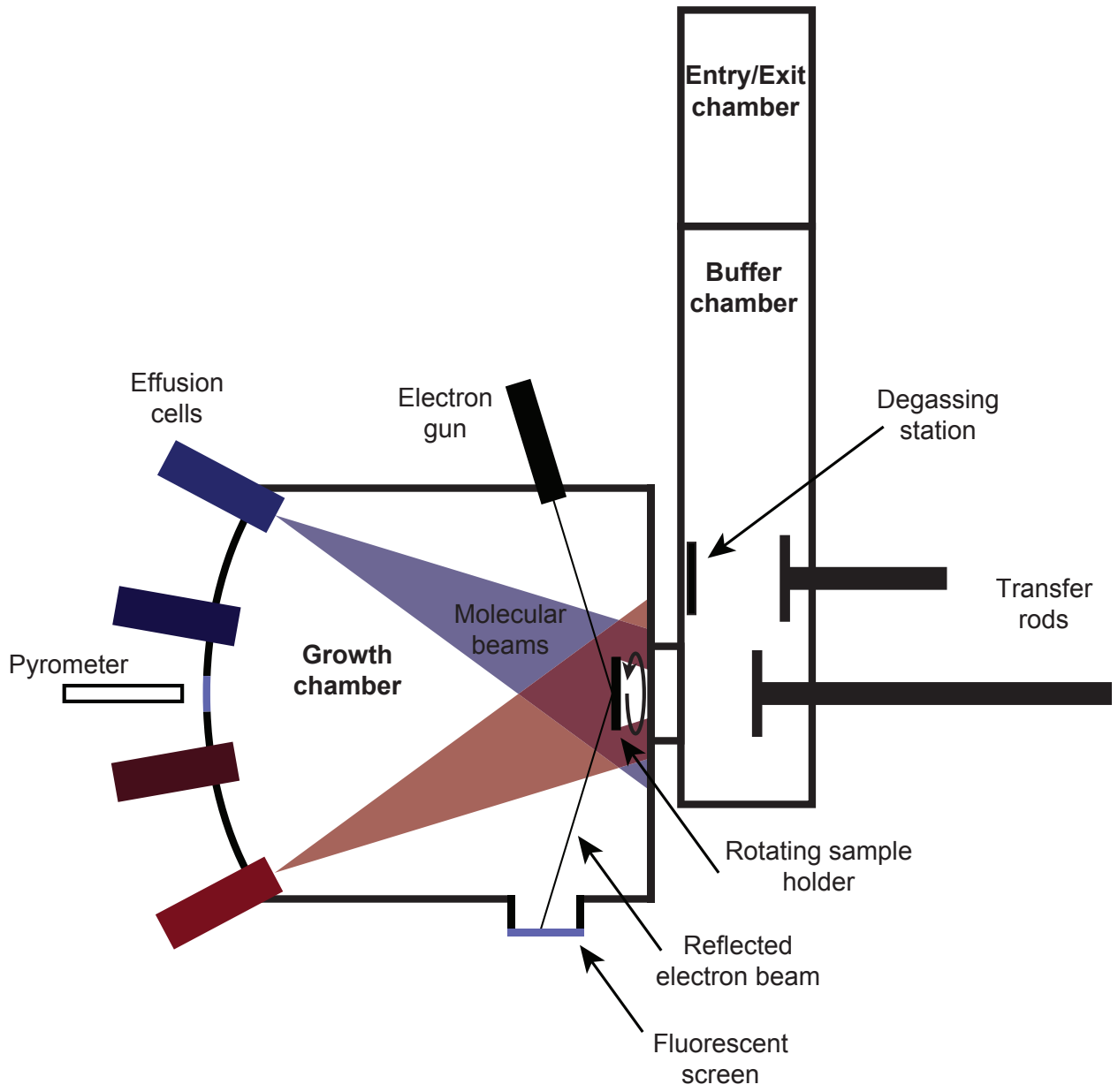

Figure 2.1: Sketch over the MBE setup, the three different chambers in our MBE system are labeled with bold text. The samples are introduced and removed from the Entry/Exit chamber, individual degassing of the substrates are performed in the Buffer chamber and the growth is performed in the Growth chamber. The transfer rods are used to move around the sample holders inside the MBE.

The MBE setup

All MBE growths presented in this thesis are grown with a Varian Gen II solid source MBE system with a base pressure of 10^{-11} Torr. The following text is a description of the specific MBE used in our experiments, including a presentation of the chambers and degassing procedure used in the projects presented in this work. A shematic view of our MBE is seen in Figure 2.1.

To mount the substrates on the Mb MBE sample holders the substrates need to be of specific sizes: quarters of a 2 inch wafer, 2 inch wafers or a quarter of a 3 inch wafer. Only one sample holder can be inside the growth chamber at one time. If substrates are

of other shapes or multiple substrates should be grown they need to be mounted to a carrier wafer of the correct shape and size. To not contaminate the system liquid Ga is used to mount the growth substrate to the carrier wafer. The MBE holders are placed on a trolley that is used to move around the sample holders with the substrates inside the MBE chamber.

After mounting the samples are introduced to the MBE through the Entry/Exit chamber. Whenever the Entry/Exit chamber is opened it is flushed with N_2 in order to prevent contaminations and water from the air from entering the chamber. Inside the Entry/Exit chamber the whole trolley is heated to 200°C for 2 hours in a vacuum below 10^{-7} Torr.

When the samples have cooled down and the pressure in the Entry/Exit chamber has reached low 10^{-9} Torr the trolley can be moved into the buffer chamber. In the buffer chamber each substrate that should be introduced to the growth chamber is individually degassed at 250°C, or higher, on the degassing station to remove the remaining water and other lightly bound contaminants.

The growth chamber is the heart of the MBE, this is where the effusion cells are located and all the nanowire or layer growth takes place. The effusions cells in our MBE contain: Au, In, Ga, As (with a cracker), Al, Si, Be, and Sb (with a cracker). In addition to controlling the beam flux by the cell temperature the As and Sb effusion cells are also equipped with a needle valve which enables a fast change of the flux. The substrate temperature is controlled by a thermocouple located on the backside of the wafer giving feedback to the heater via a temperature controller. In order to check the "true" surface temperature of the substrate a pyrometer is placed outside the growth chamber. To allow for an idea of the temperature differences over the substrate (which can be substantial in our system [44]) the pyrometer can be moved to target different areas of the substrate/sample/carrier wafer. On the backside of the sample holder there is a pressure gauge making it possible to measure the pressure for the individual beam fluxes. To reduce effects of the beam position the sample can be continuosly rotated during growth.

To make sure that the samples are clean mass spectrometry can be performed in all three chambers. This is especially important if the substrates have been in contact with any solvents or resists before loading.

Reflection High-Energy Electron Diffraction

One great advantage of the UHV inside the MBE growth chamber is the possibility to add additional surface analyzing tools, which can be used during growth. The MBE can be equipped with Reflection High-Energy Electron Diffraction (RHEED), Auger Electron Spectroscopy (AES) and Ellipsometry. In our system we have a RHEED installed.

RHEED is based on electron diffraction and the graphical setup can be seen in Figure 2.2 a). An electron gun is positioned inside the MBE growth chamber such that the generated electron beam hits the growth substrate at a low angle, typically 1-8°. The electron beam will diffract on the substrate and the resulting pattern is shown on a fluorescent screen. Due to the relatively low energy of the electron beam in RHEED (which does penetrate but not deeply into the substrate) and the low angle, the diffracted pattern will be a result of both the bulk crystal and the surface atoms [45]. This makes RHEED an excellent tool to analyse the surface reconstructions of the substrate during growth. In fact some of the different surface reconstructions for GaAs(100) undergo

transitions at certain fixed temperatures which can be used to calibrate the substrate temperature [46]. An example of the RHEED signal from a reconstructed GaAs(100) surface at 600°C can be seen in Figure 2.2 b)-c).

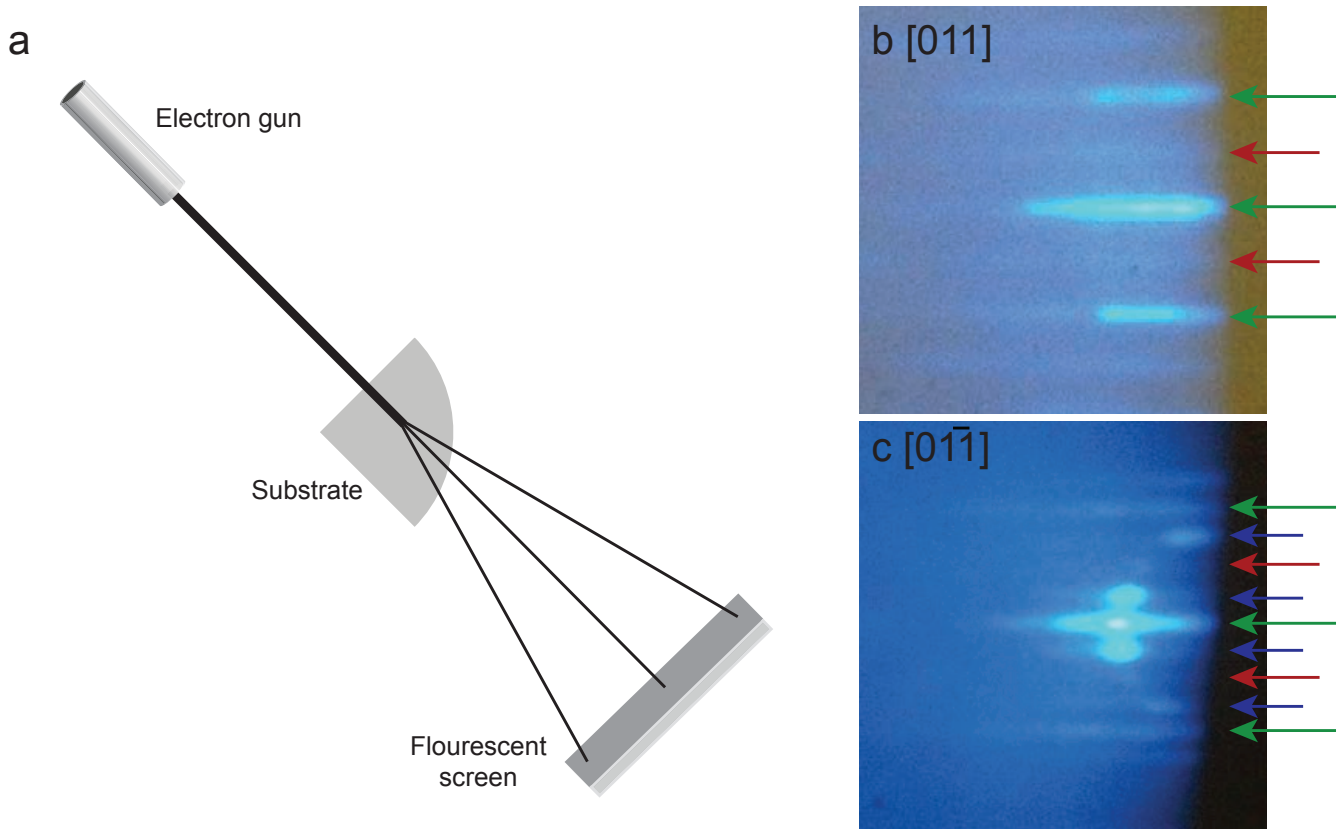

Figure 2.2: a) Basic setup over RHEED. b)-c) RHEED patterns from a GaAs(100) substrate after oxide removal. The substrate has a (2x4) surface reconstruction. The electron beam directions are [011] and [0$\bar{1}$1] for b) and c) respectively. The lines marked with green arrows originate from the bulk crystal structure while lines marked with red and blue arrows are products of the surface reconstruction.

The RHEED specular spot (direct beam) will always be strongest when a full monolayer is grown (and the surface is flat) and weaker during the growth of one monolayer (when many atom steps are present). Accordingly, by monitoring the intensity of the RHEED signal from high - to low - to high again the time for the growth of one monolayer can be measured. This makes it possible to calibrate the growth rate for the MBE at different beam fluxes [45].

In this work RHEED has mainly been used to confirm removal of the native oxide from the III-V substrates before nanowire growth. Since the native oxide of the III-V substrate is amorphous the RHEED pattern will either not show any streaks at all or only weak streaks from the bulk when the substrate is introduced to the growth chamber. When the substrate is heated and reaches the material dependent deoxidation temperature the streaks in the RHEED pattern will become clearly defined, indicating that amorphous oxide has evaporated.

2.2 The nucleation process

There are many different approaches to describe the interactions inside the MBE or in general while growing a thin film. An intuitive way of describing growth is to address what is happening to a single atom or molecule while interacting with the substrate, illustrated in Figure 2.3. An atom arriving at the substrate may undertake many different interactions. First; the atom can be reflected away, the interaction not causing anything

else than a change of path for the atom. Second; the atom can also be physically adsorbed by the surface of the substrate. A physically adsorbed atom is weakly bound to the substrate and can diffuse on the surface. Third; a physically adsorbed atom can either desorb and go back to the gas phase or it can become chemically adsorbed, thus forming chemical bonds to the substrate. Even after chemical adsorption the atom can desorb from the substrate but due to the higher energy bond the probability is lower than for a physically adsorbed atom [47].

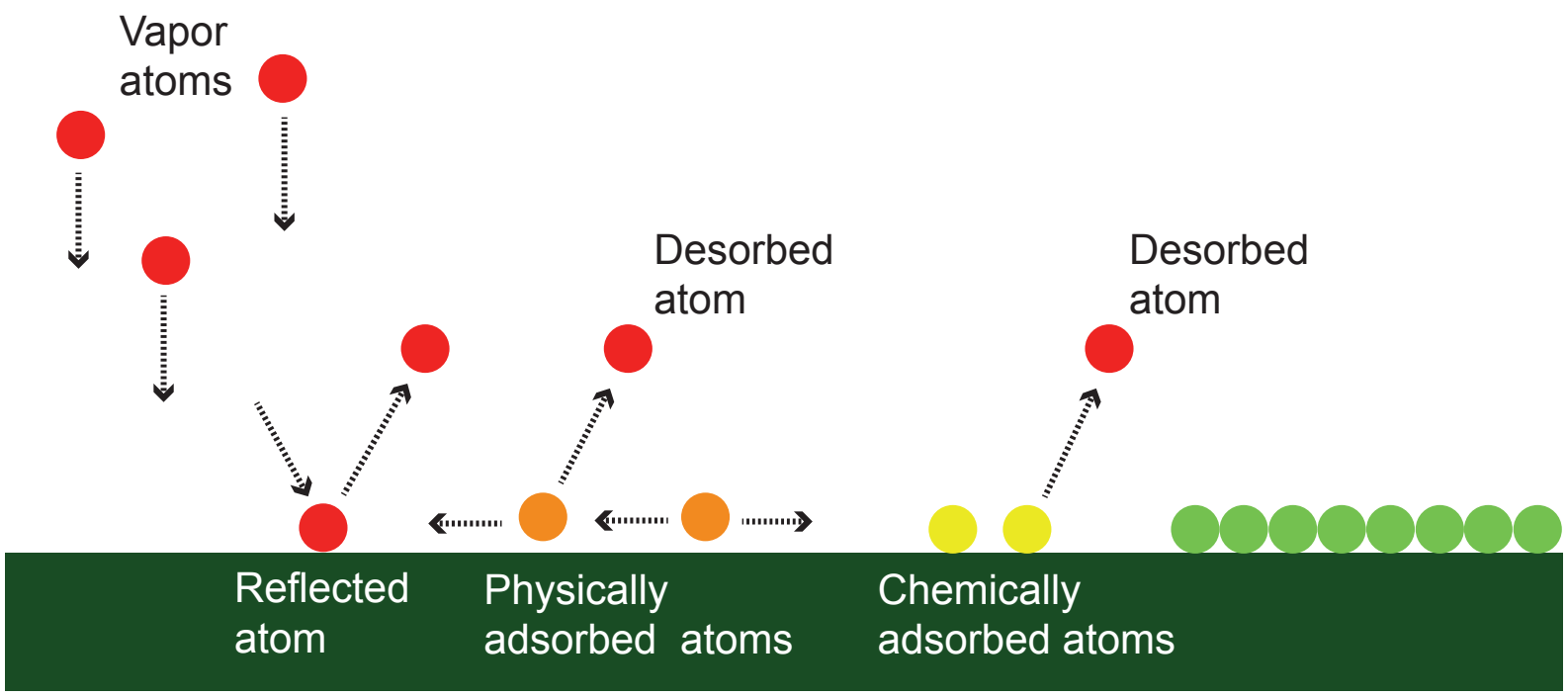

Figure 2.3: shows the different interactions available to an atom from the atomic flux in an MBE. The atom can be reflected directly, the atom can be physically adsorbed by the substrate or the atom can be chemically adsorbed by the substrate.

So far we have described what happens to a single atom or molecule when it is interacting with the substrate. However to further describe the process of crystal growth we will move to a thermodynamic approach. Any change of phase such as gas phase to solid phase is driven by a difference in chemical potential. The chemical potential describes the relation between the change of Gibbs free energy for a system with a change of moles, hence the chemical potential can be defined as equation 2.1 [47].

$$\mu = \left(\frac{\delta G'}{\delta n}\right)_{T,P} \tag{2.1}$$

where μ is the chemical potential, $\delta G'$ is the change of Gibbs free energy within a system and δn is the change of moles in the system. The T and the P denote a constant temperature and pressure. When a material moves from the gas phase in the MBE to bind with the substrate it undergoes a phase change from a gas phase to a solid phase. If the chemical potentials for the gas and the solid are equal, see equation 2.2, the system is in steady state and the same amount of material evaporates as solidifies [47].

$$\mu_{gas} = \mu_{solid} \tag{2.2}$$

Here μ_{gas} is the chemical potential for the gas phase while μ_{solid} is the chemical potential for the solid phase. When the physical properties of the system are altered it might change

the balance between the chemical potentials. The system will then leave the steady state and material will either solidify or evaporate to a greater extent. If $\mu_{gas} > \mu_{solid}$ more material will solidify than evaporate and we will have crystal growth in the MBE. The difference in chemical potential $\Delta\mu = \mu_{solid} - \mu_{gas}$ is called the *supersaturation*. When the gas phase is superaturated the reaction will move from gaseous to solid phase [48].

The transition from gas to a thin solid layer starts with the nucleation. Nucleation is simply a way to describe how clusters of atoms become stable enough to not evaporate into the gas phase again. This is described with the classical nucleation theory (CNT) which is more thoroughly presented in [49]. Considering homoepitaxial growth a forming cluster will increase the surface and hence the surface energy. Therefore a cluster of atoms will initially increase the energy even though the gas is supersaturated. However, due to fluctuations in the system small clusters will form and disintegrate continously. If these clusters overcome a critical nucleus size the increased surface energy will be lower than the energy gained by forming the cluster. Hence the atom cluster will have a lower probability to disintegrate than to grow, and a nucleus has formed. The critical size of the nucleus can be described by equation 2.3

$$n^* = \left(-\frac{2}{3} \frac{A\sigma}{\Delta G_{nucleus}} \right)^3 \tag{2.3}$$

where n^* is the number of atoms of the critical nucleus, A is a geometric factor, σ is the interface free energy and ΔG is the nucleation free energy.

2.3 Growth of particle seeded III-V nanowires

The basic concept behind particle-seeded semiconductor nanowire growth in MBE is simple and illustrated in figure 2.4. Step 1, a particle is placed on a substrate. Step 2, the substrate is heated to a sufficiently high temperature for the native oxide to disappear. During the heating the particle and the substrate will form an alloy. At this high temperature the substrate is usually kept under group V overpressure to supress substrate degradation. Step 3, the temperature is set to the correct nanowire growth temperature and group III-flux is added. Group III atoms will either diffuse on the substrate until it reaches the particle or directly impinge on the particle. When the particle becomes supersaturated nucleation in, peferably, the triple phase boundary (TPB) will take place [50]. The TPB is the location of the particle where the solid phase of the nanowire, the particle and the gas phase encounter each other. After the nucleation at the TPB a bilayer of atoms will grow beneath the particle. Step 4, with continuous nucleation at the TPB and subsequent bilayer growth a nanowire will precipitate. Hence, when nanowire growth takes place the nucleation at the TPB is enhanced compared to nucleation on the substrate.

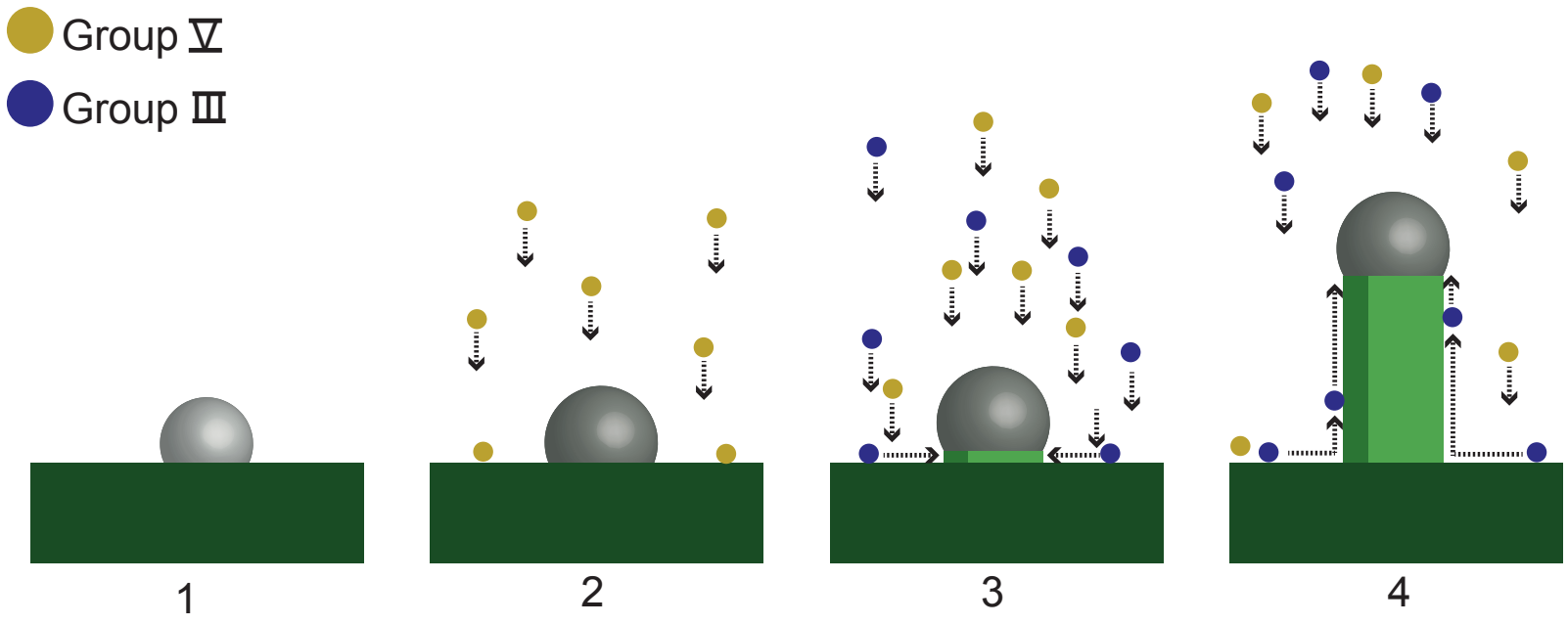

Figure 2.4: shows the basic concept behind nanowire growth. 1, a particle is placed on the wafer. 2, the particle forms an alloy with the substrate under a group V overpressure. 3, group III is introduced and the atoms will diffuse to the particle and group III and V will nucleate in the TPB. 4, the nucleation continues under the particle resulting in a nanowire.

Much time and effort has been put into understanding the process of nanowire growth and the role of the particle. Wagner and Ellis [51] introduced already in 1964 the concept vapor-liquid-solid (VLS) growth which is still today used to describe nanowire growth to a high extent. The basic assumption in VLS growth is that a liquid droplet catalyzes the crystal formation below the droplet. The increased nucleation rate below the particle compared to the substrate surface results in growth of the a nanowire. The VLS theory has since been developed [52] and combined with the CNT [53]. Combination with the CNT made it possible to predict whether the nanowire nucleates in a zinc-blende or wurtzite crystal phase [50, 54]. Today reports of growth with a solid particle, the vapor-solid-solid (VSS) mechanism, have also been presented [55][56] and even the possibility to vary between a solid particle and a liquid particle during growth in order to optimize growth time and nanowire properties [30]. With the insight of a solid phase of particles being possible new models for particle-grown nanowires are necessary. The preferential interface nucleation [57] focuses on the enhanced material collection of the particle, the increased nucleation at the TPB and suppressed nucleation at other surfaces rather then the specific phase of particle. Recent in-situ TEM studies of V-III nanowires [58, 59, 60, 61] have made it possible to study the nucleation and bilayer formation in real time, giving even deeper understanding of the process of nanowire growth.

2.4 Preparation of metal particles for nanowire growth

Metal particles in the small dimensions used for nanowire growth can be generated by a variety of different techniques. The positive and negative aspects of most techniques are reviewed by Messing et al. in [62]. If control of the size and density of the particles are important but not the placement techniques like deposition of aerosol particles and colloidal particles can be used. If control over both the size and the position of the particles are necessary lithography techniques such as electron beam lithography (EBL) [62] or laser interference lithography (LIL) [37] can be used. Another common method is

the thin film annealing method. Here a thin film of the metal intended for the particles is deposited onto a substrate. When the substrate is heated before growth the thin film will break up and form particles, see Figure 2.5. The final size and distribution of the particles will depend on the annealing process used. A longer annealing time [63] and a higher temperature [63, 64] will result in bigger particles. Other factors that affect the final particles are the thickness of the thin film where a thicker film results in bigger particles with a lower density [65] [64] [63]. The advantage of using a thin film, especially when exact growth conditions are not known, is the wide size distribution of the particles obtained. If only a limited size range of particles nucleates nanowires this size range will hopefully be covered with the thin film annealing method. The thin film annealing method is also a very clean process and no contaminants like resist or solvent residues will affect the growth [62]. In our case the samples have been prepared with the thin film method or EBL. The Ag films have in this work been deposited with electron beam evaporation, more explicity a custom made AJA evaporation chamber with a thermionic e-gun. The samples have then been transported in ambient air before being loaded into the MBE.

Figure 2.5: shows the basic concept behind formation of particles from a thin film. 1, a thin film is deposited onto a substrate. 2, when the thin film is heated the film breaks up into particles.

As mentioned above a couple of samples have been prepared with EBL. The EBL process can be divided into a series of steps, see Figure 2.6. The process starts off with a pristine substrate. In step 2, the substrate is covered with one or more layers of resists. In step 3, specific regions of the resist are illuminated with an electron beam. In step 4, the resists are developed in a resist specific chemical. During the development the regions illuminated with electrons or the regions not illuminated with electrons are removed (positive tone and negative tone respectively) [66]. In all our processing a positive tone has been used. In step 5 a thin film of the relevant material, in our case Ag, is deposited on top of the resists and the resist-free areas of the substrate. In step 6 the sample is submerged in another solvent to remove the remains of the resist, the lift off process. What is left is a substrate with a thin film in a specific pattern. For a detailed description of our recipes used see appendix F.

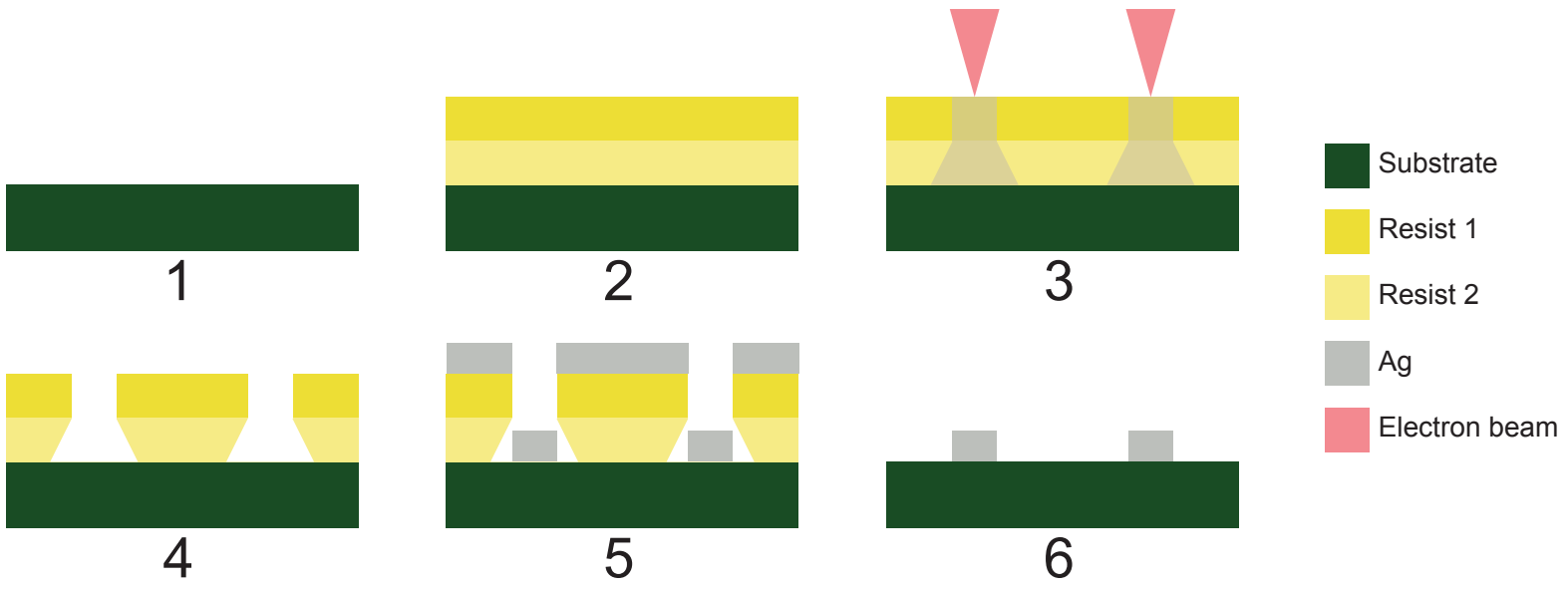

Figure 2.6: shows the schematic steps in an EBL process. 1) a clean substrate. 2) resist coating 3) illumination of the sample with an electron beam, 4) development of the resists, 5) thin film deposition, 6) after the lift off process, only the thin film on the substrate remains.

2.5 Crystal structure in III-V semiconductor nanowires

A crystalline material is a material "where the atoms, molecules, or ions pack together to form a regular repeating array" [67]. In order to describe the "regular repeating array" we divide the structure into the smallest possible unit required to build the full structure - the unit cell.

The two semiconductors InAs and GaAs both have a zincblende (ZB) crystal structure in their bulk form. A ZB crystal structure is a cubic crystal system, more specifically the unit cell consists of two face-centered-cubic crystals that have an offset of $(\frac{1}{4}\frac{1}{4}\frac{1}{4})$ with regards to each other. Except for the bulk crystal structure ZB, GaAs and InAs nanowires can also exhibit other crystal structures, the most common being wurtzite (WZ). The WZ crystal structure belongs to the hexagonal crystal system and the semiconductor crystal structure is comprised of two hexagonal unit cells with an offset of $(000\frac{1}{2})$.

The two crystal structures ZB and WZ can also be described by the repeating layers that they exhibit in the close packed direction. Since both InAs and GaAs are two compound structures with the same number of group III and group V atoms the crystal will be formed by stacking bilayers on top of each other. These bilayers can be stacked in either an ABCABC (ZB) manner, see Figure 2.7 b) or an ABAB (WZ) manner see Figure 2.7 f). In the ABAB stacking the atoms in bilayer B are positioned between the atoms in bilayer A. The third bilayer is then positioned between the atoms in bilayer B and directly above bilayer A, forming another A layer. This is illustrated in Figure 2.7 f). If the atoms in bilayer three is instead positioned so they are not on top of either layer A or B but instead form a third atom placement, C, we have an ABC stacking. This is illustrated in Figure 2.7 b). Other higher order symmetries of crystal structures such as 4H and 6H are rare but can also be found in III-V nanowires. For further reading about the different crystal structures in nanowires see for example [68].

The most common growth direction for III-V nanowires are <111>B for ZB nanowires, illustrated Figure 2.7 b), and <0001> for WZ nanowires, illustrated in Figure 2.7 f). The bonding configuration between atoms in the <111>and <0001> directions for ZB and WZ, respectively, are similar to each other and switching between the ZB and the WZ

crystal structures is fairly easy in those growth directions [68]. This has the result that nanowires grown in the <111>B or <0001> directions often contain crystal defects [69]. Nanowires grown in the <111>B and <0001> direction usually have six facets. The facets can be either {110} or {112} type for ZB nanowires or $\{01\bar{1}0\}$ or $\{2\bar{1}\bar{1}0\}$ type for WZ nanowires. In Figure 2.7 a) and c) {112} and $\{01\bar{1}0\}$ are depicted since these are the relevant facets in Chapter 5. Reports of III-V nanowires in other growth directions than $[\bar{1}\bar{1}\bar{1}]$ and [0001] are fewer but do exist and are reviewed in [19]. As mentioned in the introduction one of the most desirable substrates to grow nanowires on are (100). A ZB nanowire grown in the <100> direction is shown in Figure 2.7 c) and d). The illustrated facets for the <100> nanowire in Figure 2.7 c) are set to <110> since these are the types of facets obtained later in Chapter 4.

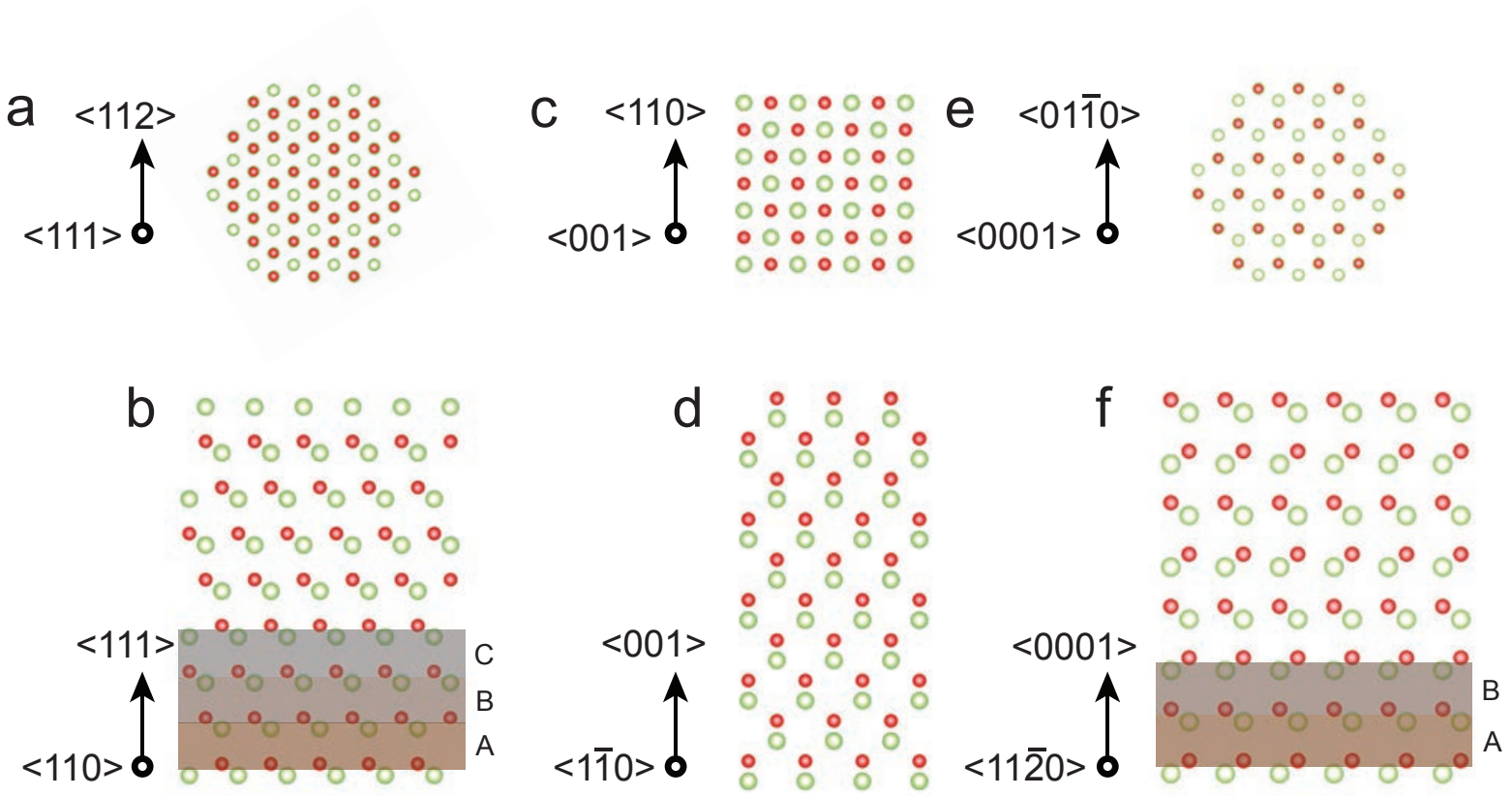

Figure 2.7: Illustration over crystal types and directions. a) and b) a ZB nanowire viewed along the <111> and <110> direction repsectively; this is the typical top view and side view for a III-V ZB nanowire. c) and d) ZB crystal structure viewed along the <100> and <110> crystal directions, respectively, illustrating top view and side view of a nanowire grown in the <100> direction. d) and e) WZ crystal structure viewed along the <0001> and <11$\bar{2}$0> direction respectively, this is the typical top view and side view for a III-V WZ nanowire.

Chapter 3

Electron Microscopy

Electron microscopes are microscopes that utilize the short wavelengths of electrons in order to increase the resolution and thus magnification compared to conventional visible light microscopes. In this work mainly two different kinds of electron microscopes have been used. To analyze the density, morphology and overall sample structure scanning electron microscopy (SEM) is used. To find the crystal structure, crystal purity and material composition of the nanowire transmission electron microscopy (TEM) is used. This chapter gives an overview on why electron microscopy is necessary to analyze structures in the nanowire size region. It will also give a short description of the instruments and the different techniques used within this work. All information in this chapter regarding TEM and electron-sample interaction is adapted from Transmission Electron Microscopy by D. B Williams and C. B. Carter unless otherwise stated [70]

3.1 Why we need electrons

In visible light microscopes the resolution will always be limited by the wavelength of the light according to the Rayleigh criterion, see equation 3.1.

$$\delta = \frac{0.61\lambda}{\mu \sin(\beta)} \tag{3.1}$$

Here δ is the smallest distance possible between two resolved features, λ is the wavelength of the light, μ is the refractive index of the viewing medium and β is the semi angle of the collection of the magnifying lens. This equation is often approximated to $\frac{\lambda}{2}$. Among the colors of the visible light violet has the lowest wavelength of around 400 nm; this gives a resolution limit of around 200 nm. Since nanowires can have a diameter well below 200 nm this resolution is clearly insufficient to study the morphology or the crystal structure of the nanowires. Electron microscopes instead take advantage of the short de Broglie wavelengths (see equation 3.2) electrons acquire when accelerated to great speeds.

$$\lambda = \frac{h}{[2m_0eV(1 + \frac{eV}{2m_0c^2})]^{\frac{1}{2}}} \tag{3.2}$$

Here λ is the de Broigle wavelength of the electrons, h is Planck's constant, m_0 is the mass of the eletron at rest, eV the energy of the electron and c the speed of light

in vacuum. This equation states that an electron accelerated by the typical acceleration voltages for TEM of 200 kV or 300 kV have a wavelength of 3 or 2 pm respectively. Even though the Rayleigh criterion is not directly transferable to electrons the shorter wavelengths of the electrons makes it possible to construct microscopes with far better resolution than conventional visible light microscopes. Contrary to visible light microscopes the resolution of electron microscopes is not limited by the wavelengths but aberration effects in the electromagnetic lenses. Many of the aberrations can today be corrected for and today both TEM and STEM can obtain sub-angstrom resolution, see reference [71] and references inside.

3.2 Electrons interaction with a sample

When an electron beam is interacting with a sample numerous different signals are created. For an overview over the signals see Figure 3.1. If the electrons are transmitted through the sample without any interactions they are referred to as unscattered electrons or the direct beam. Elastically scattered electrons have interacted with the sample without any energy loss. Inelastically scattered electrons are scattered electrons which have lost energy while interacting with the sample. These are the main signals for imaging in a TEM. Backscattered electrons (BE) are electrons from the incoming electron beam which have scattered $> 90°$. Secondary electrons (SE) are electrons which originate from the sample but have been excited out from the sample by the incoming electron beam.

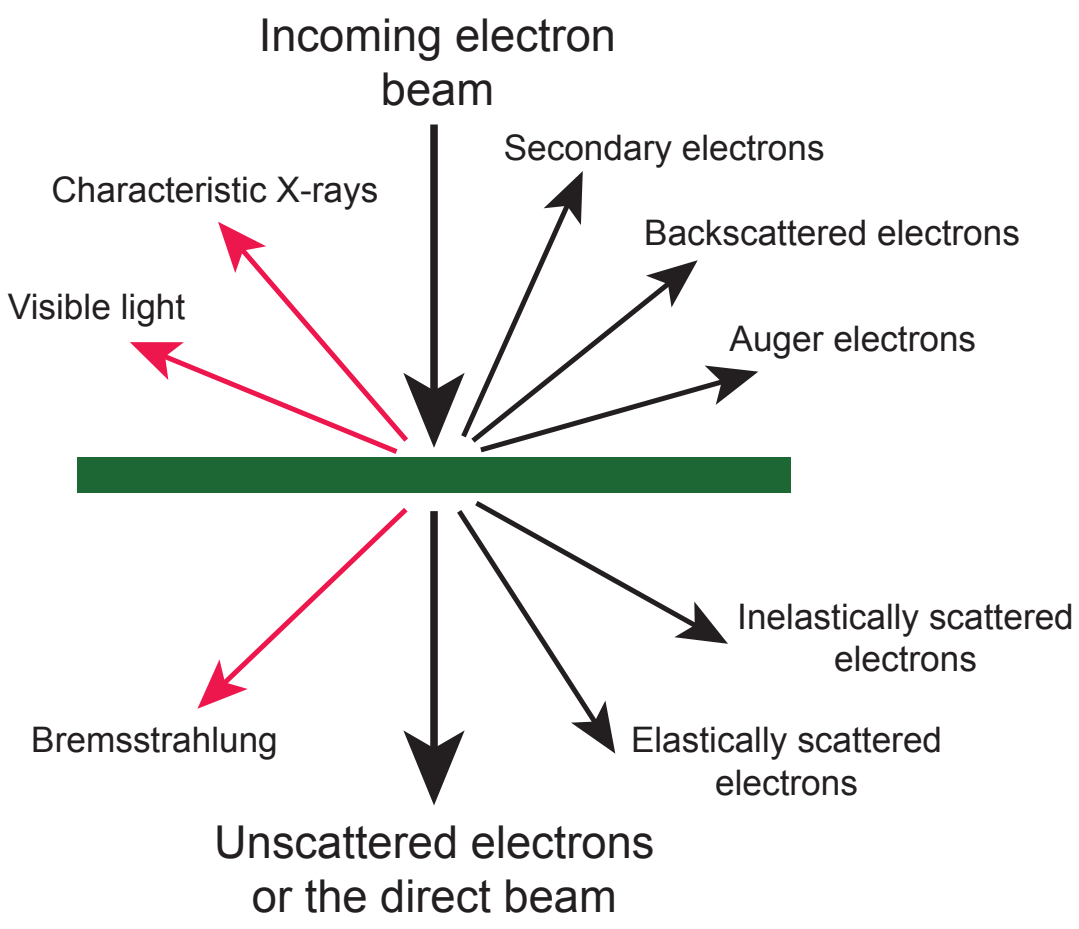

Figure 3.1: The different signals emitted from a thin sample when illuminated with a high energy electron beam. Black arrows show the electron signals while red arrows shows photon signals.

Both BE and SE are used to form images with SEM. Characteristic x-rays originate from the difference in energy released when an electron from a higher energy level fills an

empty position at a lower energy level. Since characteristic x-rays are specific for each element in the periodic table they can be used to gain information of the sample composition. Instead of creating a characteristic x-ray an electron relaxing from a higher energy level to a lower can give the energy to a third electron escaping from the sample. These electrons are called Auger electrons (AE). Bremsstrahlung is radiation that originates from electrons interacting with the Coulumb fields of the atomic nuclei.

3.3 Transmission Electron Microscopy

In transmission electron microscopy a thin sample is illuminated with an electron beam and the electrons that pass through the sample are collected to form an image. A graphical setup of a TEM together with an image of a Philips CM20 microscope is seen in Figure 3.2. Electrons are extracted from an electron gun either by heat, a high voltage or a combination thereof. The electrons are further accelerated to the desirable voltage and focused to a spot. Condenser lenses set the correct beam condition for the image technique required. In conventional TEM mode the electron beam is broad and coherent before interacting with the sample. The objective lens magnifies the image and the projector lenses place the magnified image onto a flourescent screen or camera. Since electrons are charged particles the lenses in electron microscopy are electromagnetic lenses which utilize magnetic fields to control the beam path throughout the TEM.

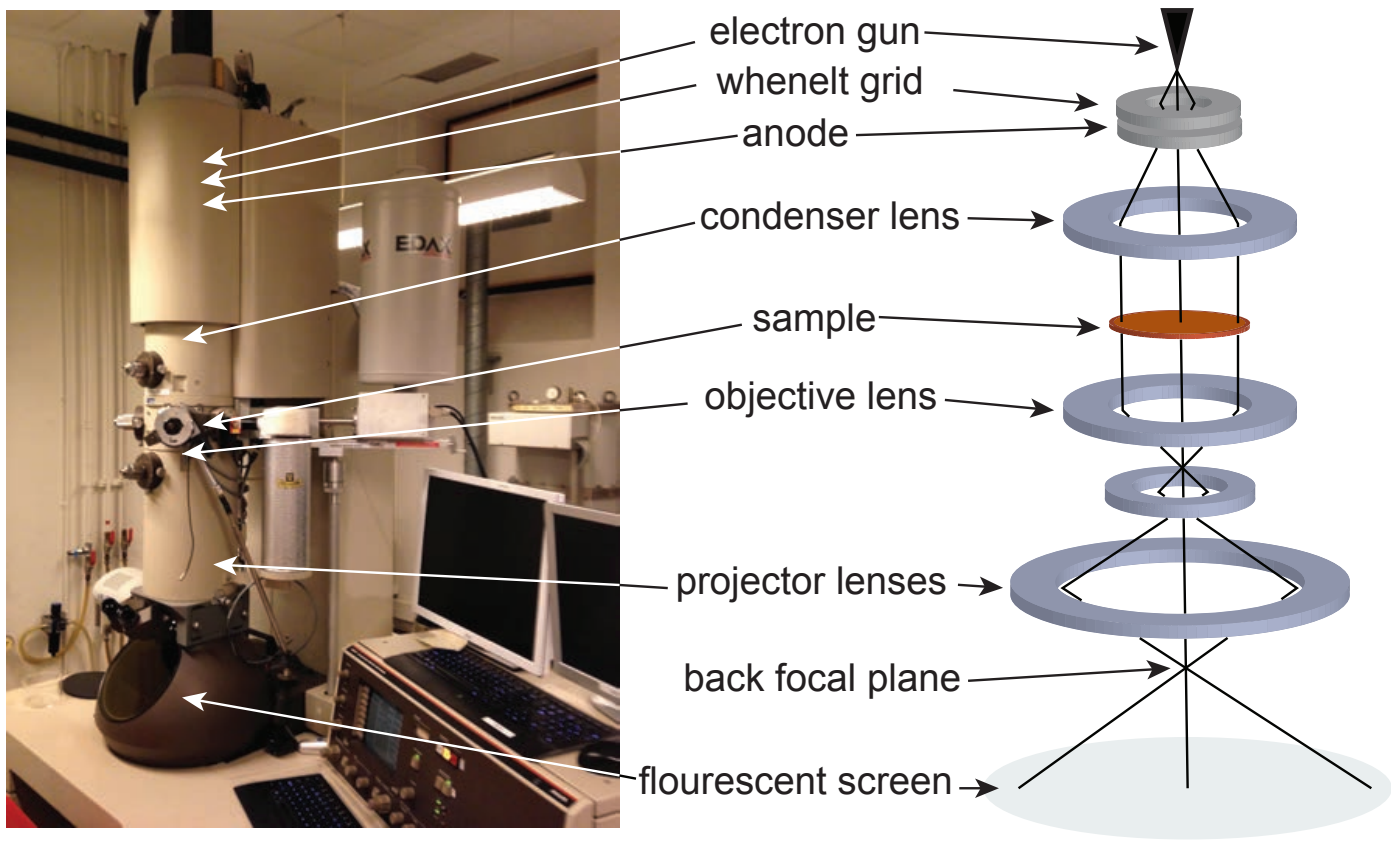

Figure 3.2: Image over a CM20 microscope and a graphical setup over a TEM

3.3.1 High resolution electron microscopy

The contrast in a TEM is generated in different ways, for example by diffraction contrast and mass-thickness contrast. These are however not the main contrast contributions while imaging in high resolution. In order to visualize the atom columns the contrast is instead based on phase shifts of the electrons. When a coherent beam is interacting with a sample the waves of the electrons that have interacted with the sample will undergo a phase shift compared to electrons that have not interacted with the sample. This phase shift is the main component of the contrast when high resolution images are acquired.

3.3.2 Diffraction in TEM

To obtain high resolution images of crystalline samples they have to be oriented in the correct way, in a zone axis. To evaluate the orientation of the crystal and tilt it to the corrrect zone axis diffraction mode is used. A diffraction pattern, see Figure 3.3, also makes it possible to identify the crystal structure even though the TEM does not have the high resolution to visualize atom columns.

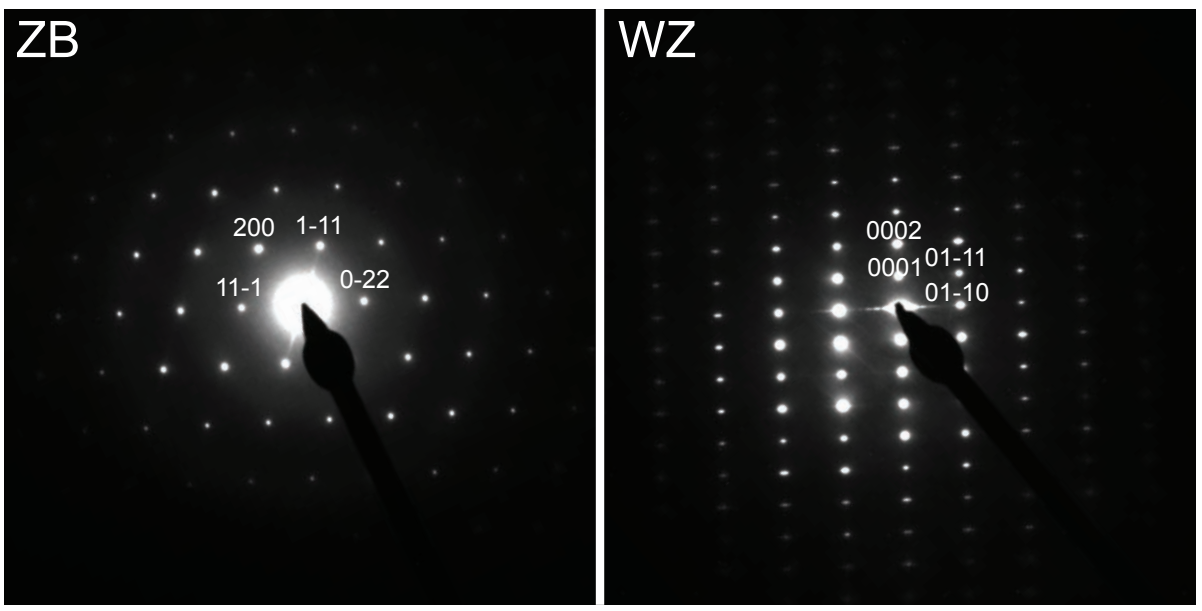

Figure 3.3: Two examples of selected area diffraction patterns. Left is a cubic ZB crystal from an InAs nanowire which is imaged in the [011] zone axis. Right is a hexagonal WZ crystal from a GaAs nanowire which is imaged in the $[2\bar{1}\bar{1}0]$ zone axis.

By controlling which part of the sample that is illuminated selected area diffraction patterns are obtained, giving crystallographic information like crystal orientation and/or crystal structure for that specific area of the sample. The most intuitive way to describe diffraction is by Bragg's equation, see equation 3.3.

$$n\lambda = 2dsin\theta \tag{3.3}$$

Here λ is the wavelength of the incoming electron beam, n is a positive integer, d is the distance between a specific set of hkl planes and θ is the Bragg angle. The Bragg angle is the angle of the incoming beam relative the lattice planes. When this condition is fulfilled constructive interference is obtained. In reality the lenses are changed so the back focal plane is imaged on the flourescent screen/camera in figure 3.2. The implication of this is that all electrons scattered in a certain direction will hit the flourescent screen (or camera) at the same point producing a diffraction pattern. Each spot in a diffraction pattern correlates to one set of hkl planes and can be identified in the pattern.

3.3.3 Scanning transmission electron microscopy and dark field imaging

In Scanning Transmission Electron Microscopy (STEM) instead of a broad coherent beam the electron beam is focused to a spot (convergent beam) which is scanned across the sample. All STEM images shown in this work are either Annular Dark Field STEM (ADF-STEM) or High Angle Annular Dark Field STEM (HAADF-STEM). When aquiring ADF-STEM or HAADF-STEM images only electrons scattered within a certain angle are allowed to contribute to the image. For ADF-STEM images all electrons scattered within 10-50 mrads form the image. For HAADF-STEM electrons scattered > 50 mrad contribute to the image. This produces an image formed mainly by mass-thickness contrast. The mass-thickness contrast originates (as the name suggests) from the mass (atom number) or the thickness of the sample. A higher atom number will interact stronger with the electrons and a thicker sample will generate more scattering events, hence more electrons reach the ADF or HAADF detectors. Due to the focused beam in STEM it is ideal for compositional analysis. The focused spot can be placed on the area of interest and only collect signals originating from that particular area. Hence compositional analysis can be obtained from specific areas of the sample and compositional differences can be detected.

3.3.4 Spectroscopy

So far everything discussed has been related to the structure of the sample. However, an electron microscope can also be utilized to determine the chemical composition of a sample. In this work two different techniques have been used to determine the chemical composition of the nanowires and their particles: X-ray Energy Dispersive Spectroscopy (XEDS) and Electron Energy Loss Spectroscopy (EELS). To be able to quantify the chemical composition of only the particle or the nanowire all spectroscopy analyses have been performed in ADF-STEM mode.

In XEDS the electron beam excites an atom by causing one of the core-shell electrons to be ejected to vaccuum or an unfilled state. When the atom relaxes by filling the empty state with an electron from a different shell a characteristic x-ray is emitted. For a sketch of the process see Figure 3.4. Since the energies of the emitted x-rays depend on the energy levels of the element, each element in the periodic table has a characteristic energy signature. In Figure 3.4 a XEDS spectrum is visible with the identified peaks noted. The ratio of the peak intensity between two elements will be proportional to the amount of each of the elements in the sample according to equation 3.4.

$$\frac{E_A}{E_B} = k_{AB}\frac{I_A}{I_B} \tag{3.4}$$

here E_A is the weight % of element A, E_B is the weight % of element B, k_{AB} a constant for this specific combination of materials and peaks. For exact measurements k_{AB} needs to be determined for a specific TEM and XEDS detector. I_A and I_B are the integrated intensities of the peaks for the respective material.

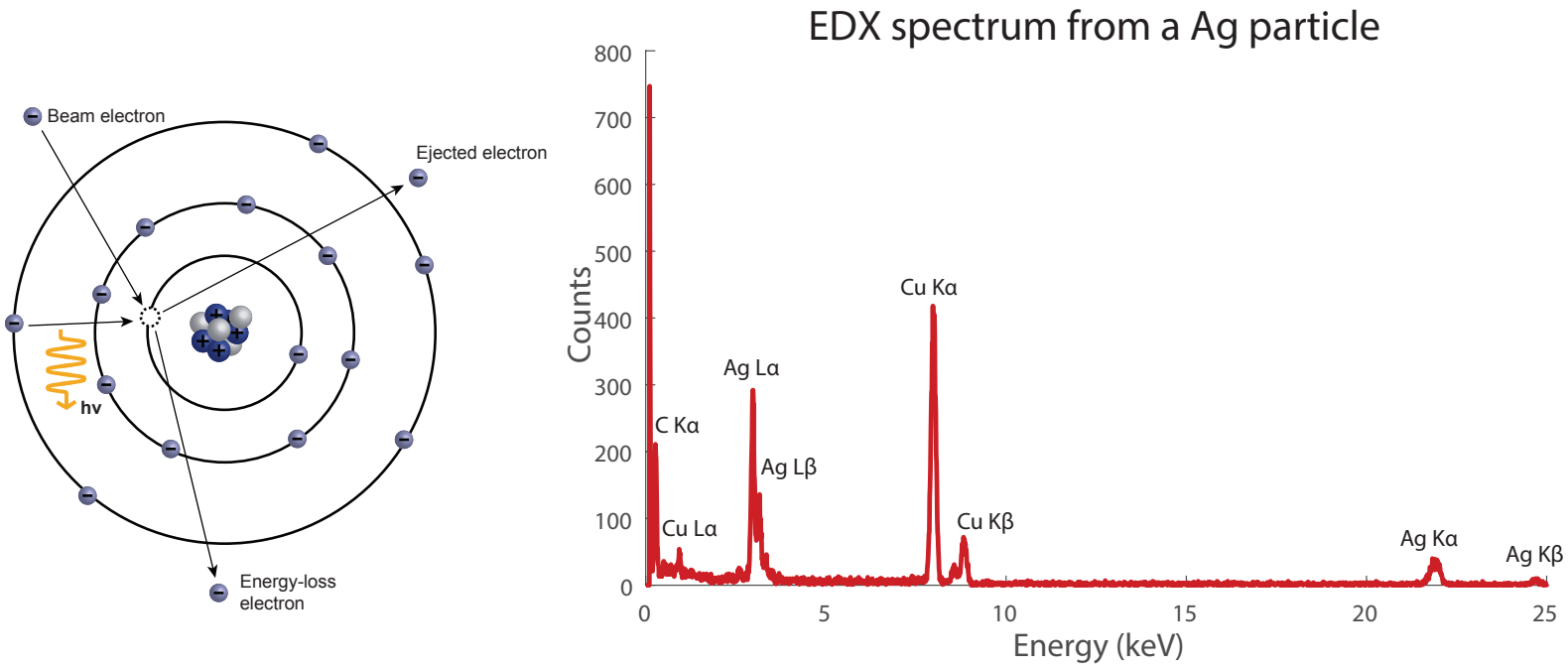

Figure 3.4: Left, schematic drawing of the process when a characteristic x-ray is generated. The electron beam excites one of the core-shell electrons. When the hole is filled by an electron at a higher energy a characteristic x-ray is generated. Right, an x-ray spectrum from a Ag particle. In the spectrum the various Ag peaks are identified and labeled. The Cu peaks originate mainly from the Cu-grid the specimen is placed on.

Equation 3.4 is only valid for thin electron transparent specimens. If a thicker or bulk specimen is to be measured the quantification is more complicated. When quantification has been performed within this work a dedicated software has been used.

In EELS we are measuring the energy loss from the transmitted beam (an example of this kind of inelastic scattering is illustrated by the energy-loss electron in Figure 3.4). The energy distribution of the transmitted beam can provide us with information about the sample such as the chemical composition, valance state and band gap. EELS and XEDS are complementary to each other since EELS can detect even lighter elements compared to XEDS.

3.3.5 Sample preparation for transmission electron microscopy

The main necesssity for using a TEM is to have an electron transparent sample. Depending on the type of nanowire analysis sample preparation might be neccessary to gain the information desired. In general there are three different ways to prepare nanowire samples. The simplest is to view a nanowire in planar view, second the sample can be prepared in cross-section to include the substrate and third the sample can be prepared for imaging of a cross-section of the nanowire itself. The three different ways to analyze and prepare the nanowires are illustrated in Figure 3.5. I will shortly describe the process of the two first ways to prepare nanowires for TEM.

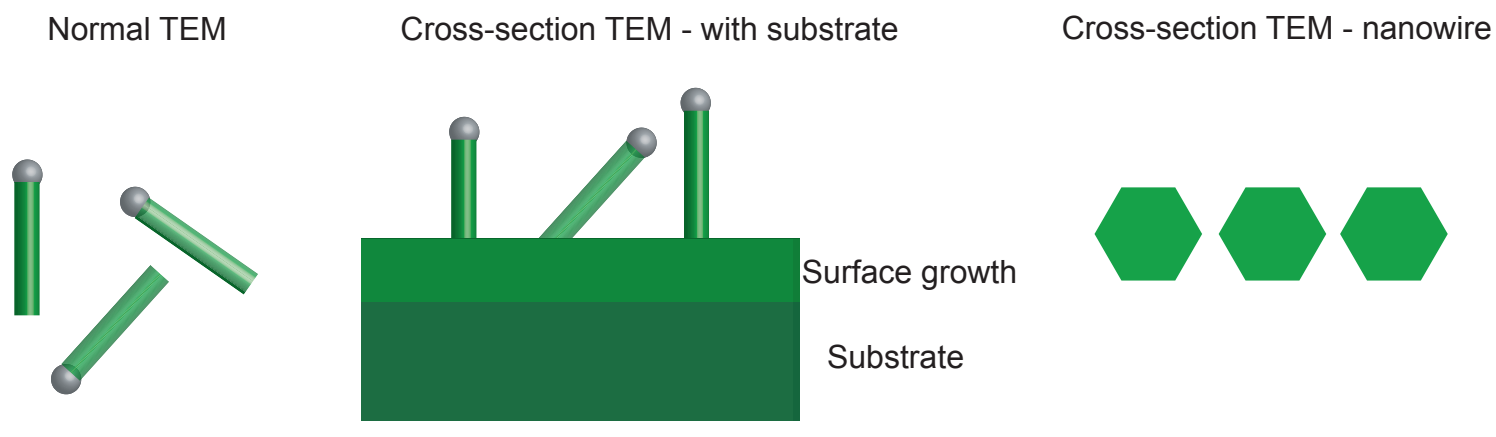

Figure 3.5: The three main ways to prepare nanowires for transmission electron microscopy. In normal TEM the nanowires are lying freely on the TEM grid. In cross-section TEM-with substrate, a part of the substrate with nanowires are thinned down until it is electron transparent. For cross-section TEM-nanowire the nanowire is cut into cross-sections for TEM imaging.

Since a single nanowire is thin enough to be electron transparent there is no need for extensive preparations for normal TEM imaging. It is sufficient to scratch a TEM grid against a substrate with nanowires. Nanowires will, by the force applied, break from the substrate and be transferred to the grid. This preparation is enough for most analysis such as investigation of the crystal structure and purity, analysis of the composition of the nanowire or analysis of the composition of seed-particle.

If the nanowire's epitaxial relationship with the substrate is to be analyzed the sample preparation is more complicated. The process outlined here is shown in Figure 3.6. First two equally sized pieces of a wafer of 4mm x 2.5mm are cut out with a diamond saw. The pieces are glued together with epoxy. The nanowires are placed so they face each other and are protected by the epoxy for the rest of the processing. A diamond wire saw is then used to cut even smaller pieces in the size of 2.5mm x 500μm. The pieces with the nicest edges are selected for continued processing. This sample is then polished to a thickness of 25 μm. The thin sample is thereafter glued to a TEM-grid with a hole in the middle. Ion milling is performed on the sample with the beam focused towards the interface between the two substrate pieces. The ion milling is stopped after a small hole is created between the substrate/epoxy. When the hole has been created there are hopefully regions close to the hole that contain nanowires and are thin enough to be electron transparent.

The third way to prepare nanowires for TEM imaging is to cut a cross-section of the actual nanowire using a focused ion beam instrument.

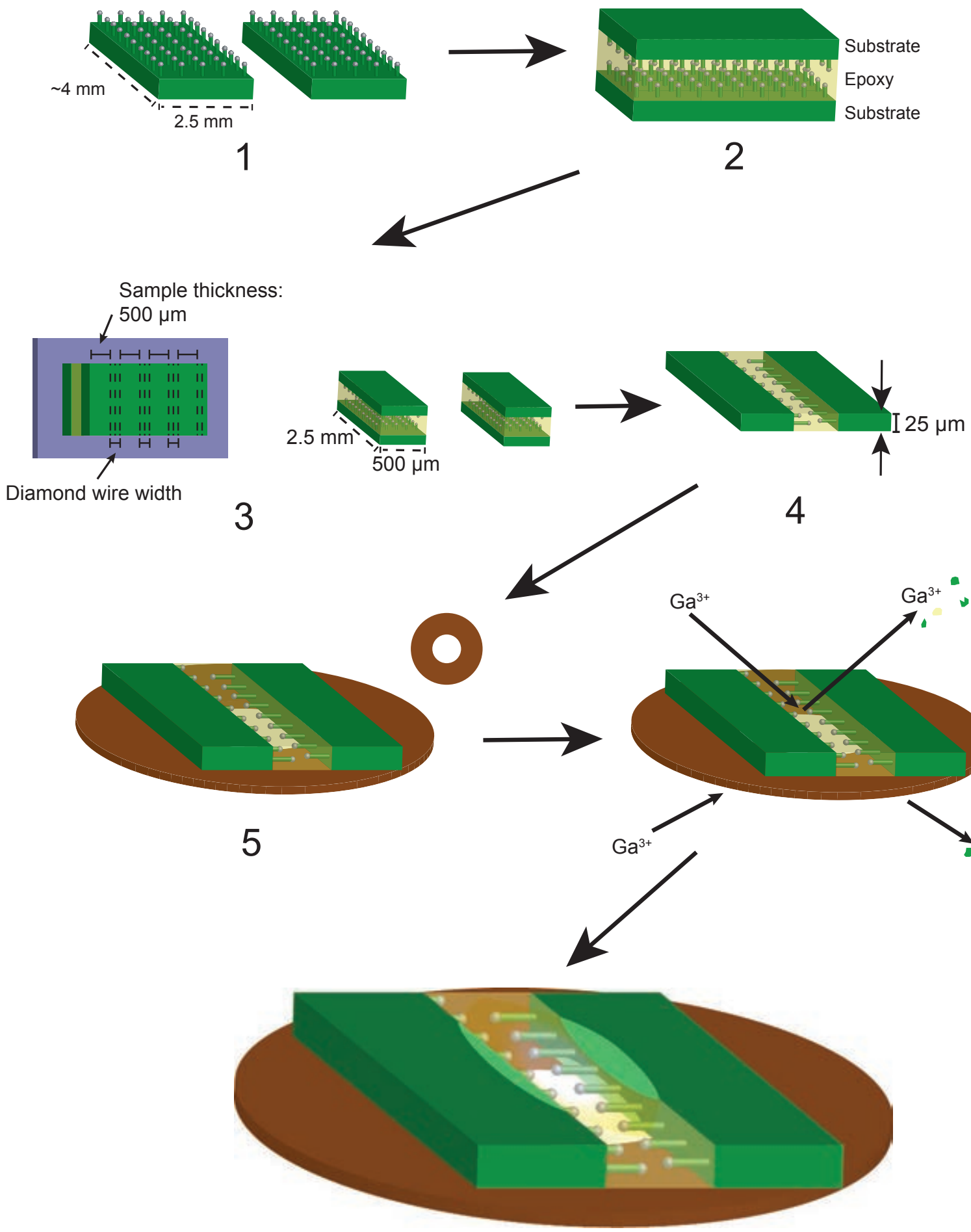

Figure 3.6: The process to prepare cross-section samples with the substrate included. 1, two equal sized wafers are cut from the sample. 2, the two pieces are glued together (nanowires facing each other) with epoxy. 3, 2.5mm x 500μm pieces are cut with a diamond saw. 4, the sample is polished down to 25μm. 5, the 25μm thick sample is glued to a TEM grid with a hole. The small ring illustrates the shape of the TEM-grid. 6, ion milling creates a hole in the sample. 7, the sample is ready for TEM measurements.

3.3.6 Transmission electron microscopes within this project

In this project several different TEMs have been used. For the planar TEM images in chapter 4 (GaAs nanowires) and chapter 6 (the Raman project) we used two different microscopes. A Philips CM20 microscope operated at 200kV located at the Niels Bohr Institute at Copenhagen University, Denmark, was used for lower magnification images. For high resolution images we used a JEOL 3000F microscope operated at 300 kV, in both TEM mode and HAADF-STEM mode, which is located at Lund University, Sweden. For the cross-section samples in chapter 4 (GaAs nanowires) and chapter 5 (InAs nanowires) we used an FEI Tecnai F20 operated at 200kV for both HRTEM, ADF-STEM and STEM-EELS mapping. The microscope is located at the Institut Català de Nanociència i Nanotecnologia (ICN2), Catalonia, Spain. On the cross-section samples we also acquired atomic resolution HAADF-STEM Cs corrected images with a FEI Titan 60-300 STEM equipment operated at 300 kV. The microscope is located at the Advanced Microscopy Laboratory (LMA) in Institute of Nanoscience of Aragon (INA), Zaragoza, Spain. For the images from the Titan it is noted in the caption of the figures.

3.4 Scanning Electron Microscopy

In scanning electron microscopy, compared to TEM, we do not measure the transmitted beam. Instead electrons that are emitted or scattered $> 90°$compared to the incident electron beam make up the image. An effect of this is that the greatest drawback with TEM, the necessity of the thin sample, is eliminated. In SEM, instead the sample needs to be conductive for the electrons to be transported away. Otherwise they may cause charging effects and induce damage to the sample. To increase the conductivity for samples such as biological ones a thin metal film can be deposited prior to imaging. III-V semiconductor nanowires are usually conductive enough to be imaged without any pre-processing. The setup of an SEM is similar to a TEM. Electrons are generated with an electron gun, the electron beam is then focused with electromagnetic lenses and the beam is scanned over the sample. Similar to TEM this produces a range of different signals see Figure 3.1. For imaging in SEM BE and SE are collected in order to construct the image. As mentioned earlier in section 3.2 BE are electrons from the electron beam that have scattered $> 90°$. These electrons are elastically scattered and hence have an energy close to that of the incident electron beam. Since this kind of scattering is proportional to the weight of the nucleus (with a heavier nucleus resulting in more BE) BE images can thus give information on the distribution of light and heavy atoms throughout a sample, with heavy elements appearing brighter compared to lighter elements. The energy of the BE depend heavily on the energy of the incoming electron beam. Due to the high energy of BE they have a relatively deep escape depth (depth from which the electrons can escape the sample) of hundreds of nm. SE form when the electrons in the incident electron beam interact with loosely bound electrons, causing the electrons to escape the attractive force of the atoms. If this occurs close to the surface of the sample the electrons can leave the sample completely giving rise to detectable secondary electrons. Due to the low energy of SE the escape depth is much smaller than for BE and only SE generated around 1-2 nm below the substrate surface will be able to escape the sample and provide surface contrast [72]. The different escape depths for different signals are illustrated by the excitation volume in Figure 3.7. SEM is the first instrument of choice when a nanowire growth

should be evaluated. It is also the instrument used when properties such as nanowire density, nanowire morphology and vertical yield is to be analyzed. When tilting the sample the length of the nanowires can be found by the simple trigonometric relation presented in equation 3.5.

$$L_{nanowire} = \frac{L_{measured}}{sin(\theta)} \tag{3.5}$$

Here $L_{nanowire}$ is the length of the nanowire, $L_{measured}$ is the measured length of the nanowire in the SEM image and θ is the tilt angle of the SEM image.

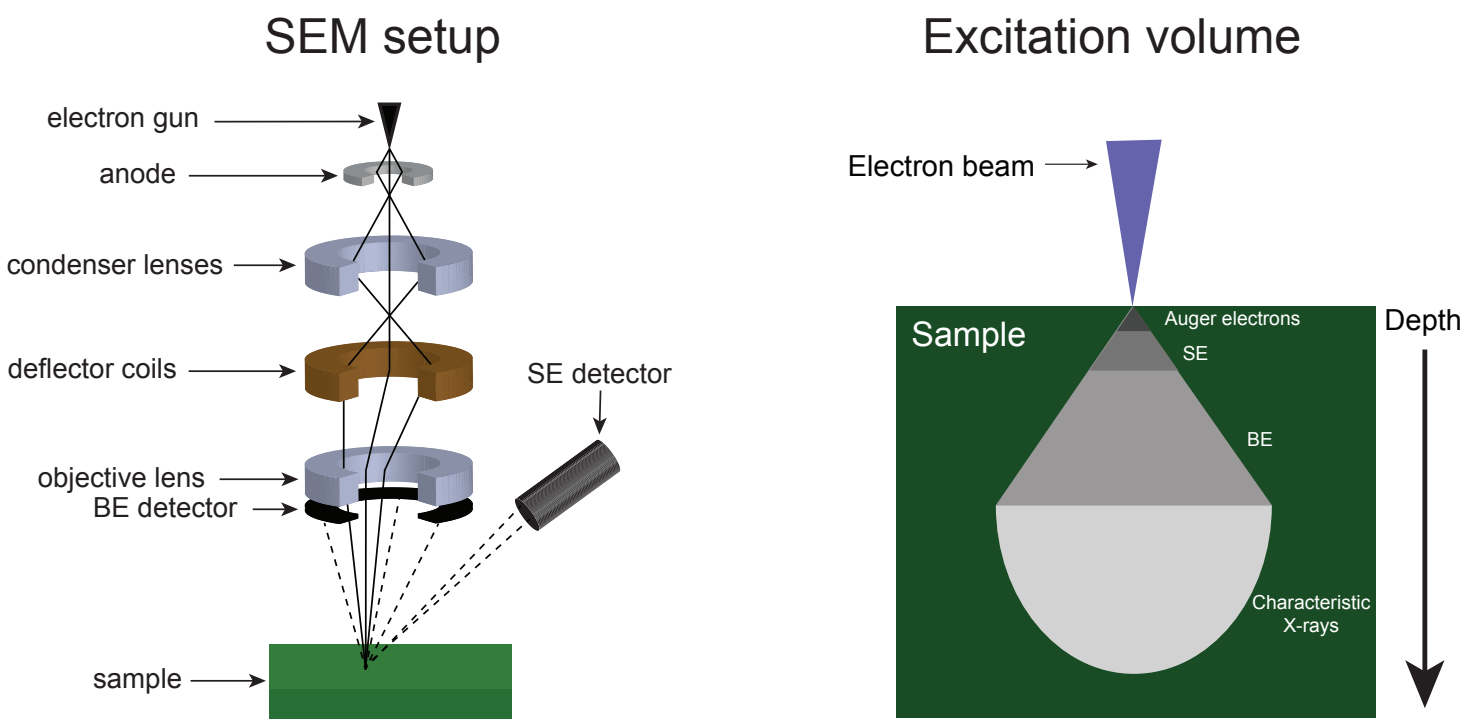

Figure 3.7: Left, the graphical setup of an SEM. Similar to STEM the electron beam is focused to a small spot and scanned over the sample. Based on the energy the electrons are divided in to BE and SE. Solid lines show the incoming electron beam, dotted lines shows scattered electrons. Right, an image of the excitation volume which illustrates from how deep different signals can escape the sample.

Chapter 4

Growth and characterization of Ag-seeded GaAs nanowires

4.1 Introduction

In this chapter I present work on Ag-seeded GaAs nanowires on both GaAs(111)B substrates and GaAs(100) substrates. Parts of this chapter are adapted from Nano Lett. 2016, 16, 2181–2188 [31]. In order to find good growth parameters for both substrates the basic growth paramaters such as As pressure, Ga flux and temperature have been varied. To gain a deeper understanding of the nucleation of GaAs nanowires on (100) substrates we also performed cross-sectional TEM on samples at different stages of growth.

Today a good control over properties such as crystal structure of GaAs nanowires grown in the <111>B direction has been achieved and many groups have investigated how to improve and control the crystal structure. The resulta is range quality from pure ZB to pure WZ for Au-seeded nanowires [69, 73, 74, 75]. SC nanowires mostly have a ZB crystal structure [76, 77] or mixed crystal structure [78]. Short segments of the 4H and 6H crystal structures have been reported in pure GaAs nanowires [79]. Slightly longer segments (but still below 20 nm) of the 4H crystal structure have also been reported in the transistion region of a Bi-induced change between ZB and WZ [80]. The 4H crystal structure is also found between ZB GaAsSb and WZ GaAs in heteroepitaxial lateral growth [81]. As mentioned all these segments are relatively short but with further research on other seed particles it might be possible to extend the segment such as for Cu-seeded InAs nanowires [28]. Even though both good control over the crystal structure and the position [82] of GaAs nanowires the same high yield of <100> nanowires as for InP [26] or InAs [14, 24] have not yet been reported for Au-seeded, SC and SAE GaAs nanowires. We therefore partly focus our research on how Ag as seed particle can affect the yield of vertical GaAs nanowires on GaAs(100) substrates and how the substrate affects the crystal structure of the nanowire.

Except for the standard unidirectional nanowires grown vertically from the substrate a few other examples of GaAs nanowire structures have been reported. These include planar nanowires [83, 84] and branched structures [85, 86].

GaAs nanowires have earlier been seeded with other particles than Au and Ga. For instance Pd particles have been used to grow vertical nanowires on GaAs(111)B substrates with MOCVD [87]. Good control over the growth direction have also been reported

for MOCVD grown Sn-seeded GaAs nanowires [88, 89]. Sun et al. [89] also report incorporation of the Sn particle into the nanowires during growth and suggest that this can be used to deliberately dope the nanowires. Besides Pd and Sn, Fe-seeded MOVPE grown GaAs nanowires have also been reported [23]. For MBE Mg has been used to seed GaAs nanowires on SiO_2 and GaAs(100) [29] and we have reported Ag-seeded GaAs nanowires [31].

4.2 Method

In this work MBE has been used to grow Ag-seeded GaAs nanowires from a thin Ag film on both GaAs(111)B and GaAs(100) substrates. For the samples presented here a 1 or 2 nm thin Ag film has been deposited onto epi-ready substrates. The substrates were, after Ag deposition, transported in ambient air to the MBE and loaded. Before moving the substrates into the growth chamber a two-step degassing procedure described in chapter 2.1 was performed. In the growth chamber the samples were first annealed at 580-600°C. This annealing was performed to remove the native oxide from the substrate and to form Ag particles with the thin film annealing method, explained in chapter 2.4. Confirmation of the oxide removal at 580-600°C was done by RHEED for the early growths. After the annealing step the temperature was lowered to the correct growth temperature and allowed to stabilise for five minutes. The growth was then started and stopped by opening and closing the Ga effusion cell. During the temperature increase and decrease an As_2 overpressure was kept, unless otherwise stated, in order to prevent evaporation of As from the substrate. In the growths presented the temperature has been varied from 400-600°C, the As pressure from $2.4 * 10^{-6}$-$1.2 * 10^{-5}$ Torr and the Ga flux from $4.1 * 10^{18}$-$7.4 * 10^{18}$ (atoms/m$^2 s$).

The experiments can be divided into several different series: First, we tested the effect of the Ga flux and As pressure at a low temperature on (100) substrates. Second, we investigated the optimum growth temperature on both (100) and (111)B substrates. Third, we tested the effect the As pressure has on growths performed on (111)B substrates. Fourth, based on the results from the temperature series we also made a second Ga flux test on (100) substrates at a higher temperature. Finally we performed a growth time series on (100) substrates. For an extended list over samples and growth parameters see Appendix A.

After growth the samples were analyzed with SEM and TEM to find morphology, vertical yield and the crystal structure for the different nanowires.

4.3 Results and discussion

4.3.1 As pressure and Ga flux dependence on (100) substrates

Figure 4.1 shows the results for nanowires grown at 400°C on (100) substrates at two different Ga fluxes and two different As_2 pressures. The density of nanowires differs greatly over the substrate, probably due to the temperature difference (see chapter 2.1) on the substrate during growth. However nanowires have nucleated steadily everywhere on all four samples.

At the higher As_2 pressure $1.2{*}10^{-5}$ Torr a higher Ga flux promotes a higher density of nanowires, see Figure 4.1 a) and b). We attribute the higher density of nanowires (with

a high Ga flux) to an increased Ga supersaturation in the Ag particle. However, when a lower As_2 pressure is used we could not find the same obvious increase of nanowire density with the Ga flux, see Figure 4.1 c) and d). This can be explained by the increased diffusion length of the Ga atoms with a decreased As_2 pressure [90]. When the Ga diffusion length is increased by a lower As_2 pressure more Ga can diffuse to a Ag particle. This will increase the supersaturation of the Ag particle for the sample with both a lower Ga flux and As_2 (compared to the sample with a high As_2 pressure) and decrease the difference in nanowire density between a low and a high Ga flux.

As seen, on all four samples, the nanowires grow in many different directions. Analyzing top view images we could not find any preferred crystal directions. We do however note that isolated nanowires have grown in the [100] direction.

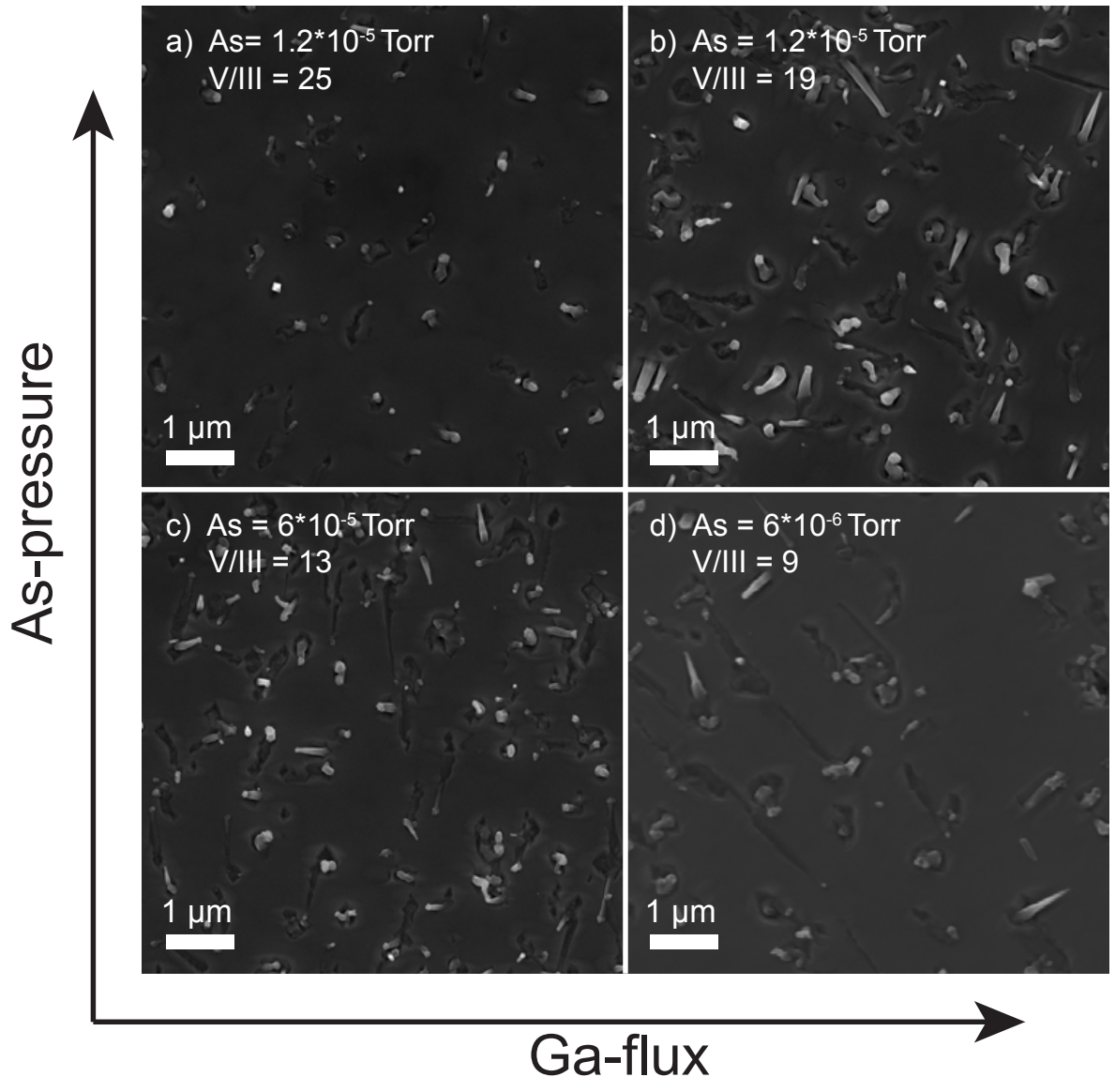

Figure 4.1: Varying Ga fluxes and As_2 pressures for Ag-seeded GaAs nanowires at 400°C. All SEM images are in top view.

4.3.2 Temperature dependence

To find optimum growth temperatures, a temperature series was performed on both (100) and (111)B substrates. For these series a V/III ratio of around 9 and an As pressure of $6*10^{-6}$ Torr was used.

Figure 4.2 shows the results for the temperature series on (100) substrates. The temperatures were set to 400°C, 550°C, 575°C and 600°C. The two lower temperatuers (400°C and 550°C) were grown for 30 min while the two higher temperatures (575°C and 600°C) were grown for 60 min. Growth at the lowest temperature, 400°C, resulted in nanowires grown in different directions and with a mixture of different morphologies.

At 550°C the sample showed mostly particles with a low density of nanowires scattered throughout the sample. At 575°C there were no particles and a surprisingly high yield of 45-50% vertical nanowires. Increasing the temperature even further to 600°C caused all nanowire growth to cease. For the three higher temperatures the surface showed a distinct wave-like pattern (most clearly seen in the image for 550°C). In the layer growth at 600°C a low density of elongated six facetted pits was also present, see the top view image for 600°C in 4.2. Both the waves and the pits are common defects in film growth of GaAs on (100) substrates, see [91] and references therein. However for our growths the waves only formed where we had deposited Ag particles [92]. The impact of the different growth times in the temperature series will be further elaborated in section 4.3.4.

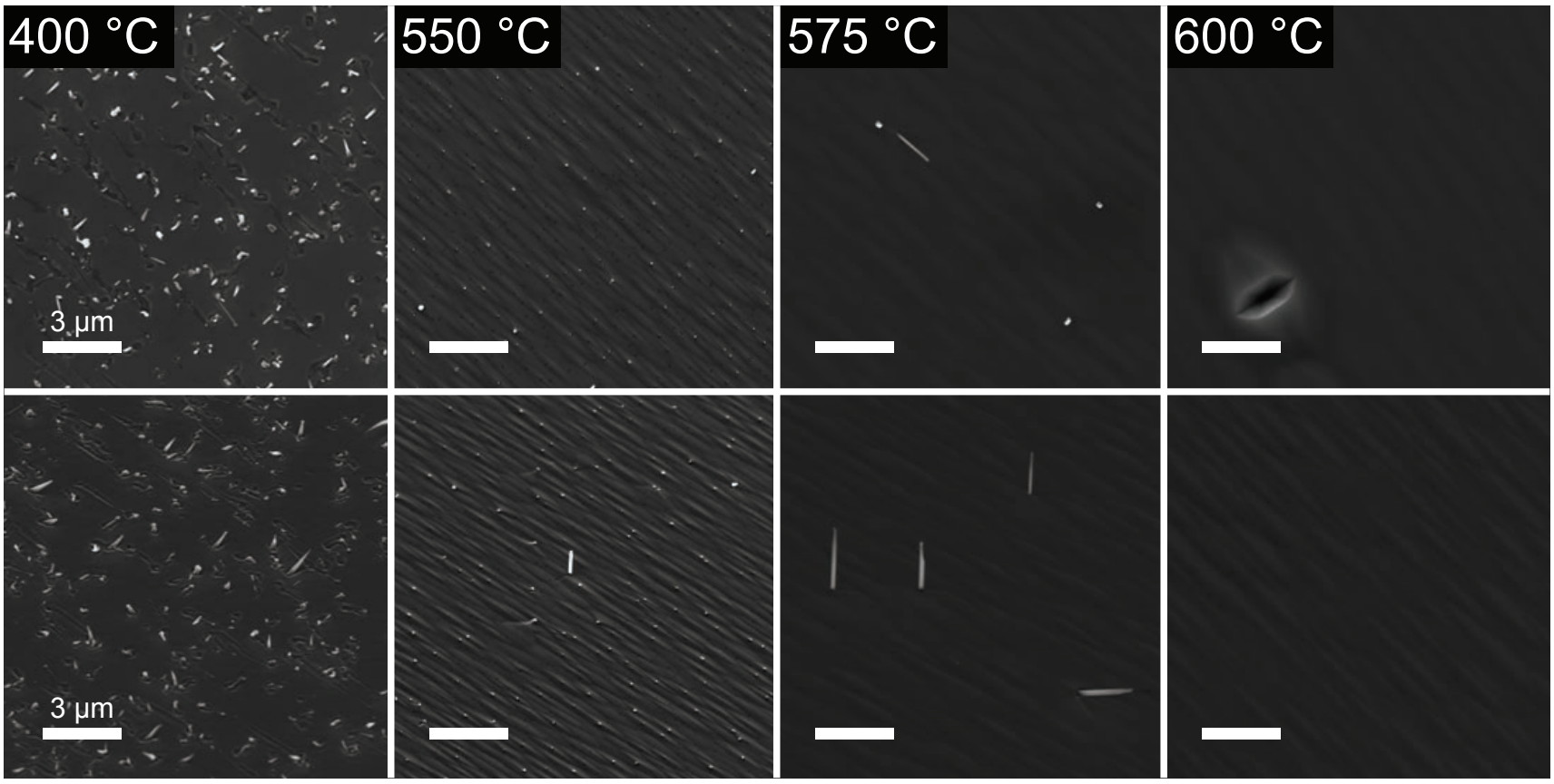

Figure 4.2: Ag-seeded GaAs nanowires grown on GaAs(100) substrates at four different temperatures. Upper images are in top view, bottom images are imaged at 45° tilt.

The morphology of the vertical nanowires grown at 575°C can be seen in Figure 4.3. The top view images reveal a rectangular cross-section indicating a pure ZB crystal structure [26]. By correlating the facets of the nanowires to the substrate we conclude that the facets are <110> type. The top view shape of the nanowires can be both close to a square, Figure 4.3 a) and b), or elongated in one of the <110> directions, Figure 4.3 c) and d). The elongations are visible for both <110> type cleaving directions of the substrate excluding a favorable surface growth of two facets as the only reason for the widening of the nanowires.

For the (111)B substrate the temperature was varied from 400°C to 600°C in steps of 50°C. All samples were grown for 30 min and the results are seen in Figure 4.4. Nanowire growth occured over the whole temperature range tested. At the lower temperatures (T<550°C) the nanowires grew in different directions and could exhibit kinks and similar morphologies, similar to what was seen on (100). With increasing temperature the yield of vertical nanowires increased and at the highest temperature 600°C all nanowires grew in a vertical manner relative the substrate. This should be compared to (100) where the nanowire growth had totally ceased at this temperature. While the vertical yield increased with higher temperatures the total density of nanowires decreased. At the

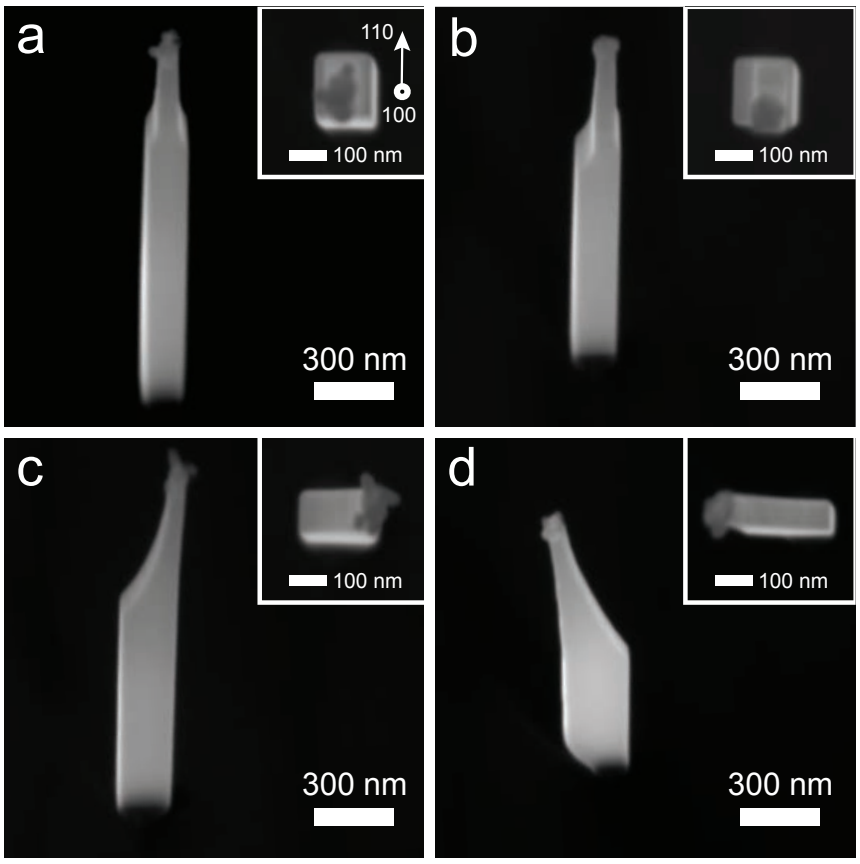

Figure 4.3: The different morphologies of vertical nanowires that have grown on a (100) substrate. The images are acquired at 20° tilt, insets are top view images of that particular nanowire. All images are acquired in the same direction indicated in top view in a).

lowest temperature 400°C the nanowire density was 0.85 nanowires/μm^2 while at 600°C the nanowire density had decreased to 0.02 nanowires/μm^2.

As mentioned earlier growth for 30 min on (100) substrates at 550°C generated mostly particles and only a low density of nanowires. On the other hand on the (111)B substrate the same growth conditions resulted in a relatively high density of nanowires and no particles were observed. So on the (111)B substrate all particles have either nucleated and formed nanowires or become buried in the early stages of nanowire growth.

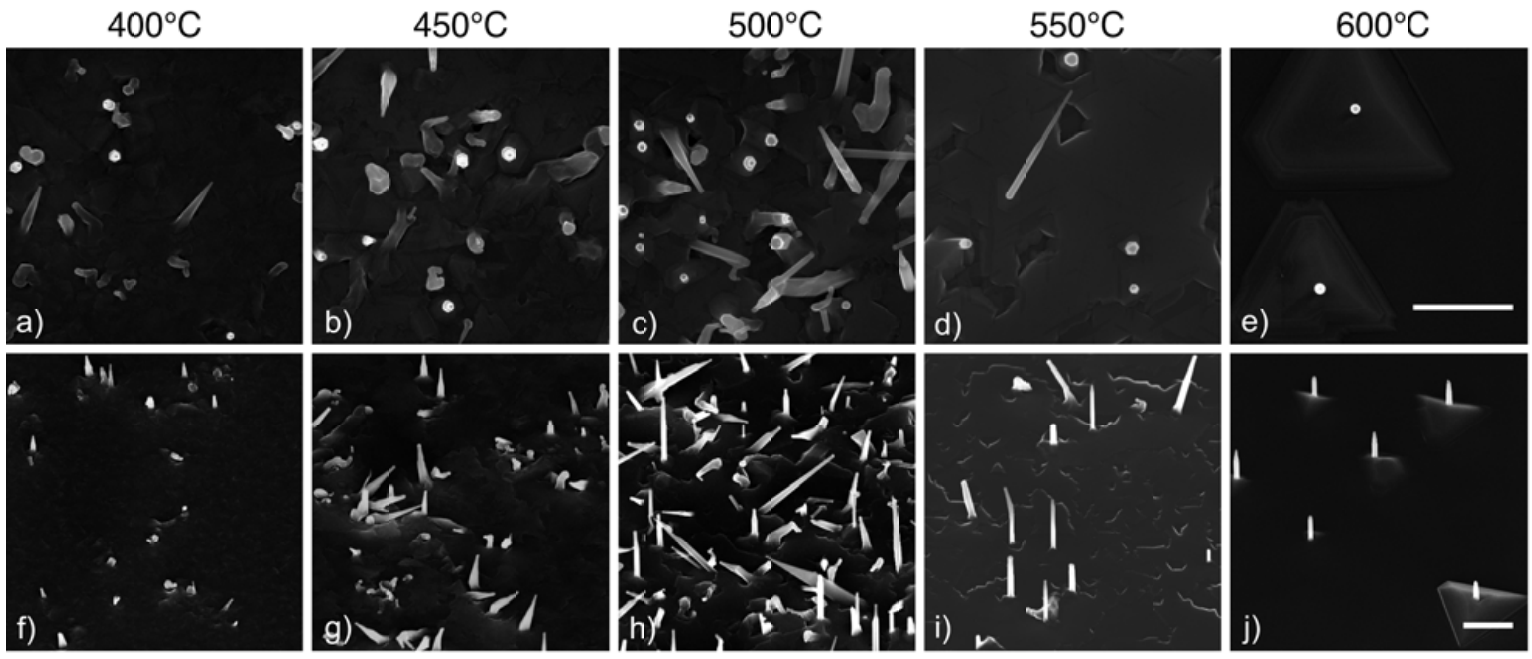

Figure 4.4: Nanowires grown on (111)B substrates at five different temperatures. The nanowires develop from mostly inclined nanowires with different morphologies to all vertical nanowires at 600°C. The top images are viewed at 0° tilt and the bottom images are viewed at 45° tilt. The scale bars are 1μm. Image adapted from Nano Lett. 2016, 16, 2181–2188 [31]

The trend continues at 600°C where no nanowire growth is observed on the (100) substrate but on the (111)B substrate the nanowire growth is stable. The cut off temperature is also different. While 600°C gave the best yield of vertical nanowires on (111)B substrates no nanowires at all grew on the (100) substrate. This shows that at the higher temperatures the nucleation is more stable on (111)B substrates than (100) substrates.

4.3.3 As dependence on the (111)B substrates

For the completeness of the study we have varied the As_2 pressure on three different samples. For this series we kept the temperature at 550°C and the same Ga flux as in the temperature series described in the previous section. The As_2 pressure was set to $2.4*10^{-6}$, $6*10^{-6}$ and $1.2*10^{-5}$ Torr. SEM overview images did not reveal a big difference between the samples and all three samples looked similar to Figure 4.4 d) and i). However further analysis of the particle sizes versus the length of the nanowires revealed a difference between the samples. The results are presented in Figure 4.5. For the two samples grown with high As_2 pressures the length follows the trend of smaller particles yielding longer nanowires (red crosses and blue circles) explained by material transport models [93, 94, 95]. For the lowest As_2 pressure this trend is broken. Instead of smaller particles yielding longer nanowires the length of the nanowires are close to constant regardless of the seed particle size (green diamonds). This phenomenon was recently modelled by Dubrovskii [96]. When decreasing the As_2 pressure from $6*10^{-6}$ to $2.4*10^{-6}$ we move from a Ga transport limited regime to a more nucleation limited regime. Even though it is beyond the scope of this work it would be interesting to investigate the crystal structure for the different growths. This since Dubrovskii [96] reports that the Au-seeded GaAs nanowires switched from a WZ to a ZB crystal structure when moving from a transport limited regime to a nucleation limited regime.

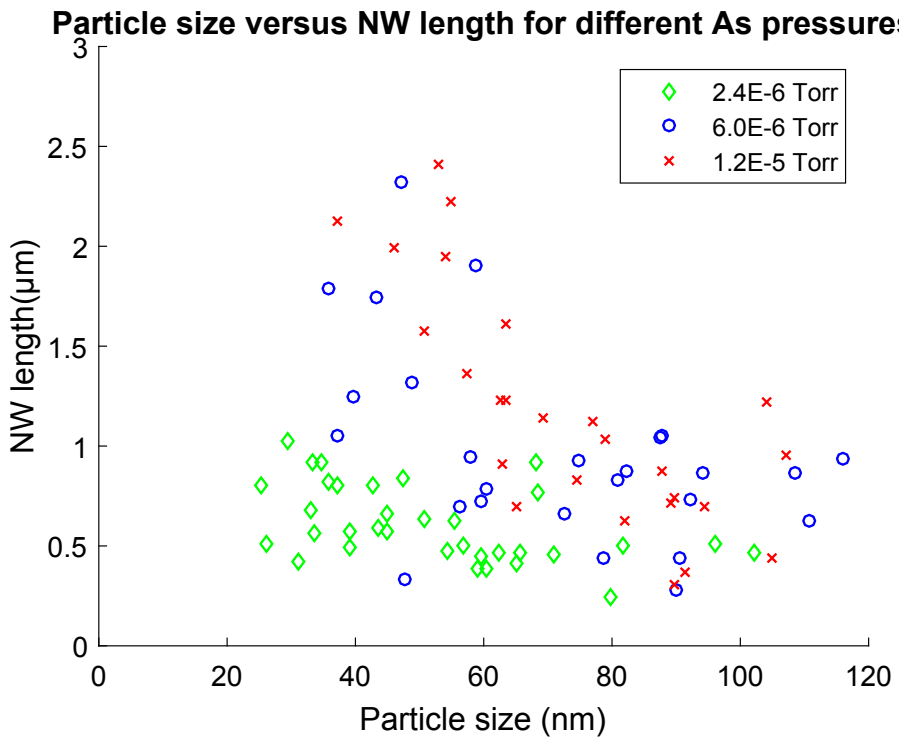

Figure 4.5: Particle size versus nanowire length for different As_2 pressures. Every data point represents the length and particle size for one nanowire. When decreasing the As_2 pressure to $2.4*10^{-6}$ Torr long nanowires with small particles disappear.

4.3.4 Ga flux and growth time dependence at higher temperatures on GaAs(100)

Puzzled by the low yield and the cut off temperature on the (100) substrates we continued to investigate growth on (100) substrates at high temperatures. This by performing another Ga flux test as well as a growth time series.

Two samples with the same temperature, around 575°C, and the standard As_2 pressure $6*10^{-6}$ but slightly different Ga fluxes, corresponding to V/III ratios of 9 and 8, respectively, were grown. Both samples were grown for 30 min and SEM images can be seen in Figure 4.6. Note that the sample shown in a) and c) has the same V/III ratio as the temperature series. Both samples showed mostly particles and a low density of nanowires. The density of nanowires was calculated from images tilted to 45°, in order to distinguish between short nanowires and particles. The particle size and density was measured on top view images using ImageJ. The density of nanowires increases from 0.3 nanowires/100μm^2 to 2.0 nanowires/100μm^2 with the increased Ga flux. The particle density is however constant on 240 particles/100μm^2 while the average particle size increases from 80±30 to 100±40 nm with the higher Ga flux. The maintained particle density together with the increase of particle size could be due to an increase of Ga content in the Ag particles and hence a higher supersaturation. This confirms that by increasing the Ga flux we probably increase the Ga supersaturation in the particles and thus promote nanowire growth resulting in the higher density of nanowires.

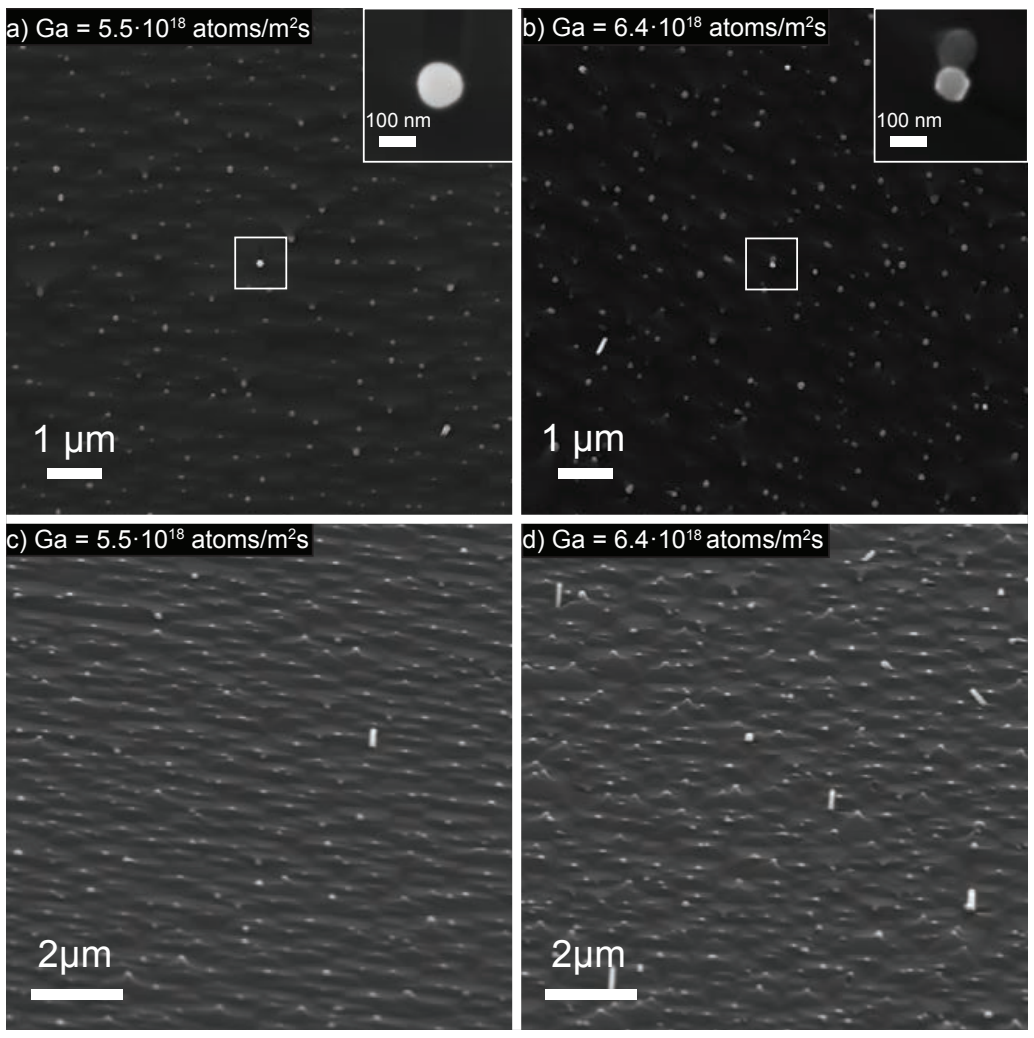

Figure 4.6: The difference in nucleation on a (100) substrate with Ga flux. a) and c) the sample grown with a lower Ga flux, b) and d) the sample grown with a higher Ga flux. The upper images are top view images with the inset of a vertical nanowire. The images at the bottom are at 45° tilt.

The time series is based on three samples grown for 4 min, 20 min and 60 min. For these growths we used the same temperature and As_2 pressure as the Ga flux series above. The Ga flux is slightly increased, to a V/III ratio of 7, to further promote nanowire nucleation. The sample grown for 4 minutes only resulted in particles on the surface. The particles have an average size of 25 ± 10 nm and a density of 15 particles/μm^2 see Figure 4.7 a). The sample grown for 20 minutes showed mostly particles and a low amount of nanowires. The average nanowire density for the 20 min sample was 0.05 nanowires/μm^2, see Figure 4.7 b). For the sample grown for 60 min the particles had completely disappeared and the nanowire density had increased to 7.2 nanowires/μm^2, see Figure 4.7 c).

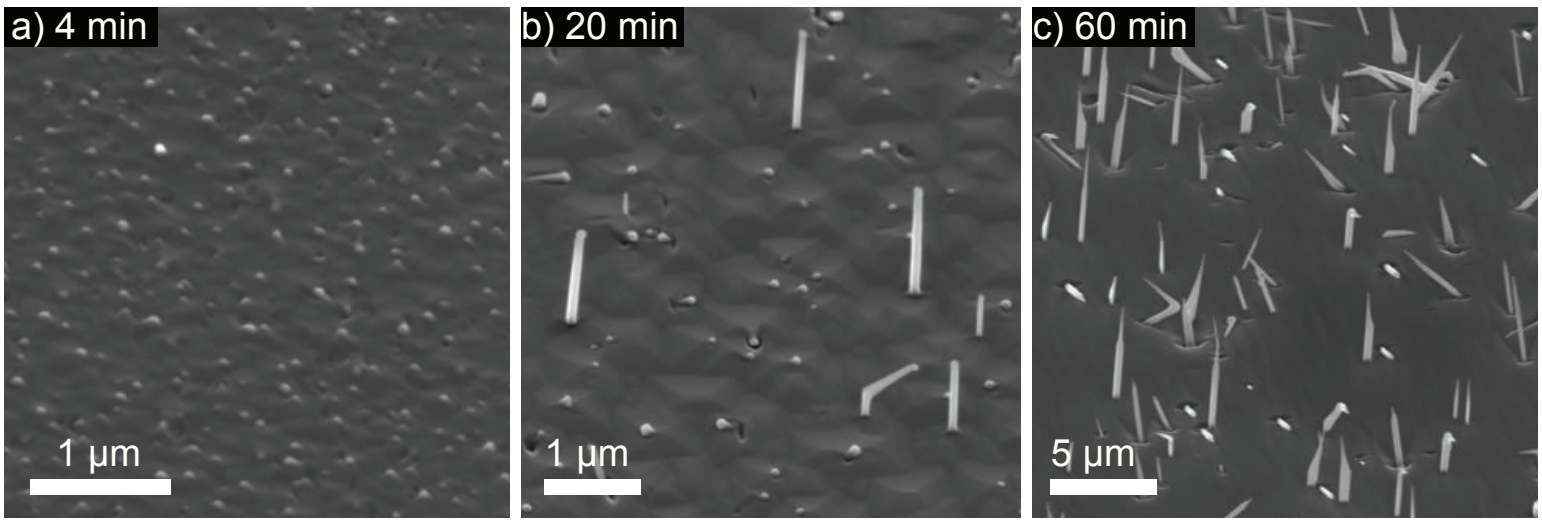

Figure 4.7: Growth of Ag-seeded GaAs nanowires on (100) substrates for 4 min, 20 min and 60 min respectively. Images acquired at 45° tilt. Note the different scale bars due to the big difference in size between the particles and the nanowires.

The big difference in nanowire density between the sample grown for 20 min compared to the sample grown for 60 min shows the long nucleation time for nanowires grown on (100) substrates. We also have a decrease between the number of particles visible after 4 min and the number of nanowires grown for 60 minutes. The decrease of particles compared to nanowires with time shows that not all particles visible after 4 min growth form visible nanowires after 60 min. This can have two different explanations: The number of particles can decrease due to Ostwald ripening or coalescence before nucleating or the particles get buried below layer growth. By assuming that all particles are half spheres, the average density and the average size of the particles are used to calculate a corresponding thin film thickness, see equation 4.1

$$t_{film} = \frac{4\pi}{3} \cdot \frac{r_a^3}{2} \cdot \frac{\delta}{10^6} \tag{4.1}$$

Where t_{film} is the film thickness in nm, r_a is the average particle radius in nm, δ is the average density of particles in particles/μm^2 and 10^6 is to get the final film thickness in nm instead of μm. The particle volume after 4 min of growth corresponds to a thin film of 0.5 nm and then we have not accounted for any Ga inside the particles. Since all samples grown in the time series had a starting film thickness of 1 nm Ag we draw the conclusion that after 4 min of growth at least half the volume of Ag has either been buried under layer growth or evaporated.

The results from the time series give new insights to the temperature series on (100) substrates in section 4.3.2, Figure 4.2. To further discuss the implications of the time

series on the temperature series we will quickly review the results for the temperature series. At 400°C there was a high density of nanowires and all particles looked like they had nucleated. Increasing the temperature to 550°C for the same growth time of 30 min we instead had particles on the substrate with only a low density of nanowires. However the time series shows that the growth time plays a major part in the density of nanowires and particles. Since the growth at 550°C in the temperature series and the growth for 20 min in the time series are similar to each other where both samples exhibit both particles and nanowires, increasing the growth time for the growth at 550°C in the temperature series would probably result in a higher density of nanowires and a disappearance of the particles. Since there are no particles present for the growth at 400°C even with 30 minutes growth time the nucleation of nanowires seems to be easier at lower growth temperatures. This is probably due to fewer Ga atoms desorbing from the surface. For the two higher growth temperatures, grown for 60 min, no particles are present. Most likely all particles that have not nucleated fast enough have been buried by layer growth. So the lower density of nanowires at 550°C compared to 575°C is due to the growth time (not all nanowires have nucleated) rather than the temperature. At 600°C on (100) substrates the nanowires do not nucleate and/or grow fast enough to not get buried by layer growth. At higher temperatures the evaporation rate of Ga on the substrate is higher than at lower temperatures [47]. This will decrease the diffusion length of the Ga atoms on the (100) surface and the effective Ga pressure experienced by the particle. With a lower Ga pressure the supersaturation of the particles will decrease and nucleation will either not take place at all or be too slow for the nanowires to grow faster than the layer growth. It is, however, at the high temperatures (and thereby high evaporation of Ga atoms) that we achieve a high yield of vertical nanowires (45-50 %). Without any further processing of substrates and/or nucleation steps we have a trade off between a high yield of vertical nanowires and a high density of nanowires.

4.3.5 Crystal structure for Ag-seeded GaAs nanowires

TEM was performed on nanowires grown on (111)B substrates at 600°C for 60 min, since these nanowires showed a 100% yield of vertical nanowires. The crystal structure consists of pure WZ grown in the <0001> direction. Close to the seed particle the nanowires exhibit a so called cooling neck [55] consisting of a more mixed crystal structure, see Figure 4.8. TEM on vertical nanowires grown on (100) substrates instead showed a pure ZB crystal structure grown in the <100> direction, Figure 4.9. While the particle-metal interface for the WZ nanowire is the (0001) plane, perpendicular to the growth direction, the particle-metal interface for the ZB nanowire is not the (100) plane. Instead the nanowire depicted in Figure 4.9 has an angle of 14° between the (100) plane and the plane of the particle-metal interface. This could correspond to the (115) or (116) planes which have an angle of 15.8°and 13.3°, respectively, with respect to the (100) plane.

We confirmed the composition of the particle with post growth XEDS on nanowires grown on both (111)B substrates and (100) substrates. The XEDS quantification is similar on both types of nanowires and the results are presented in Figure 4.10. The particle is almost pure Ag and only a low amount of 1 at% of As is detected inside the Ag particle. However no Ga was detected inside the Ag particle. This can be compared to the 25% of Ga detected inside a Au particle after GaAs nanowire growth with MBE [97]. XEDS was also performed on the nanowire stems, showing no detectable amounts

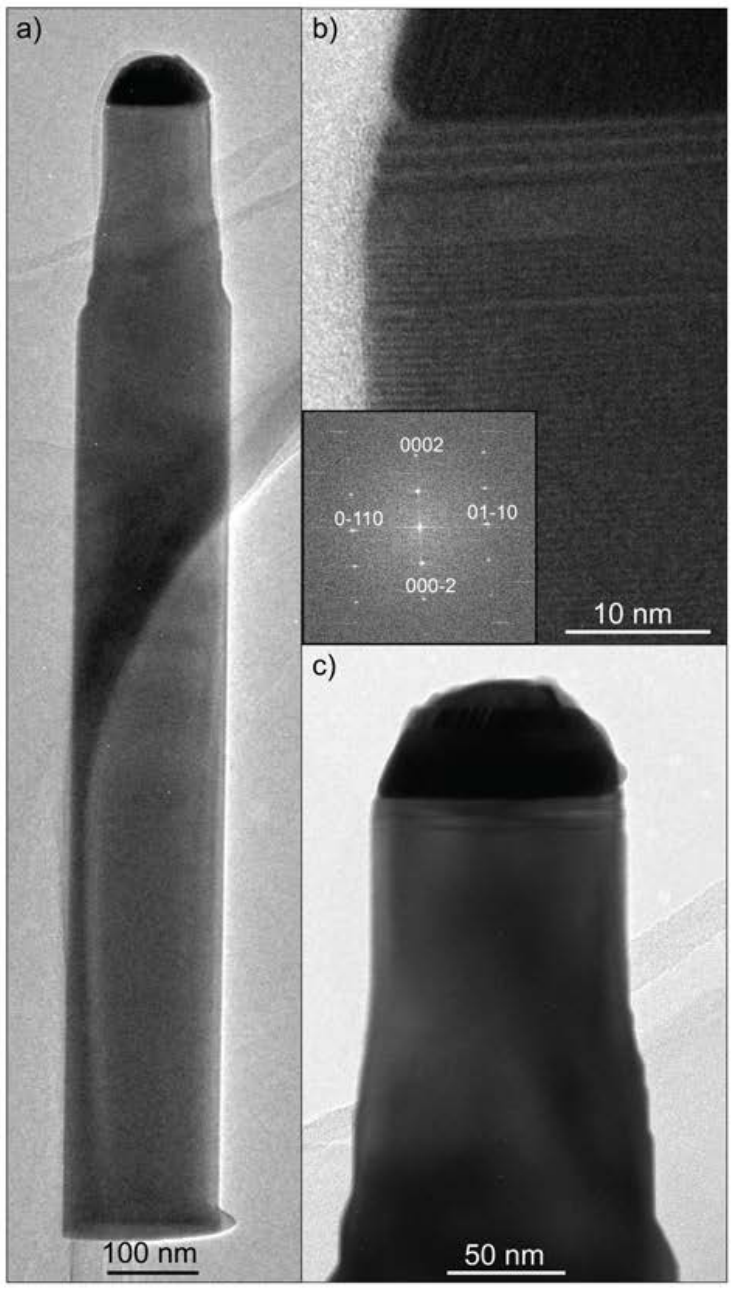

Figure 4.8: TEM image of a Ag-seeded GaAs nanowire grown on a (111)B substrate. The nanowire exhibits a pure WZ crystal structure with a cooling neck close to the particle. The nanowire is imaged in the zone axis $[2\bar{1}\bar{1}0]$. The image is adapted from Nano Lett. 2016, 16, 2181–2188 [31] and a photoluminescence spectrum has been edited out.

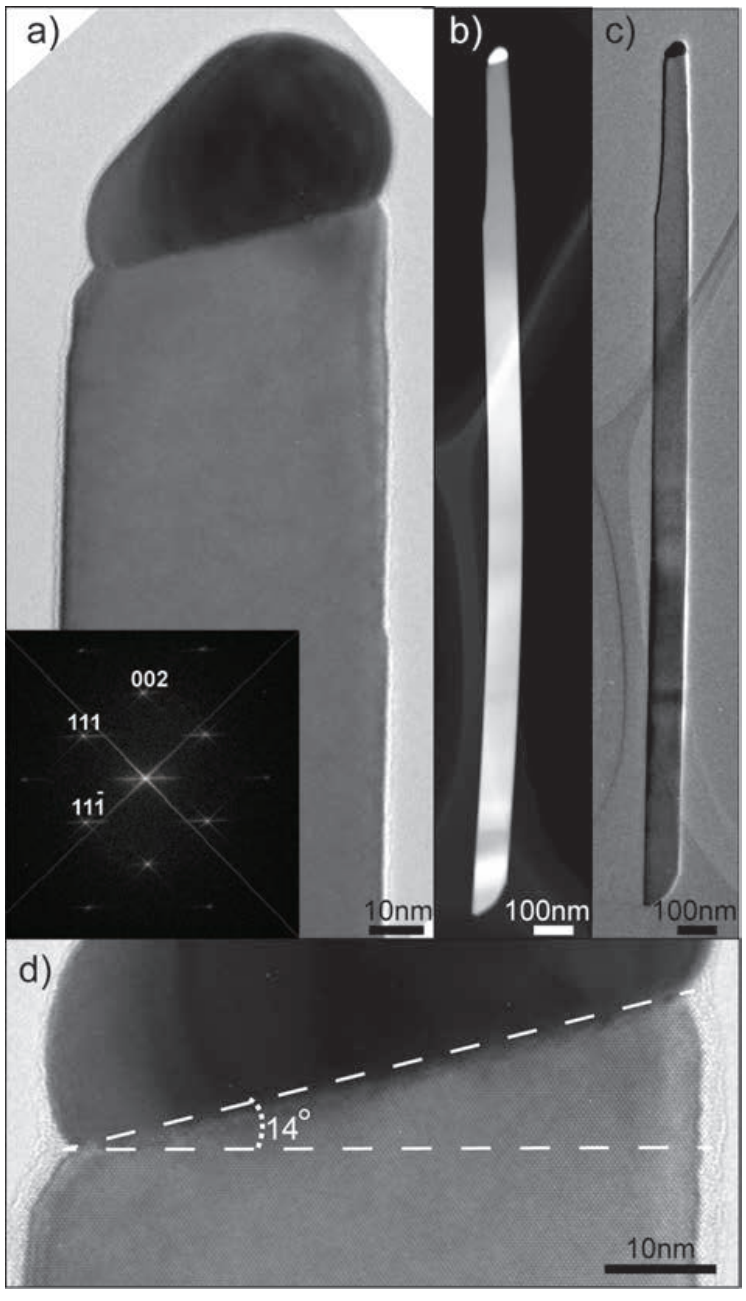

Figure 4.9: TEM image of a vertical Ag-seeded GaAs nanowire grown on a (100) substrate. The nanowire shows a pure ZB crystal structure. The image is acquired in the $[\bar{1}10]$ zone axis. The image is adapted from Nano Lett. 2016, 16, 2181–2188 [31]

of Ag inside the nanowires.

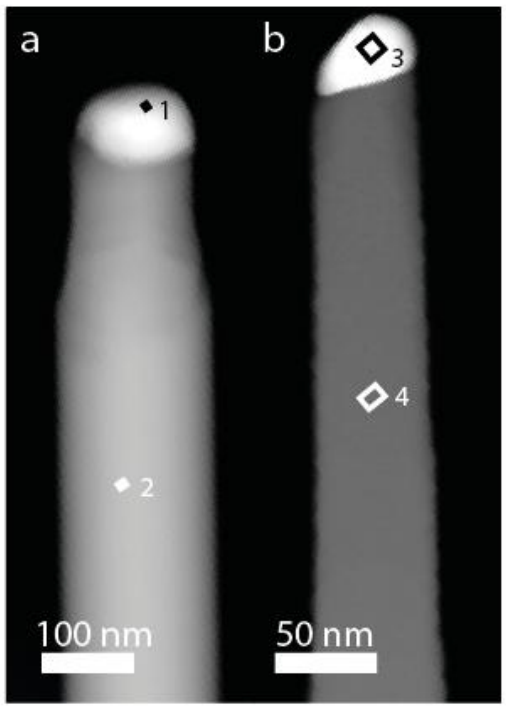

Spectrum	Ag (at%)	Ga (at%)	As (at%)
1	99	0	1
2	0	49	51
3	99	0	1
4	0	48	52

Figure 4.10: HAADF-STEM images on one (111)B nanowire a) and one (100) nanowire b) and the corresponding XEDS data. The squares show where the XEDS scans have been acquired. The XEDS reveal no Ga inside the Ag-droplet but a low, around 1 at%, amount of As. No Ag was detected inside the nanowires. The image is adapted from Nano Lett. 2016, 16, 2181–2188 [31]

The cooling neck phenomenon is attributed to Ga residues inside the seed particle when the growth is stopped. After the growth has been halted, the Ga residues inside the seed particle crystallize together with the As in the As overpressure usually kept in the growth chamber during heating and cooling of the substrate. This results in a short growth segment of the nanowire, grown under different conditions than during the actual nanowire growth. This extra segment, close to the seed particle, shows a high density of defects [55]. The obvious cooling neck in Figure 4.8 b) and c) indicates that some precipitation did occur while cooling. Thus the particle might contain Ga during growth even though none was seen in the post-growth XEDS measurements. To get more accurate XEDS measurements we performed one growth on (111)B substrates at 600°C where the Ga and the As shutters were closed simultaneously. This in order to keep the Ga inside the particle during cooling. This cooling procedure has, for MBE grown Au-seeded GaAs nanowires, been shown to remove the cooling neck and increase the post-growth Ga content in the particle measured with XEDS from ∼25 at% to ∼50 at% [97]. XEDS on our nanowires cooled without the As_2 overpressure showed no big difference compared to the our normal growth procedure. Further TEM investigation of the growth revealed that even though the As shutter was closed when the growth was stopped the nanowires still exhibit a cooling neck, see Figure 4.11.

To gain further understanding on what is happening we measured the length of the cooling neck in correlation to the diameter of the nanowire tip, for both the samples cooled with and without an As_2 overpressure. The results are presented in Figure 4.11. As seen the sample cooled without As_2 overpressure (blue crosses in Figure 4.11 c) seems to follow a linear dependence while the sample cooled under an As_2 overpressure (red crosses in Figure 4.11 c) does not show this linear dependence. While doing supply interruption method growth Bolinsson et al. [98] report a similar dependence between

WZ segments and the particle size. They relate this dependence to the fact that size of the Au particle is proportional to r^3 while the grown segments are proportional to r^2. In the supply interruption method the growth takes place in the same way as for a cooling neck. This results in a linear dependence between the particle size and the amount of growth after the TMI supply has been stopped [98]. As mentioned earlier, for Au-seeded GaAs nanowires a post-growth particle composition is reported to have ∼25 at% Ga when the nanowire growth is cooled under As pressure. This together with the low solubility of As in Au has lead to the general assumption that the group III in the particle nucleates with the As overpressure creating the cooling neck. However as seen in Figure 4.11 c) we have this linear dependence for the sample where the As supply is interrupted when the growth stops but not when we keep the As pressure. This indicates that it is the As content inside the particle that is limiting the cooling neck growth when both growth species are interrupted and not the group III content. When only the group III pressure is stopped (red crosses in Figure 4.11) no such linear dependence can be seen. The cooling neck for Ag-seeded GaAs nanowires is therefore probably not only due to group III content inside the particle but also to group V content inside the particle. The presence of a cooling neck on both samples indicates that we can have both a higher As and Ga content inside the particle during growth, compared to what is measured in post-growth XEDS.

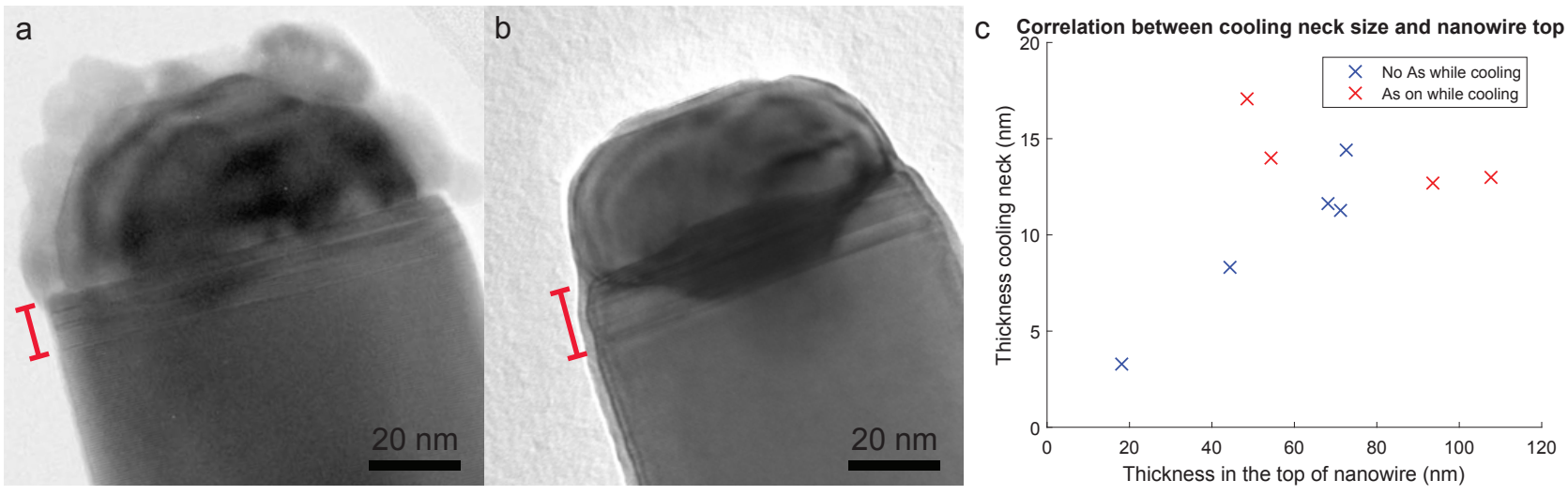

Figure 4.11: Top of nanowires cooled down with an As_2 overpressure a) and without an As_2 overpressure b). Both growths show a so called cooling neck (marked in red in the images) close to the particle. Both nanowires are imaged in the $[2\bar{1}\bar{1}0]$ zone axis. c) the correlation between the top of the nanowire and the length of the cooling neck.

When growth was performed for longer times (t≥45 min) on (111)B substrates at high temperatures we also noted another type of nanowire. These nanowires showed no Ag particle in the top, instead three facets were distinguished in the SEM images, see Figure 4.12. TEM on these nanowires revealed a clean WZ structure in the bottom of the nanowire with an increasing amount of crystal defects closer to the top, see Figure 4.13. XEDS on this nanowire showed no Ag residues neither in the middle of the nanowire nor in the top of the nanowire. We believe that these nanowires nucleated with a Ag particle in the top. With longer growth times the Ag particle became unstable and either migrated away along the sidewalls of the nanowire [99] or evaporated as suggested by reference [35], leaving the nanowire halted in its growth process and with a facetted tip.

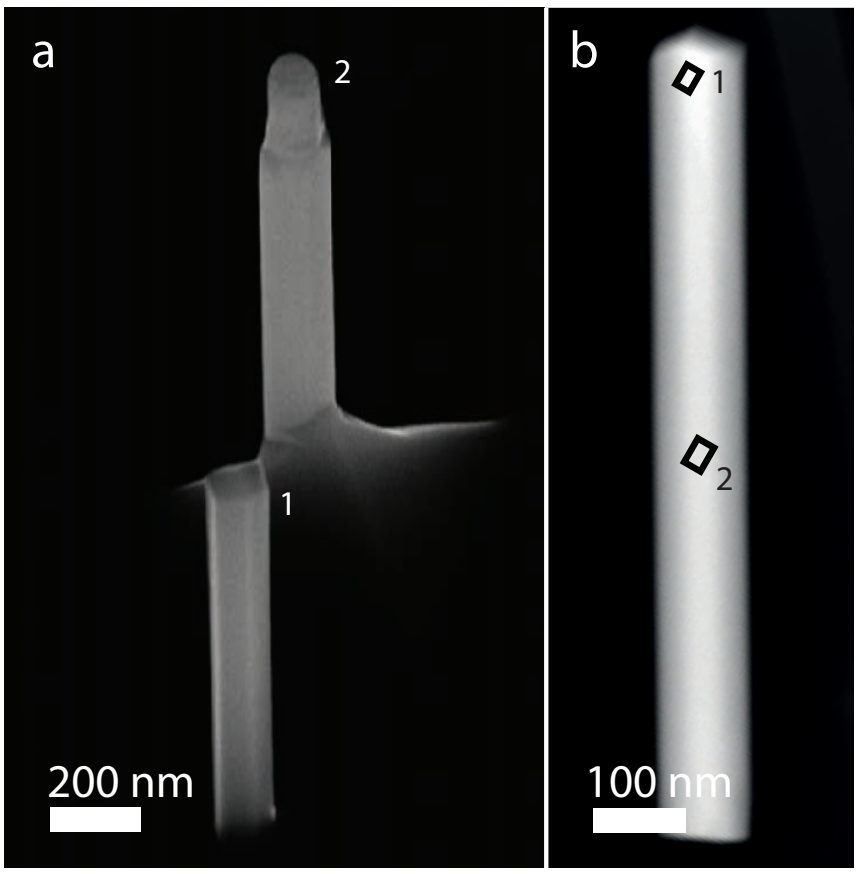

Figure 4.12: a) SEM image over 1. Nanowire with a facetted tip, 2. Nanowire with a Ag particle. b) HAADF image of a facetted nanowire. The black boxes show where XEDS has been acquired. The facetted nanowires were present when growing on (111)B substrates for a longer time. Image adapted from Nano Lett. 2016, 16, 2181–2188 [31]

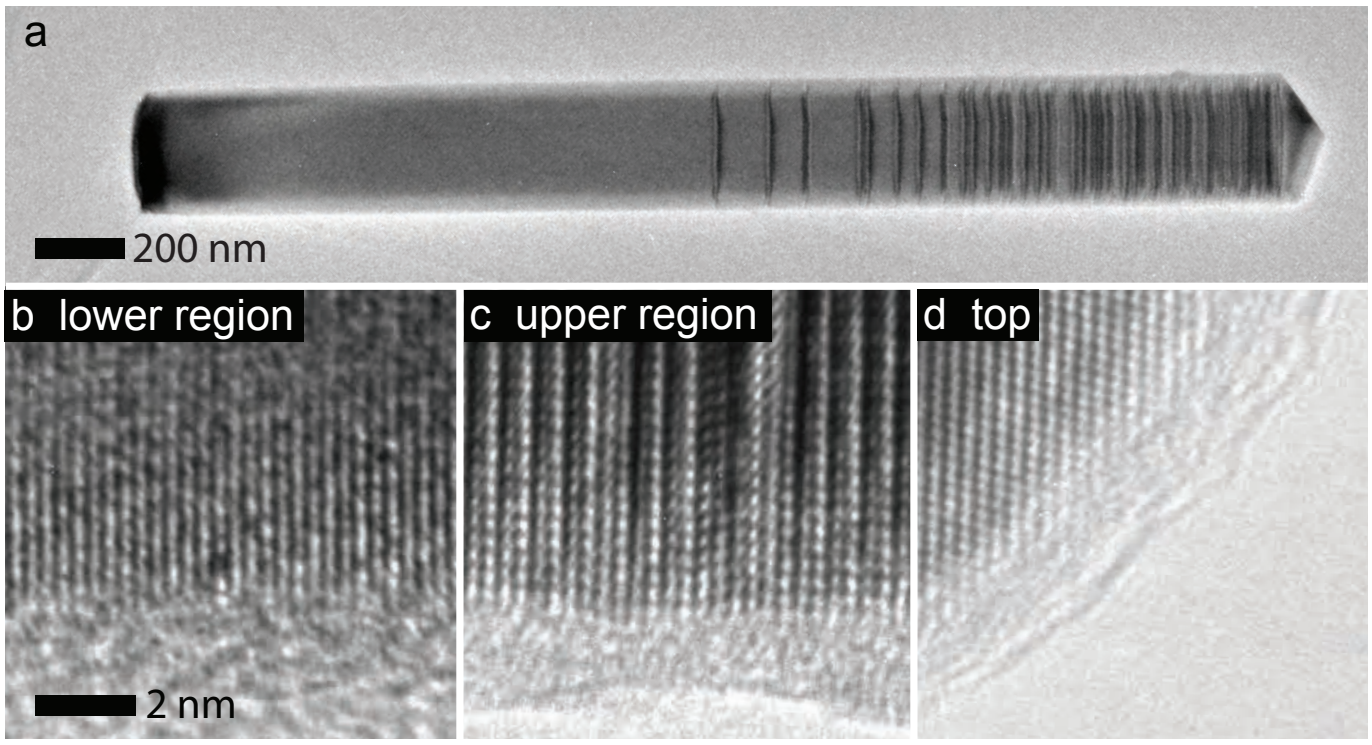

Figure 4.13: TEM of a facetted nanowire, a) an overview over the nanowire. b) the lower region of the nanowire which shows a pure WZ crystal structure. c) the upper region of the nanowire which is riddled with defects. d) the facetted tip consists of a ZB crystal structure. These nanowires were present when growing on (111)B substrates for a longer time. The image is acquired in the $[2\bar{1}\bar{1}0]$ zone axis.

4.3.6 Phase of the particle

Au-seeded GaAs nanowires in MBE are reported to grow in a temperature range where the history of the substrate affects whether or not the seed particles are liquid or solid [100]. Both Pd-seeded MOCVD grown GaAs and InAs nanowires have been suggested to grow from both liquid and solid particles within the same growth [87, 101] showing that determining the phase of the particle is far from straight forward. Our XEDS measurement showed a low (≤ 1 at%) of As and no Ga inside the particle but as shown in our results on the cooling we might have Ga inside the droplet during growth. This means that both the Ag-As and the Ag-Ga phases need to be accounted for when determining the phase of the particle. In the Ag-Ga phase diagram [102] the highest amount of Ga dissolved in solid Ag is 18.7 at%. So if only Ga is present inside the particle and the Ga content is below 18.7 at% the Ag droplet is solid in our temperature range (400-600°C). The lowest Ga composition that results in a pure liquid alloy close to this temperature interval is 27 at% Ga at 611°C. Moving to the Ag-As phase diagram [32] the highest amount of As that can be dissolved inside of Ag is 7.8 at% at 582°C. The Ag-As phase diagram also has an eutectic point at 540°C so if the particle is only alloying with As the growth temperature needs to be at least 540°C to reach any liquid phase at all. This shows that Ag-seeded GaAs nanowire growth might very well happen with both solid particles (in the lower temperatures) and liquid particles (in the upper temperatures).

4.3.7 TEM on time series of Ag-seeded GaAs nanowires on (100) substrates

This section represents a collaboration with Jordi Arbiol and his research group at ICN2 Catalan Institute of Nanoscience and Nanotechnology Advanced Electron Microscopy Group, Barcelona, Spain.

To increase the understanding on how the nanowires nucleate on a (100) substrate cross-section TEM was performed on the time series samples. These are the samples grown for 4 min, 20 min and 60 min, respectively, presented above in Figure 4.7. The samples grown for 4 min and 20 min are cooled without an As_2 overpressure and the sample grown for 60 min is cooled with an As_2 overpressure.

Imaging after 4 min of growth

In Figure 4.14 particles are imaged after 4 minutes of growth. Different particles were found on the substrate including particles that have not nucleated (Figure 4.14 a) and particles that seem to have nucleated (Figure 4.14 b). The nanowire depicted in Figure 4.14 c) is particularly interesting. Figure 4.14 c) shows an overview over a particle while d) is a higher magnification image of the particle-substrate interface. One side of the particle reveals that a {111} plane interface forms between the substrate and the particle. This might be the start of the wave patterns on the substrate visible in Figure 4.4 at the higher temperature. It could also be the nucleation of a non-vertical nanowire. However the particle-substrate interface shows that already after 4 min, when only minimal nanowire growth has occured, new surfaces between the particle and the substrate have been created, forming the possibility for nanowires to nucleate on other surfaces than (100).

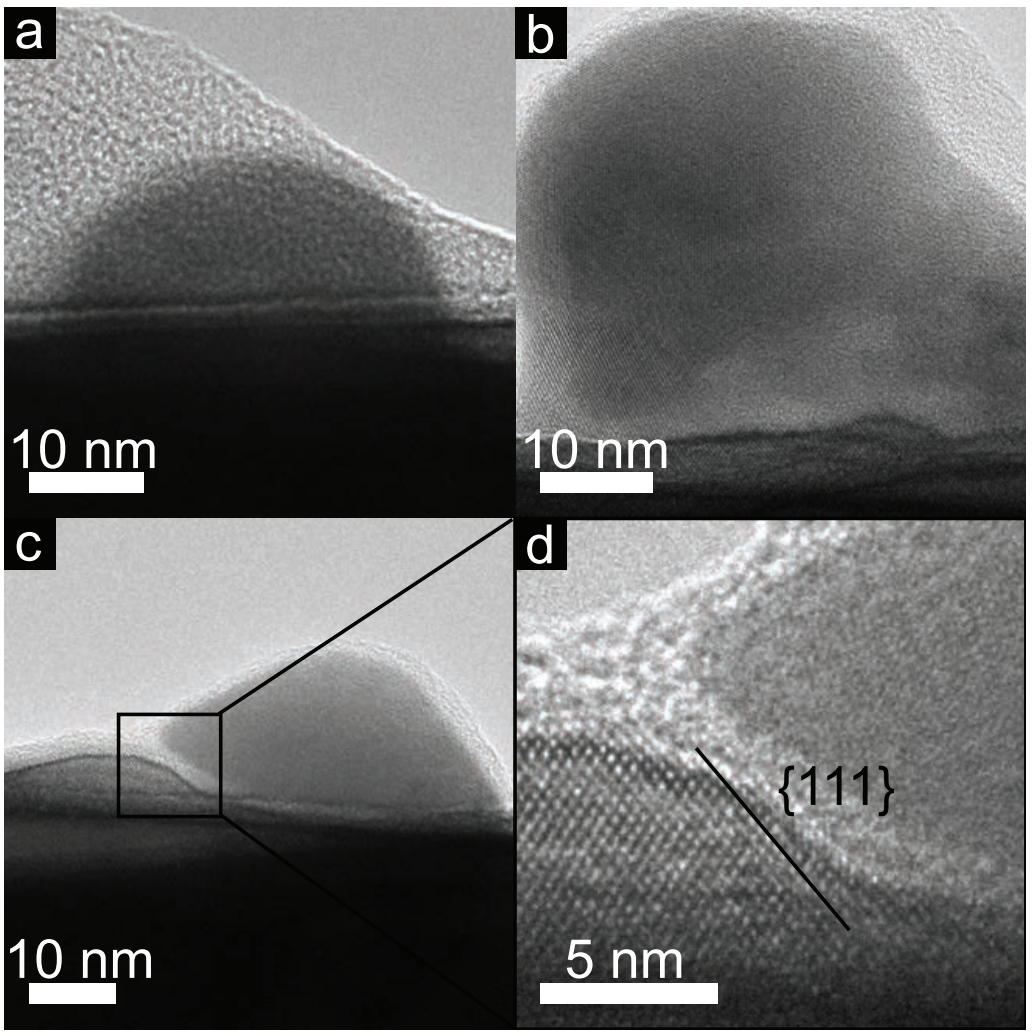

Figure 4.14: The different particles after 4 minutes growth time. The particles show different interface planes between the particle and the substrate. All images are acquired with the zone axis $[0\bar{1}\bar{1}]$.

Imaging after 20 min of growth

The 20 min growth, Figure 4.15, revealead many different particles that have just nucleated. The combination of all particles that have just nucleated and the big increase of nanowire density between the sample grown for 20 min and 60 min shows the extended time it takes for Ag to nucleate GaAs nanowires on a GaAs(100) substrate. TEM of four just nucleated nanowires are depicted in Figure 4.15. The top of the figure shows TEM images and the bottom shows corresponding schematic images. a) and b) show a nanowire that has nucleated on only one side of the particle. c) and d) show a nanowire which has nucleated on both sides of the particle. For this specific particle only the right side is perfectly lattice matched with the substrate (not shown). e) and f) show a nanowire that has started to grow from the substrate in a <111> direction. g) and h) show a nanowire that has nucleated from a triangular hole in the substrate. Even this nanowire has started to grow in a <111> direction. The triangular holes that are the starting points for this particular type of nanowire could be found throughout the sample, sometimes without a Ag particle or nanowire inside. These triangular holes might result from a GaAs-metal interaction [103] with Ag etching the substrate in the same way as Au. Another possibility is that it is one of the pits formed as a defect in layer growth [91]. The SEM image of the sample grown for 60 min shown in Figure 4.7 reveals strongly inclined nanowires which are all originating from holes in the substrate. The nanowire nucleating from the triangular hole is most probably the beginning of one of these nanowires. The preferred interface between the GaAs and the Ag particle is clearly a {111} plane. This since all nucleated particles imaged in HR have at least one major interface in a {111} plane. Even when the particle-substrate interface is parallel to the substrate a zigzag

pattern can form along {111} planes in order to keep the {111} interfaces, Figure 4.16 a).

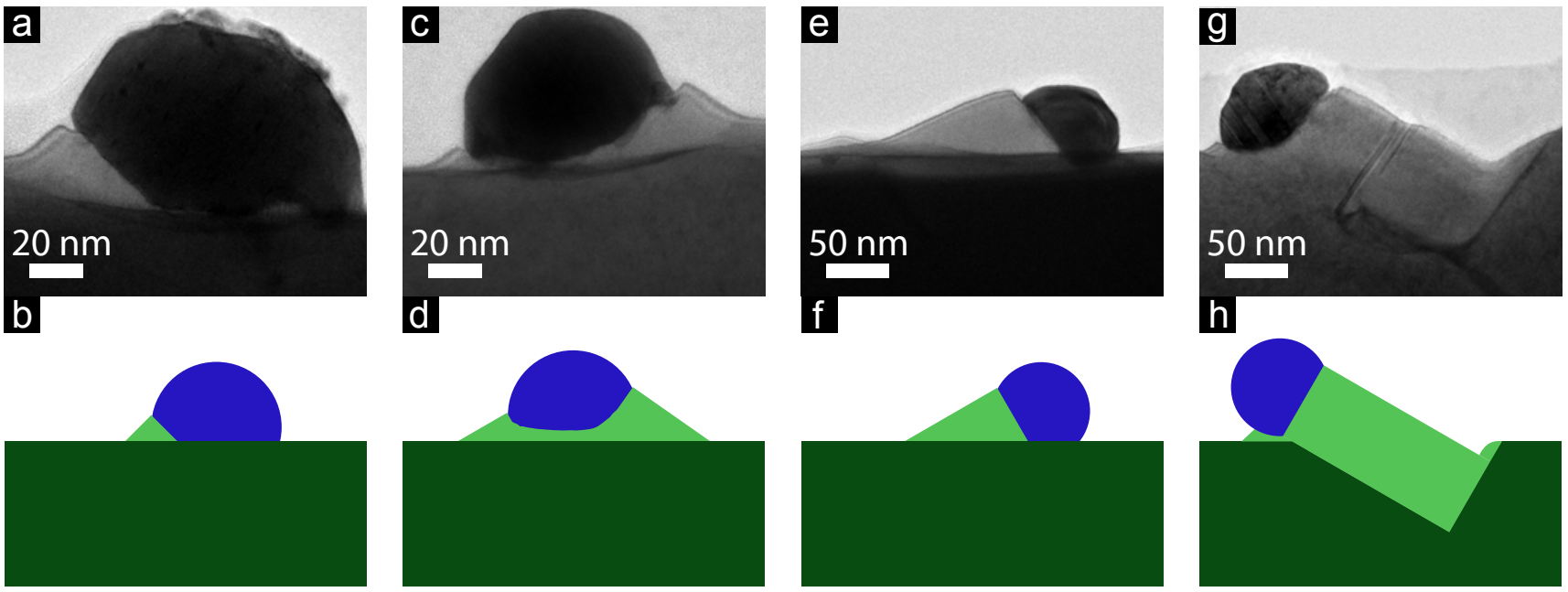

Figure 4.15: The different nanowires which high resolution images were obtained from. Each nanowire shows different nucleations with a schematical image below the TEM image. a) and b) nucleation have only happend on one side of the particle. c) and d) nucleation have occured on both sides of the particle. e) and f) nanowire which have started to grow in the <111> direction g) and h) nanowire which have nucleated from a triangular pit.

EELS results from the nanowires, presented in Figure 4.16 b-e, confirm a Ag particle in the top and GaAs in the nanowire. Following the results from the earlier XEDS results no signal from Ga can be seen inside the Ag particle but small amounts of As are again detected inside the Ag particle.

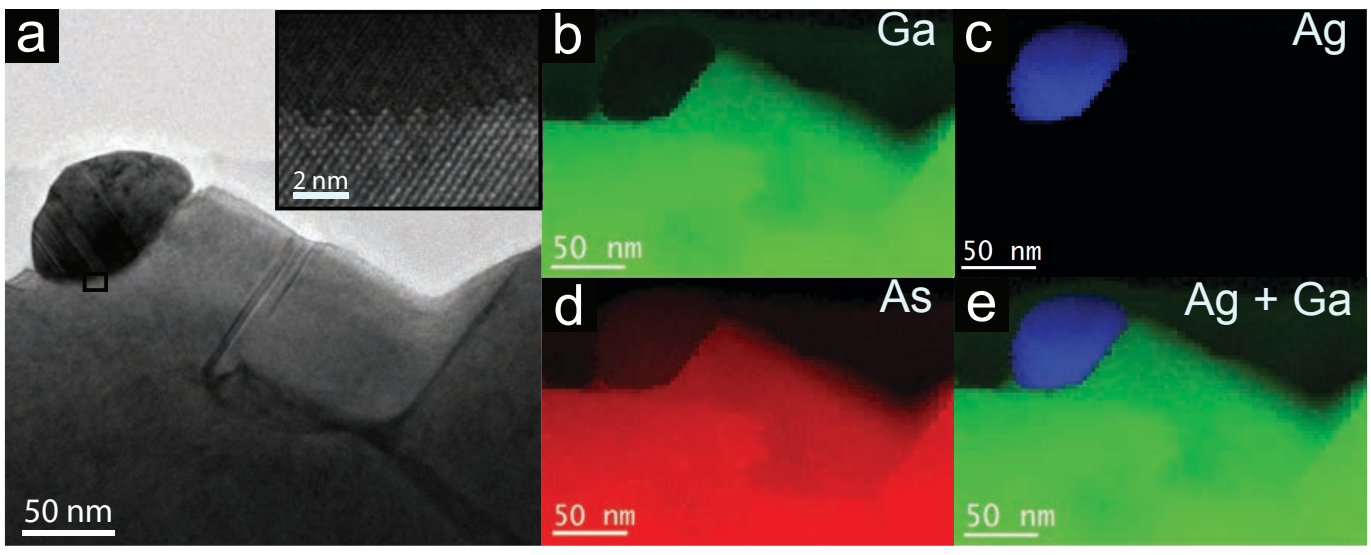

Figure 4.16: a) overview over one nanowire where EELS was acquired. Inset in a) the GaAs/Ag interface with the zigzag patterns forming {111} plane interfaces. For the EELS: green shows the Ga, red the As and blue the Ag. No Ga can be found inside the Ag droplet but a low amount of As is detected. All images are acquired with the zone axis $[0\bar{1}\bar{1}]$.

Many of the Ag particles showed twinning within the particle as illustrated in Figure 4.17. The twinning, however, does not seem to propagate into the nanowire.

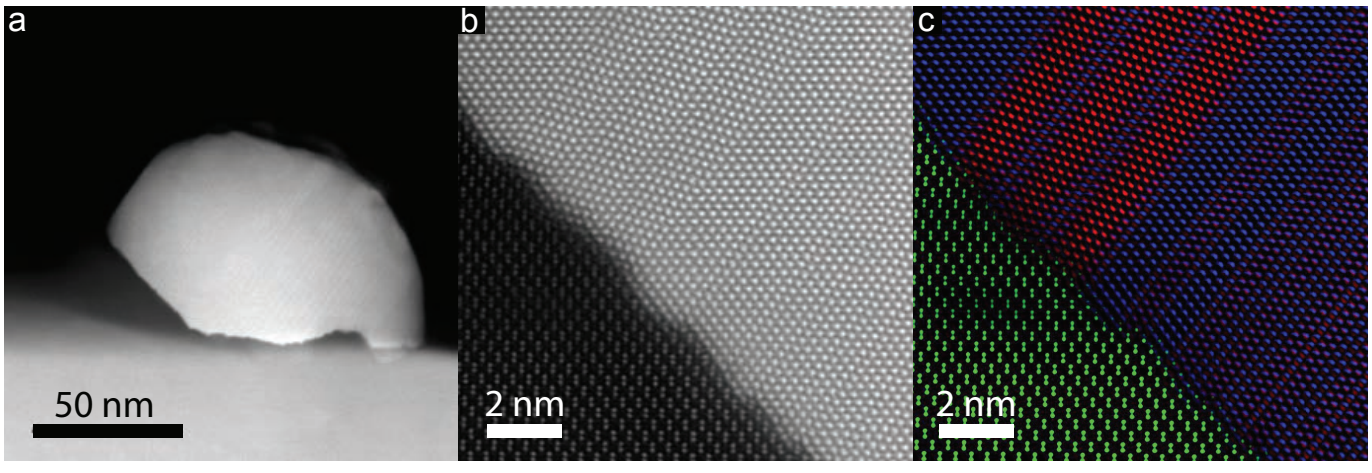

Figure 4.17: HAADF-STEM images of twinning inside the Ag particle. a) overview over a nucleated particle. b) high resolution image over the particle-GaAs interface. c) the twinning inside the particle where blue belongs to one twinning direction and the red to the other twinning direction. All images are acquired with the zone axis $[0\bar{1}\bar{1}]$. The image is acquired at the Advanced Microscopy Laboratory in Zaragoza, Spain and has been deconvoluted with STEM_CELL [104]

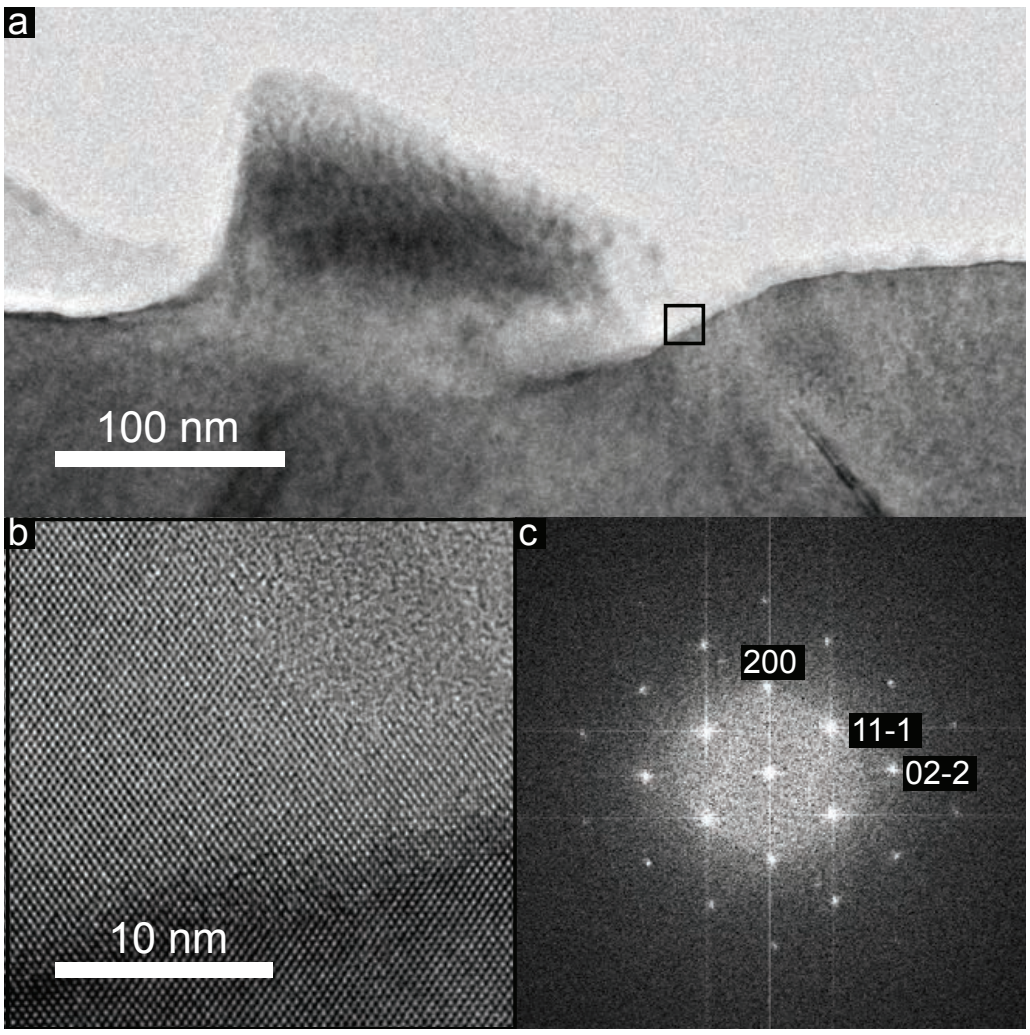

Figure 4.18: A broken vertical nanowire from the sample grown for 60 min. The nanowire has the crystal structure ZB and is fully epitaxial to the substrate. a) Overview over the nanowire. b) A higher magnification of the black square in a) showing the epitaxial match between the nanowire and the substrate as well as the ZB structure. c) FFT of b). The image is acquired in the $[0\bar{1}\bar{1}]$ zone axis.

Imaging after 60 min growth

For 60 minutes growth time one inclined WZ nanowire (not presented) and one broken off vertical nanowire have been imaged in high resolution. The inclined nanowire has been growing in the <0001> direction and has crystallized in the WZ structure with many crystal defects. The broken off vertical nanowire has most probably crystallized in

the ZB structure and both nanowires are originating from a small hole in the substrate. The broken off vertical nanowire is seen in Figure 4.18. a) shows the nanowire stub and the hole in the substrate it is originating from. b) is a high resolution image from the black square in a) showing an epitaxial match between the substrate and the nanowire. c) shows the FFT from b) showing the ZB crystal structure and that the (100) is the same for both the substrate and the nanowire.

4.3.8 Surface growth during GaAs nanowire growth on (100) substrates

From the cross-sectional samples we could also study the surface growth during nanowire growth. The surface growth was separated from the substrate by a white line (ADF-STEM) or black line (TEM). The surface growth also contained a considerable amount of defects such as stacking faults but also other features such as darker areas and spots. Both the defects and the black line separating the layer growth from the substrate can be seen in Figure 4.19 a). TEM image over the waves in the substrate shown in section 4.3.2 is shown in 4.19 b) and shown to be lattice matched to the substrate/layer growth.

As expected due to the long nucleation time and low density of the nanowires we have a considerable amount of surface growth during the nanowire growth. The thickness of the surface growths were measured for each of the three samples and the results comparing the layer growth and the vertical nanowire length can be seen in Figure 4.20. Due to the big difference in nanowire length and density of nanowires in the growths it might be expected that we have more layer growth in the beginning. This does not seem to be the case here. The layer growth for these three samples follows a quite linear dependence with growth time.

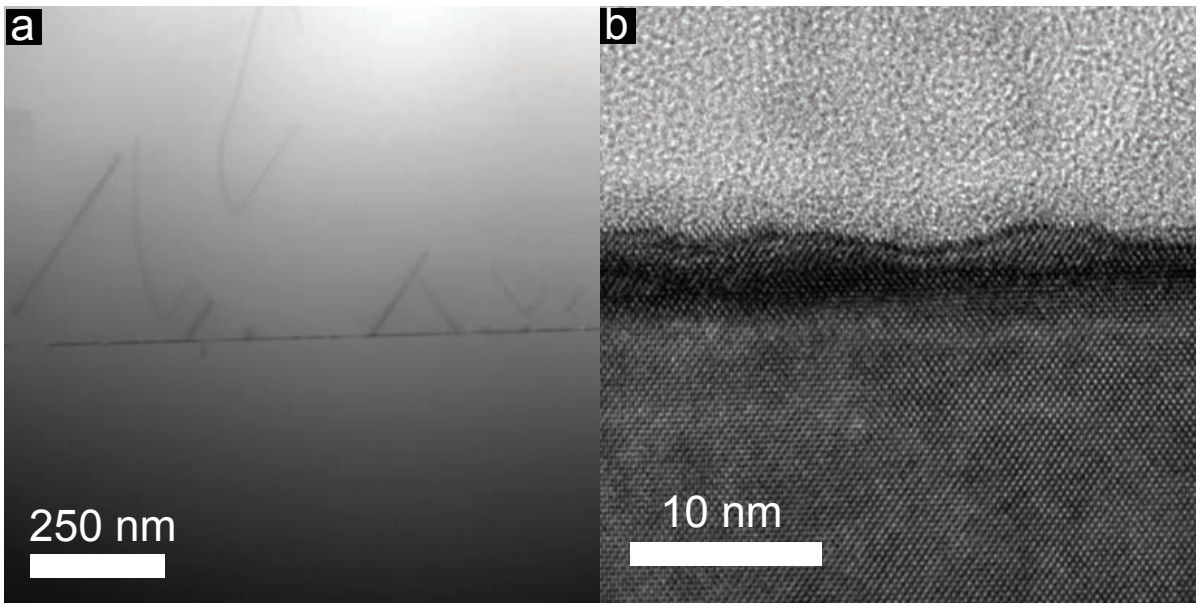

Figure 4.19: Surface growth on the substrates. These images are from the sample grown for 60 min. a) Defects in the layer growth. b) The waves arising from the layer growth on the surface of the substrate. All images are acquired in the $[0\bar{1}\bar{1}]$ zone axis.

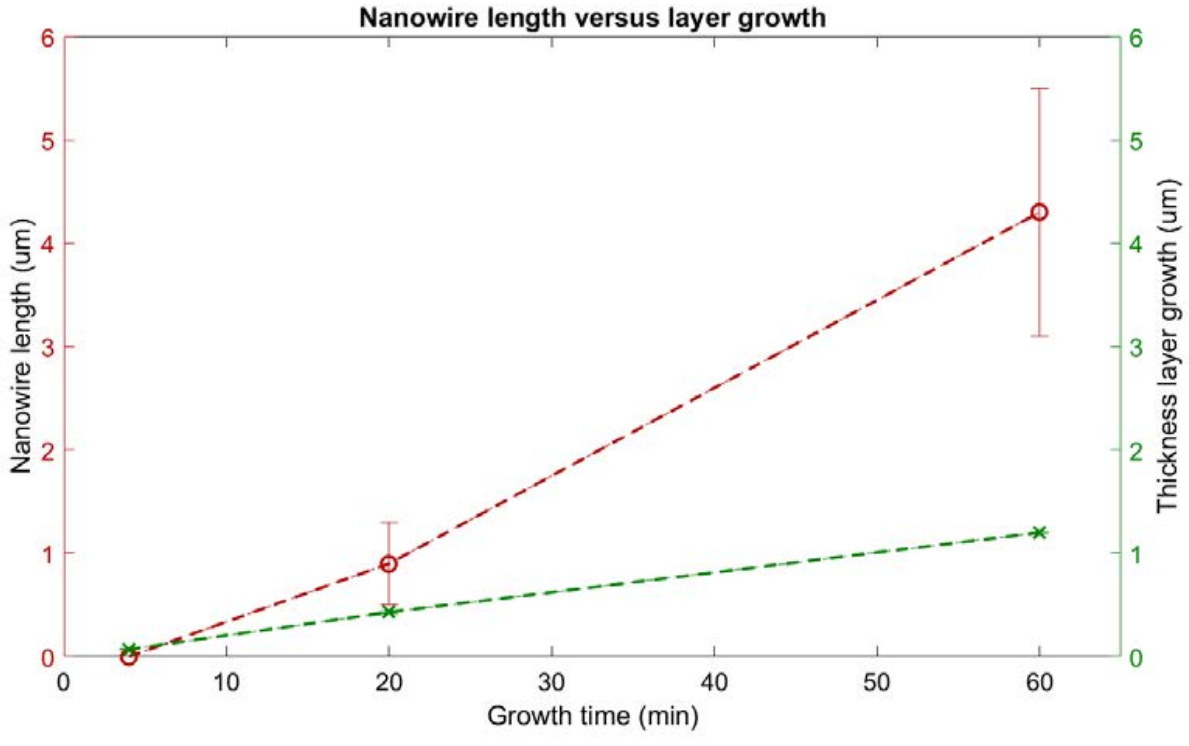

Figure 4.20: Layer growth and length of vertical nanowires versus growth time. Red circles with the scale on the left hand side show the length of the nanowires. Green crosses and the scale on the right hand side show the thickness of the layer growths.

Already after 4 min a considerable amount of layer growth of around 70 nm has grown. This layer growth is thicker than the average particle size on the substrate. Based on the layer growth after 4 min and the increased density of nanowires on the sample grown for 60 minutes the correlation between nanowires and layer growth is not as simple as the particle either nucleating or becoming buried. Instead a number of particles seem to "float" on top of the layer growth and nucleate at a later stage. For that reason we do not relate the delayed growth of nanowires solely to a delayed supersaturation of the Ag particle. We speculate that another plane than the original (100) plane must be present for the particle to nucleate and start to induce nanowire growth. Based on the cross-section TEM results presented we suggest that the evolution of nanowire growth in the [100] direction on GaAs(100) substrates proceeds in a process illustrated in Figure 4.21.

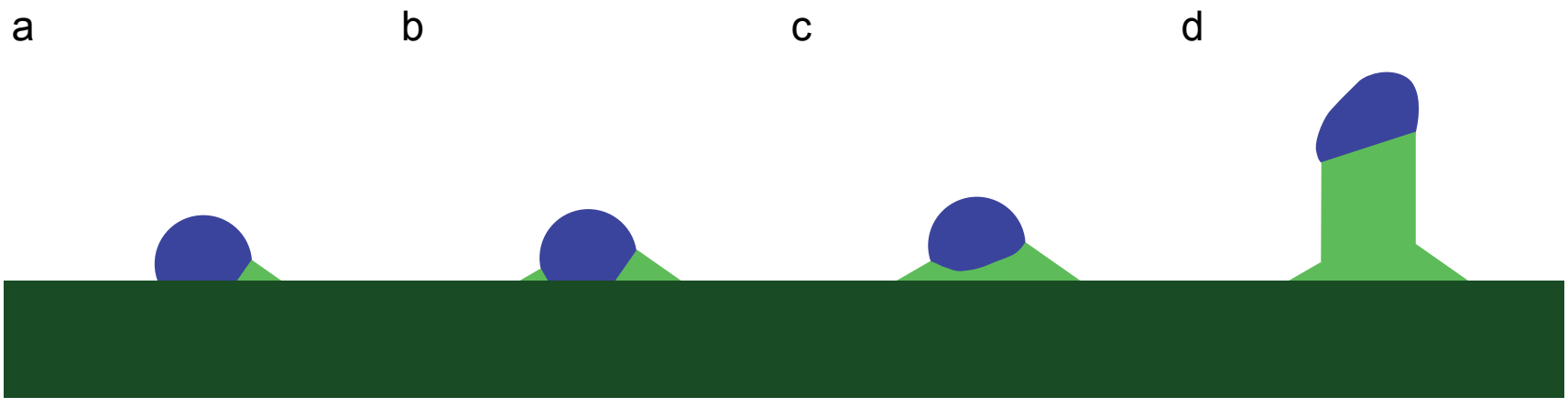

Figure 4.21: A presentation on how the formation of vertical (100) nanowires might take place. In a) the Ag particle has nucleated on one side with the GaAs/Ag interface in the {111} plane. In b) the nanowire has nucleated on both sides forming a {111} interface on each side. In c) the nanowire has started to grow beneath the whole Ag particle. In d) the vertical nanowire has formed.

The nanowire nucleates on one side of the Ag particle creating a {111} plane interface between the Ag and the GaAs. When nucleation occurs on the other side as well the

particle is positioned in a hole within the GaAs with mainly {111} planes as the side interfaces. The hole in the substrate is not necessarily created by the double nucleation but can be a triangular hole or created by the wavelike surface growth. When further growth in the [111] direction is hindered growth will take place beneath the whole Ag particle. Eventually a new Ag/nanowire interface will form, which we earlier suggested to be (115) or (116). The nanowire will then continue to grow in the [100] direction. Hence the long nucleation time for Ag particles on (100) substrates can be both due to the lack of supersaturation of the particles or the lack of {111} surfaces to nucleate on.

In general GaAs nanowires seem to have a difficult time nucleating in other directions than the polar direction <111> B. Studies of GaAs nanowire nucleation on Si(111) report a similar growth progress to the one we have suggested. When Au-seeded GaAs nanowires are grown on clean Si(111) substrates they first grow as traces on the substrate. When the Au particle meets another trace the nanowire changes direction to vertical [105, 106]. So both for Au-seeded GaAs nanowires on Si and for Ag-seeded GaAs nanowires on GaAs(100) other growth directions must be hindered before vertical nanowire growth takes place on clean standard non-polar substrates. A similar investigation of Au-seeded GaAs nanowires on GaAs(100) substrates also showed that the preferred metal/GaAs interface followed the {111} plane regardless of whether the growth direction was <111> or <110> [103]. Though, which we have shown, one of the advantages with using Ag as seed particle on (100) subtrates is the high yield of vertical nanowires without any substrate preparation. It might be possible to increase the yield even further by intentionally blocking other growth directions such as <111>, <110> and <112> by for example using a SiO_2 masking layer.

4.4 Conclusions

We have presented a thorough investigation of Ag-seeded GaAs nanowires on both GaAs(111)B substrates and GaAs(100) substrates. For (111)B substrates the nanowires grow robustly in the temperature region 400°C to 600°C. At the higher growth temperatures a vertical yield of 100% is obtained and the nanowires exhibit a pure WZ crystal structure. Keeping the high Ga flux and lowering the As_2 pressure to $2.4*10^{-6}$ Torr the growth changes from a transport limited regime to a more nucleation limited regime. For growth on (100) substrates we reached a maximum yield of 45-50% vertical nanowires at the temperature ≈575°C. These vertical nanowires exhibit a pure ZB crystal structure. The nucleation on (100) substrates at higher temperatures is very sensitive to the Ga flux and takes a long time. For many growths on (100) substrates particles were still visible on the substrate after 30 min of growth. The preferred Ag/GaAs interface is the {111} plane and we suggest that the <111> growth direction must be hindered for the nanowire to grow in the vertical <100> growth direction. From our experiments we also conclude that our Ag-seeded GaAs nanowires are of the same quality with regards to yield and crystal structure as nanowires grown with Au, SC or SAE on (111)B substrates. For (100) substrates we show a higher yield of vertical Ag-seeded GaAs nanowires than we know have been published for MBE grown Au-seeded, SC and SAE nanowires.

Chapter 5

Growth and characterization of Ag-seeded InAs nanowires

5.1 Introduction

Growth of Ag-seeded InAs nanowires from InAs substrates in MBE has to the best of our knowledge never been reported. However Ag-seeded InAs nanowires have been shown to grow on substrates such as graphite flakes [36] and Si(111) [35]. In this chapter we investigate the possibility to grow Ag-seeded InAs nanowires on InAs(111)B substrates with MBE.

In the same way as GaAs nanowires, Au-seeding, SC and SAE are the most common ways to grow epitaxial InAs nanowires [34]. Due to the long history of research with Au as seed particle nanowires with many different properties have been grown. In the same way as GaAs many studies have been performed on InAs nanowires to find a pure WZ or ZB crystal structure, and the correlation between growth parameters and crystal structure has been thouroghly investigated, see for example [75, 107, 108]. For InAs controlled twinning resulting in zig-zag edges has also been shown [109, 110] as well as various other nanowire morphologies besides the simple unidirectional nanowire, such as nanotrees [111], merged nanowires [112] and controlled kinks [113].

A few examples of other seed particles than the Au and Ag-seeded InAs nanowires presented above have been reported. These reports include Mn-seeded InAs nanowires on Si(100) substrates [114]. Introducing tricarbonyl(methylcyclopentadienyl)manganese after inital growth of nanowires resulted in self assembly of Mn particles and the possibility to grow branched nanostructures without Au as seed particle [115]. For Pd both MBE grown InAs nanowires on GaAs(111)B substrates [22] and CBE grown InAs nanowires on InAs(111)A substrates [116] have been reported. Ag has also been used to seed a network of non-tapered $In_xGa_{1-x}As$ nanowires on Si(100) substrates with MOCVD [117]. All of the above indicate that Ag is a promising candidate not only for GaAs but also for InAs nanowire growth.

In this study we start by investigating particle formation on InAs substrates through the thin film annealing method [62]. After confirmation of particle formation a wide range of growth parameters are tested by varying the temperature, In flux and As_2 pressure to map the growth window of Ag-seeded InAs nanowires. The growths discussed in this chapter are presented in table 5.1 while a full list of all Ag-seeded InAs nanowire samples

is found in Appendix B.

5.2 Preparation of Ag particles and annealing

The first step to grow InAs nanowires from Ag particles is the creation of Ag particles on the InAs surface. We have formed our nanoparticles with the thin film annealing method [62] explained in chapter 2.4. Searching the literature we have not found any earlier reports of the behaviour and formation of Ag particles from a thin Ag film on InAs at the elevated temperatures usually needed for nanowire growth. We therefore started our experiments of Ag-seeded InAs nanowires with annealing experiments.

Although we have not found anything about the formation of Ag particles on InAs substrates at the elevated temperatures used in nanowire growth, the properties and the development of a few monolayers thin Ag film on InAs(110) during deposition has been investigated in the temperature range 4K to room temperature [118, 119, 120]. The reason for this is that a Ag film in the thickness range of monolayers on InAs(110) substrates creates band bending and a two-dimensional electron gas [118, 119, 120]. If the deposition is performed at 85K [120] or room temperature [118, 119] particles will form already during deposition due to Wolmer-Weber growth.

Formation of Ag particles from a thin film at higher temperatures has been researched on other substrates than InAs due to the optical properties of Ag nanoparticles. For example the thin film annealing method has been used to form Ag particles on TiN [121], Si [122, 123] and ZnO [124, 125] substrates. These reports show similar results to Au (see chapter 2.4 for a literature overview) with a higher annealing time resulting in bigger particles [122, 125] and a lower density [125]. A thinner film results in a decrease of the particle size [121, 124]. Annealing of a thin film was also the choice of particle preparation when Pan et al. [35] were growing Ag-seeded InAs nanowires on Si(111). They report a decrease in particle size (and hence nanowire diameter) by introducing a two step annealing process. They first anneal at the low temperature 200°C for ten hours and then at 600°C for 20 min. Surprisingly the two step process with a longer total annealing time generated smaller particles compared to other reports [63, 122, 125].

As mentioned in chapter 2.1 all samples must be degassed before they are introduced to the growth chamber inside the MBE. The substrate is then annealed at 550°C or higher in order to remove the native oxide on the InAs wafer. In this study we focused on the differences of particle size and density of a 10 nm thin Ag film after the degassing step and annealing at 550°C for 0 min, 5 min and 15 min. For a complete list of the annealing samples see Appendix C. For all samples except the degassing sample an overpressure of As_2 was kept. Figure 5.1 a) shows an SEM image of a Ag-coated InAs(100) wafer after the degassing step at 250°C for 1 hour. We see that already after the degassing step the film has broken up and Ag particles with the average size of $8 * 10^{-4}$ μm^2 have formed. This corresponds to an average particle diameter of 31 nm. The particle size distribution for the degassed sample is depicted in Figure 5.2 a).

SEM images of InAs(111) substrates with a 10 nm thin Ag film annealed at 550°C are seen in Figure 5.1 b)-d). For the sample in b) the temperature has been increased to 550°C and then directly decreased. Figure 5.1 c)-d) show annealing at 550°C for 5 min and 15 min, respectively. Already from the SEM images it can be seen that the density of particles decreases with a longer annealing time. In all samples annealed at

550°C pits in the substrate indicate that Ag has formed an alloy with the substrate during the annealing step. Especially for the sample annealed for 15 min the Ag particles look like they have migrated on the substrate creating pits while moving. Figure 5.2 shows histograms over the particle size distributions for each of the four samples. In the histograms the increased particle size distribution with increased annealing time is clearly seen. The mean particle size and number of particles per unit area are presented in Figure 5.3. When increasing the annealing time from 0 min to 15 min the average particle area increases from 0.05 μm^2 to 0.12 μm^2, which corresponds to a particle diameter of 250 nm and 380 nm respectively. The particle density decreases from 0.9 particles/μm^2 to 0.3 particles/μm^2.

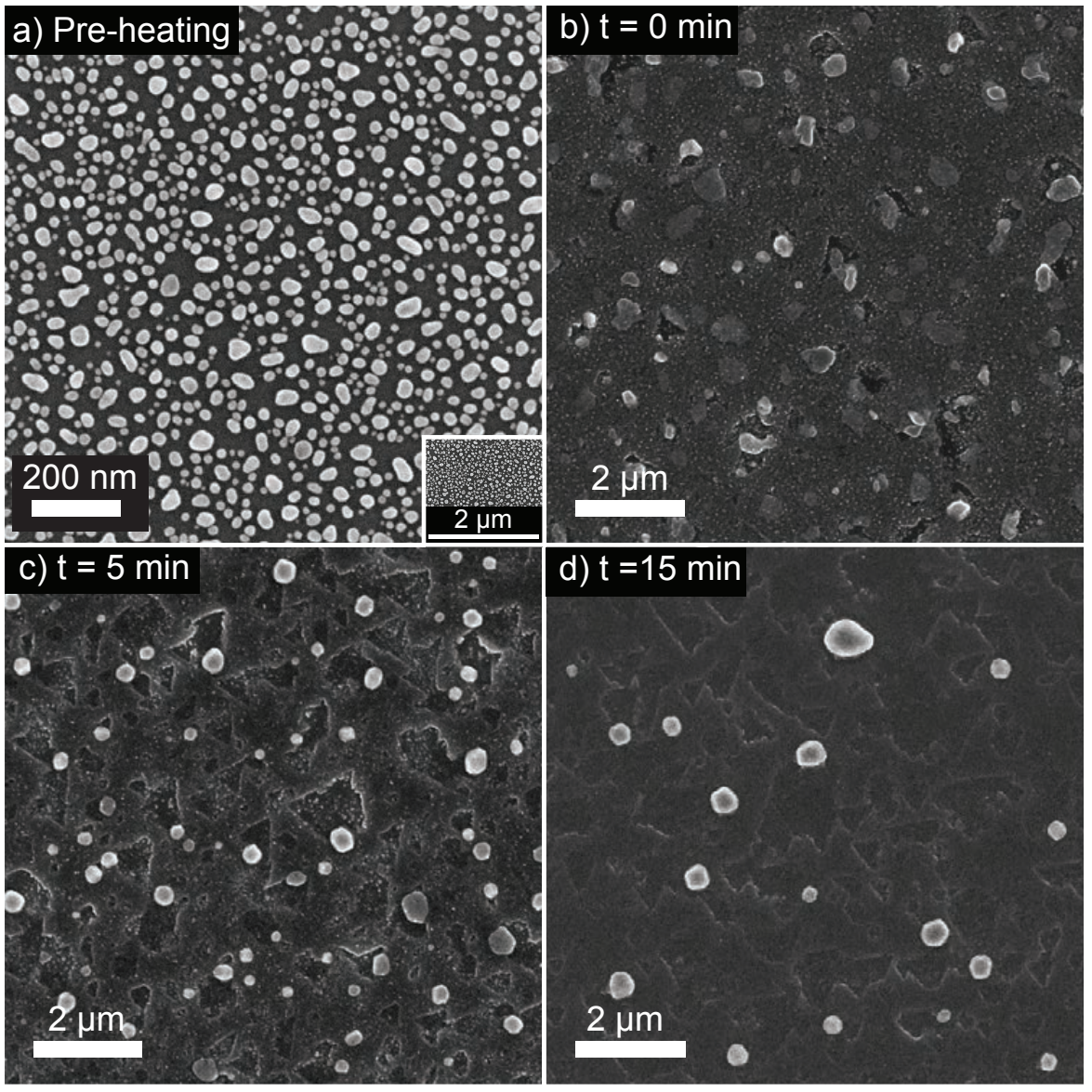

Figure 5.1: Top view SEM images from the annealing experiments. a) An InAs(100) substrate after 250°C heating for 60 min (the so called degassing step). The inset has the same magnification as the other three SEM images. b)-d) (111)B substrates annealed at 550°C for 0 min, 5 min and 15 min respectively. Images acquired by Anders Bjørlig.

As mentioned in chapter 2.4 a longer annealing time commonly results in bigger particles. This can be attributed to two significantly different processes: *Ostwald ripening* and *coalescence* [126]. In coalescence the existing particles will migrate, encounter each other and coalesce. In Ostwald ripening the higher surface pressure for smaller particles will cause atoms or clusters of atoms to diffuse to bigger particles. Hence bigger particles will grow at the expense of smaller particles [47]. It has been suggested that the particle size distribution can give an insight into the mechanism involved with a tail of bigger particles (as in our experiments)

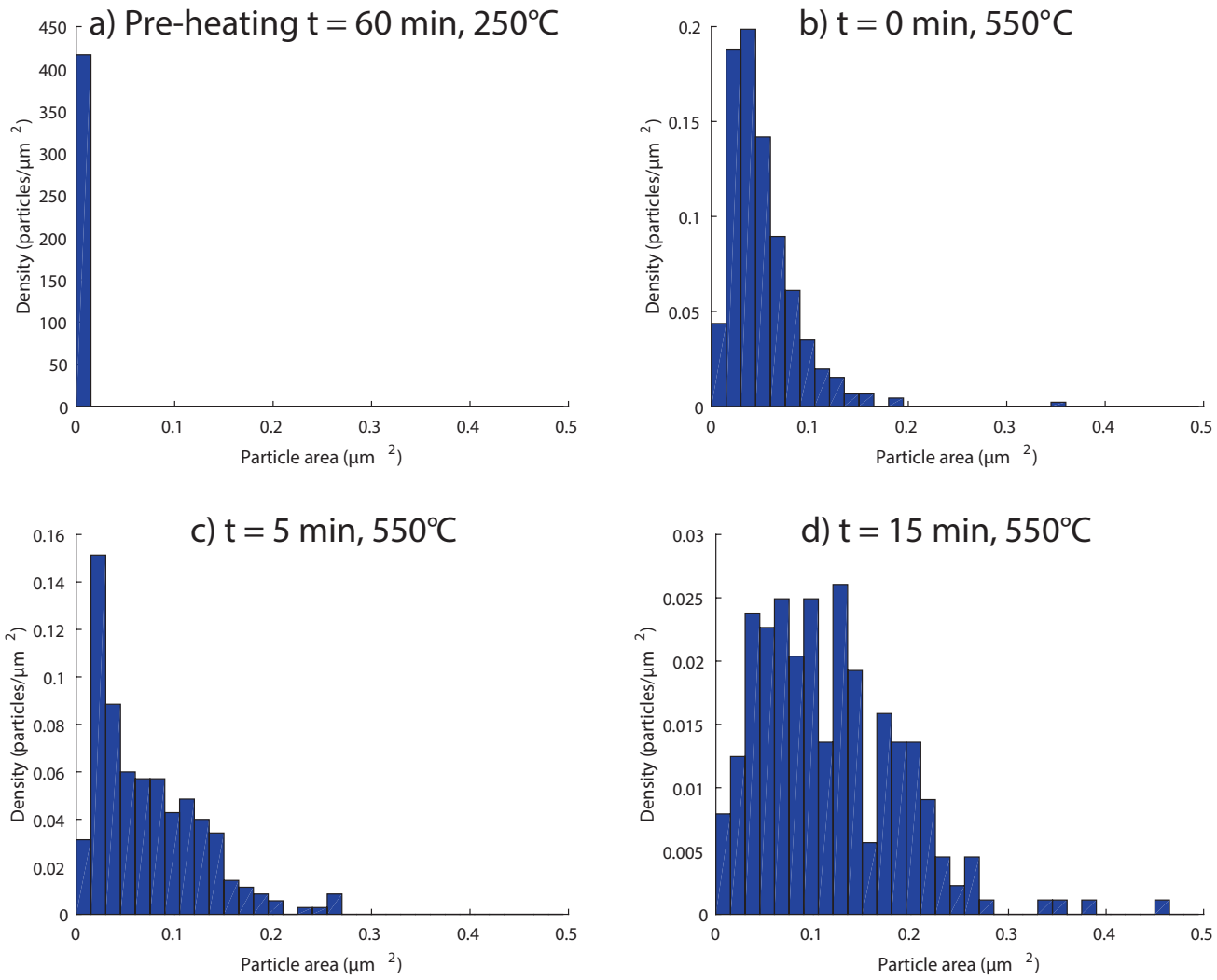

Figure 5.2: Particle size distribution for the four annealing samples. a) the degassed InAs(100) sample. b)-d) the InAs(111)B substrates annealed at 550°C for 0 min, 5 min and 15 min respectively. A longer annealing time results in bigger particles with a wider particle size distribution. Note the difference in scales on the y-axis.

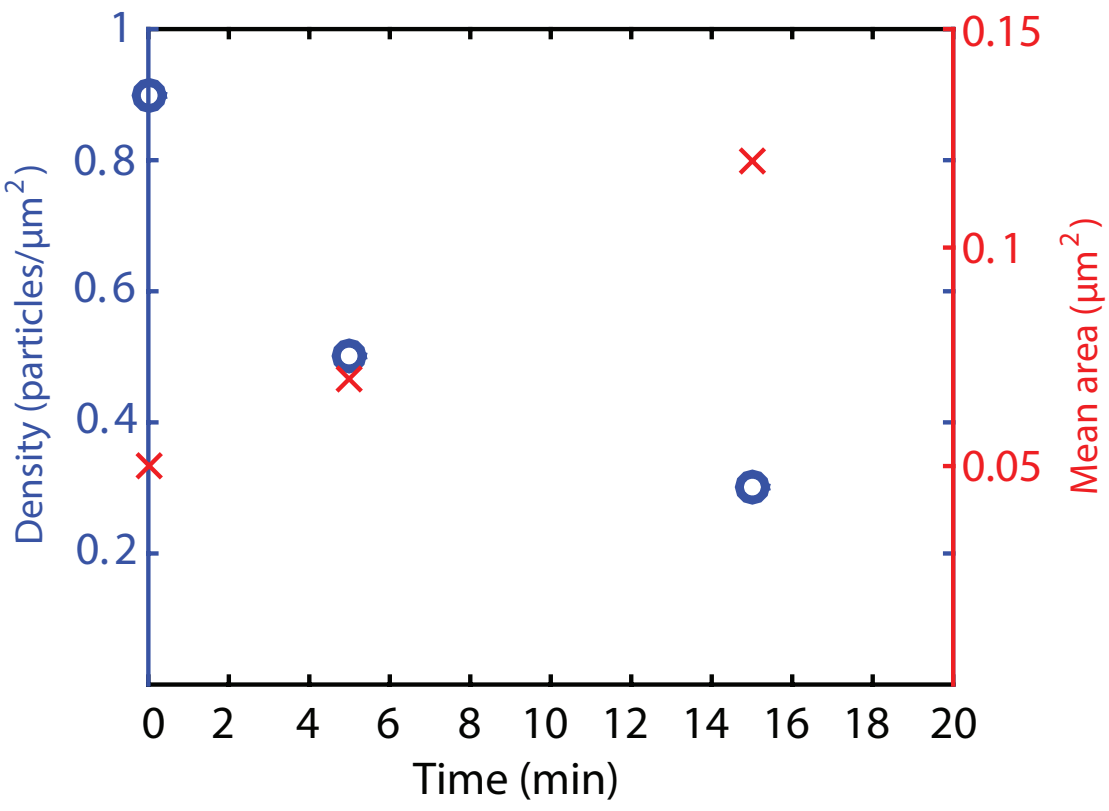

Figure 5.3: Mean particle density (left axis) in particles per μm^2 and mean particle area (right axis) in μm^2 as a function of the annealing time for Ag on InAs(111)B substrates.

indicating the coalescence mechanism [126]. The pits connected to each particle for the longer annealing times in our experiments clearly show that particle migration takes place. This further supports the theory that the particles grow mainly due to particle migration and coalescence. However as Plante et al. [63] point out, the theory does not account for alloying between the particle and substrate. Further they also highlight that determining the mechanism solely based on the size distribution is misleading [127]. Most likely the increase in particle size is due to a combination of the two mechanisms.

Based on the results from the annealing temperature and the earlier report where small Ag particles increase the yield of vertical Ag-seeded InAs nanowires [35] a short annealing time of two minutes was used in subsequent growth experiments. The thickness of the Ag film was also decreased to 1-2 nm in order to keep the seed particles small.

To confirm that the deoxidation temperature is not affected by a thin Ag film a monitored deoxidation test with an InAs(111)B substrate with a two nm Ag film was also performed. During the slow temperature increase ($t_{increase} \approx 60$ min) the substrate was constantly recorded with RHEED and oxide removal was confirmed at the expected 550°C. The RHEED pattern after deoxidation can be seen in Figure 5.4 a). The surface is illuminated in the <112> direction and shows an unreconstructed (111)B surface. This is consistent with an earlier report [128] where Andersson et al. report an unreconstructed surface for InAs(111)B when first sputtered clean and then annealed at 400°C. However in our system we do not see the surface reconstruction for a GaAs(100) substrate until after some film growth has taken place. This indicates that even though no second order lines are visible in the RHEED pattern for the InAs(111)B surface we cannot rule out the existance of surface reconstructions during nanowire growth. SEM images on the deoxidation sample confirm that Ag particles remain on the substrate after deoxidation, see Figure 5.4 b). Similar to the sample annealed at 550°C for 15 min the particles have migrated on the substrate. In Figure 5.4 b) some of the more obvious paths created by the migrating Ag particles have been marked with arrows.

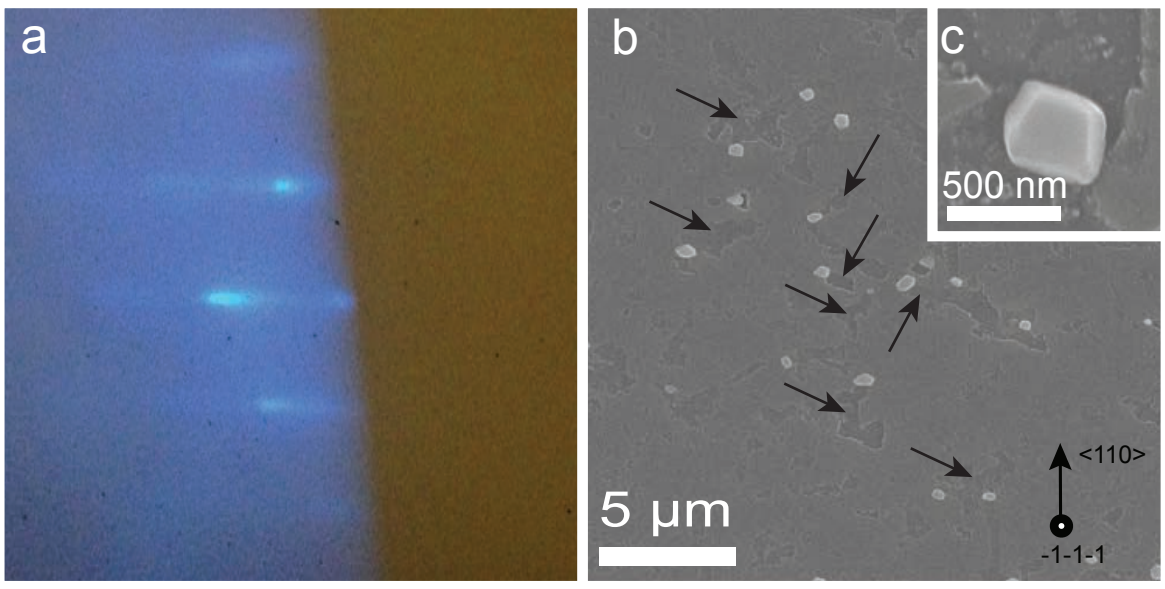

Figure 5.4: a) RHEED pattern after oxide removal from an InAs(111) substrate with a 2 nm thick Ag film. The RHEED pattern shows no surface reconstruction. b) SEM image of the same sample. The Ag particles are present all over the substrate. The inset shows a higher magnification of one of the facetted particles.

5.3 Growth experiments

5.3.1 Method for Ag-seeded InAs nanowire growth experiments

In order to find and map the growth window for Ag-seeded InAs nanowires a wide range of different growth parameters have been tested. In this study growth temperature, In flux, As_2 pressure and the Ag film thickness have been varied. The growths mainly discussed in this chapter are presented in Table 5.1, while a full list over the Ag-seeded InAs nanowire growths is given in Appendix B. The samples listed in Table 5.1 form four different sets of tests of the growth parameters: sample A and B test the In flux, sample B and C test the As_2 pressure and samples D-G form a temperature series. Sample X is an additional EBL patterned growth at the high temperature 500°C. Sample H and I form a second temperature test with different In flux and As_2 pressure as well as Ag film thickness. All growths are performed on InAs(111)B substrates and sample C, E, G and X have been glued to a GaAs(100) carrier wafer before loaded into the MBE.

All samples have first been degassed for 1 hour at 250°C and then transferred into the MBE growth chamber where they have been annealed in an As_2 overpressure. After annealing the temperature has been lowered to the growth temperature and allowed to stabilise for 10 minutes before the growths have been started by opening to the In effusion cell. All temperatures have been measured with a pyrometer or set with the calibration presented in Appendix E.

Table 5.1: Ag-seeded InAs nanowire growths on InAs(111)B

Sample	Ag thickness (nm)	Substrate T (C)	In flux (atoms/m^2s)	As_2 pressure (Torr)	V/III ratio	Eq 2D growth (μm/h)	Growth time (min)
A	2	420	$1.7 * 10^{18}$	$7.0 * 10^{-6}$	35	0.3	30
B	2	420	$3.3 * 10^{18}$	$7.0 * 10^{-6}$	18	0.6	30
C	2	420	$3.3 * 10^{18}$	$1.5 * 10^{-5}$	39	0.6	60
D	2	370	$4.3 * 10^{18}$	$1.5 * 10^{-5}$	30	0.7	30
E	2	420	$4.3 * 10^{18}$	$1.5 * 10^{-5}$	30	0.7	30
F	1	445	$4.3 * 10^{18}$	$1.5 * 10^{-5}$	30	0.7	30
G	2	470	$4.3 * 10^{18}$	$1.5 * 10^{-5}$	30	0.7	30
X	10nm EBL	500	$3.3 * 10^{18}$	$1.5 * 10^{-5}$	39	0.6	30
H	0.5	370	$5.1 * 10^{18}$	$5.0 * 10^{-6}$	8	0.9	30
I	0.5	420	$5.1 * 10^{18}$	$5.0 * 10^{-6}$	8	0.9	30

5.3.2 Results for Ag-seeded InAs nanowire growth

A range of different nanowires have been grown and for simplicity a terminology similar to what Hallberg et al. used [87] will be followed when addressing different kinds of nanowires. *Curly nanowires* are nanowires with so many changes of growth directions that they are not straight, see Figure 5.5 c). *Inclined nanowires* are nanowires that are straight but not vertical with respect to the substrate, see Figures 5.5 d)-e). *Vertical nanowires* are nanowires that grow straight and vertical with regards to the substrate, see Figure 5.5 f). When *straight nanowires* are addressed both the inclined and the vertical nanowires are included. During SEM analysis all samples have been characterized on at least three different sites and the SEM images presented herein are representative for the

samples. However during our experiments we discovered the importance of complete oxide removal from the substrate. All the glued samples where nanowire growth was present showed nanowire growth on only parts of the substrate. We attribute this to insufficient removal of the oxide with the oxide removal being more complete at the areas where nanowires have grown. Since the pyrometer reading can be both on the InAs substrate or the carrier wafer the uncertainty of the temperature is bigger for the glued samples causing insufficient oxide removal and nanowire growth only on parts of the wafer. In these cases only the areas with nanowire growth have been considered. This is further elaborated in Appendix D

Figure 5.5 a) shows an SEM image of sample A and 5.5 b) shows an SEM image of sample B. Both sample A and sample B are grown at the temperature 420°C with two different In fluxes. Sample A has an In flux of $1.7 * 10^{18}$ atoms/m^{2}s while sample B has an In flux of $3.3 * 10^{18}$ atoms/m^{2}s. A majority of all nanowires on both samples are curly nanowires, a few straight nanowires are however scattered across the samples. Figures 5.5 c)-f) show some of the different nanowires on sample B and in Figure 5.5 b) the straight nanowires on sample B are marked with white arrows. A more systematic investigation of the density of straight nanowires shows a slight increase of straight nanowires from 2.0 ± 1.5 nanowires/1000 μm^2 to 4.6 ± 1.8 nanowires/1000 μm^2 when increasing the In flux. This increased average of straight nanowires suggests that the nucleation of straight nanowires is favored at the high In flux.

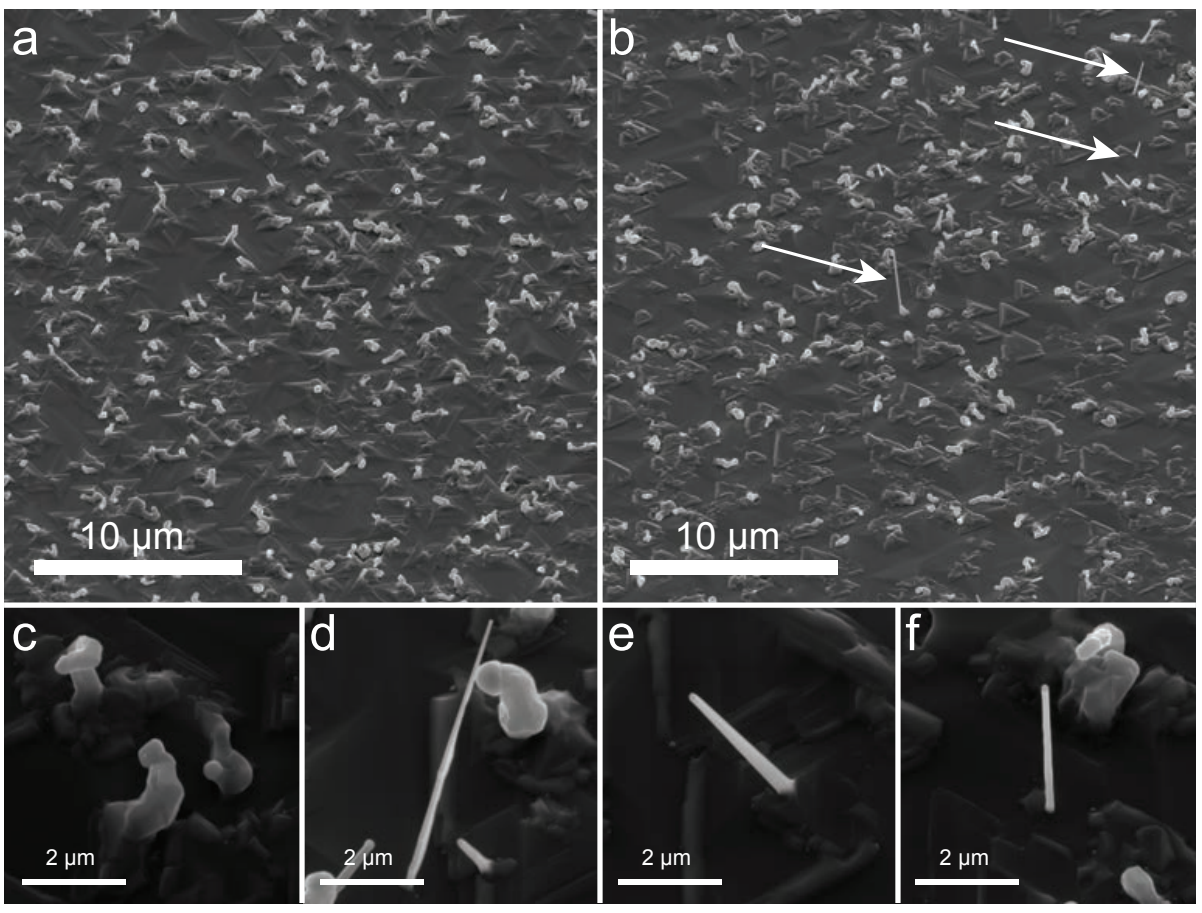

Figure 5.5: The difference between sample A (image a)) and sample B (image b)). Both images are acquired at 45° tilt and both samples show mostly curly nanowires. The straight nanowires on sample B are marked with white arrows in b). Images c)-f) show a few of the different nanowires found on sample B: c) curly nanowires, d) and e) inclined nanowires and f) a vertical nanowire. Images c)-f) are acquired at 20° tilt.

For sample C the high In flux of sample B was kept and the As_2 pressure was increased by a factor of $\sim$2 compared to samples A and B, discussed above. This resulted in a considerably higher amount of straight nanowires compared to sample B, see Figure

5.6. The number of straight nanowires increased from 4.6 ± 1.8 nanowires/1000 μm^2 on sample B to 10 ± 0.7 nanowires/1000 μm^2 on sample C. Sample C is grown for a longer time which explains the obviously longer nanowires in Figure 5.6 b) compared to a). However since all particles in sample B have nucleated in either straight or curly nanowires we do not believe that the longer growth time affects the statistics in the same way as the time affects the statistics for nanowire growth on GaAs(100) presented in chapter 4. While sample B has a smooth surface with islands sample C has a more rough surface. We attribute this to a decrease of the diffusion length for the group III species with a higher As pressure. A decrease of the group III diffusion length on the surface with an increased As pressure is consistent with an earlier report [90].

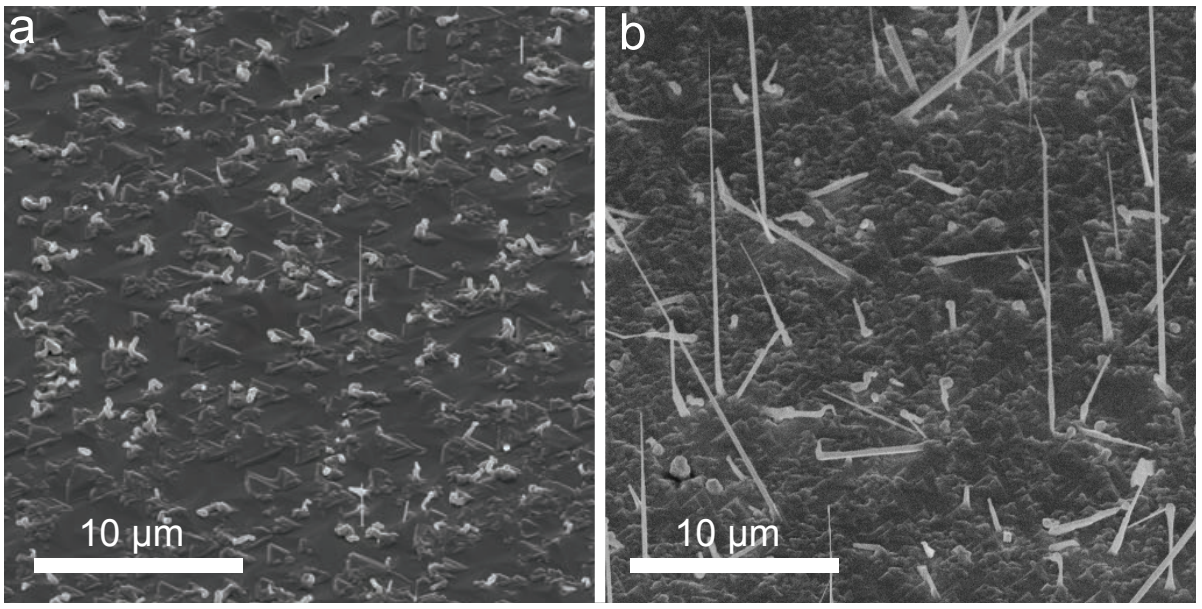

Figure 5.6: Comparison between sample B (image a)), and sample C (image b)). Both samples are imaged at 45° tilt. In sample C the density of straight nanowires has increased.

Based on the results in Figure 5.5 and 5.6 a high In flux and a high As_2 pressure appears to promote straight nanowire growth. Therefore a temperature series was conducted with the high In flux $4.3 * 10^{18}$ atoms/m^2s and the high As pressure $1.5 * 10^{-5}$ Torr. For MBE grown Au-seeded InAs nanowires on InAs(111)B substrates a growth temperature in at least a temperature range of 390-450°C [129, 130, 131] have been reported. For Ag-seeded InAs nanowires grown on graphite and Si temperatures of 417°C [36] and 380-560°C [35], respectively, have been reported. In order to cover a wide temperature range the temperatures were set to 370°C (sample D), 420°C (sample E), 445°C (sample F) and 470°C (sample G). The results from this temperature series are shown in Figure 5.7. Nanowire growth occured at the temperatures 370°C and 420°C. At 445°C a sparse amount of nanowires had grown and at 470°C the nanowire growth had ceased completely, see Figure 5.7. The morphology of vertical nanowires changed with the increased temperature. At 370°C all vertical nanowires imaged have an obvious tapering with a small particle in the top. Increasing the temperature to 420 or 445°C the tapering of the vertical nanowires mostly disappears. We attribute this to the longer diffusion length of In due to the increased temperature. At the low temperature 370°C all vertical nanowires viewed from the top exhibit clear facetting. Based on the substrate orientation these facets are always {112} type in the base of the nanowire, see Figure 5.7 a). Along the length of the nanowire the facets can switch. For some of the nanowires three of the facets are more pronounced giving the nanowire a more triangular shape (not shown). At the higher temperature 445°C the switching of the facets within one nanowire is gone.

The facets of the nanowires grown at the higher temperature 445°C were not always distinguishable but both {112} type and {110} type seem to exist.

For the substrate morphology there is a drastic change between the lower temperatures and the higher temperatures. Both sample D at 370°C and sample E at 420°C exhibit a rough surface after growth. When increasing the temperature to 445°C (sample F) the substrate instead has a smooth surface with triangular islands with the sides parallel to the {112} planes. When increasing the temperature even further to 470°C (sample G) the surface is smooth with pits, see Figures 5.7 d) and h). We attribute this smoother surface to the longer diffusuion length of In with its increased kinetic energy at the higher temperature.

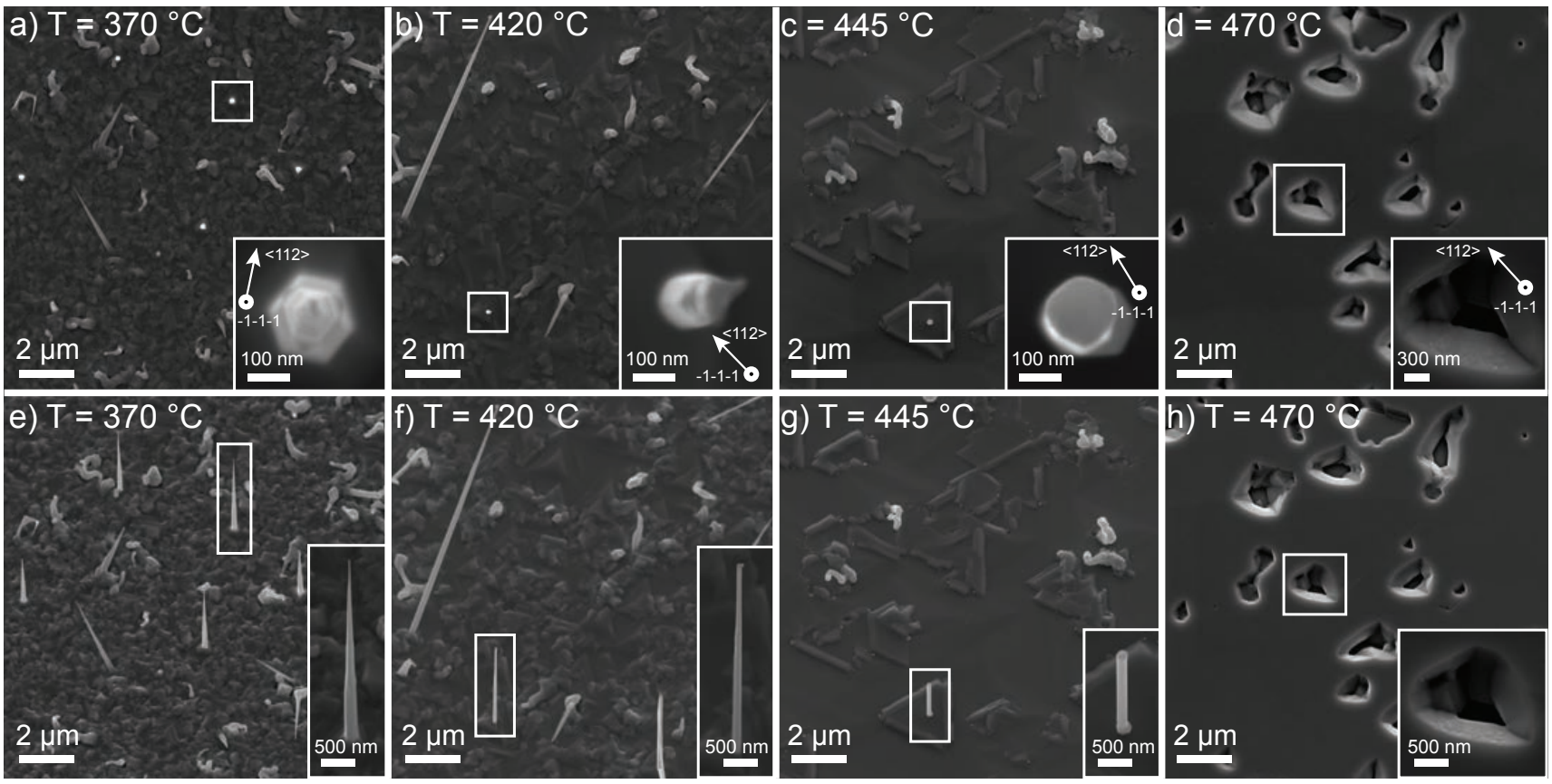

Figure 5.7: The results from the temperature series. Each sample is represented with one top view image (top) and one image tilted by 20° (bottom). Images a) and e) show sample D grown at 370°C, images b) and f) show sample E grown at 420°C, images c) and g) show sample F grown at 445°C and images d) and h) show sample G grown at 470°C. For each image an inset of a higher magnification is included, this area is marked with a white box. Nanowire growth occurred at the lower temperatures 370°C and 420°C. At 445°C nanowires grew only sparsely.

In order to understand the Ag/substrate interaction at the higher temperatures we grew one patterned sample at 500°C (sample X). This temperature was chosen since it is close to the optimum reported temperature for Ag-seeded InAs on Si(111) substrates [35] but according to our temperature series on InAs(111)B substrates all nanowire growth have ceased. During this growth the As_2 pressure was kept constant while the In flux was slightly lowered to $3.3 * 10^{18}$ atoms/$m^2 s$. For the pattern we used an EBL defined 10 nm Ag film in the form of lines and squares in the μm sized range. The results from the growth can bee seen in Figure 5.8. The pattern reveals that the presence of pits in the substrate is a direct consequence of the Ag film. This is further elaborated on in the discussion.

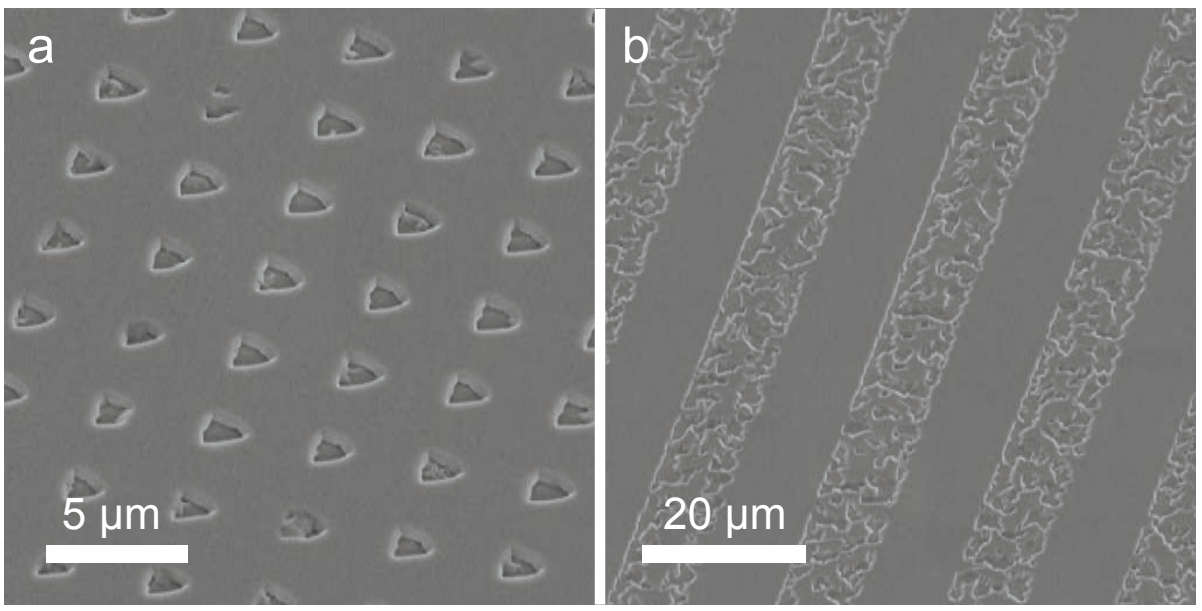

Figure 5.8: Growth at 500°C with 10 nm thick Ag patterns in squares and lines. This sample shows that the pits in the layer growth at the higher temperatures is a direct consequence of the Ag. Image a) shows the remnants of squares with the size of 2x2μm with a spacing of 2μm, b) shows the remnants of lines that are 10μm wide with a spacing of 10μm. Both images are acquired at 45° tilt. The pits only occur where Ag was deposited.

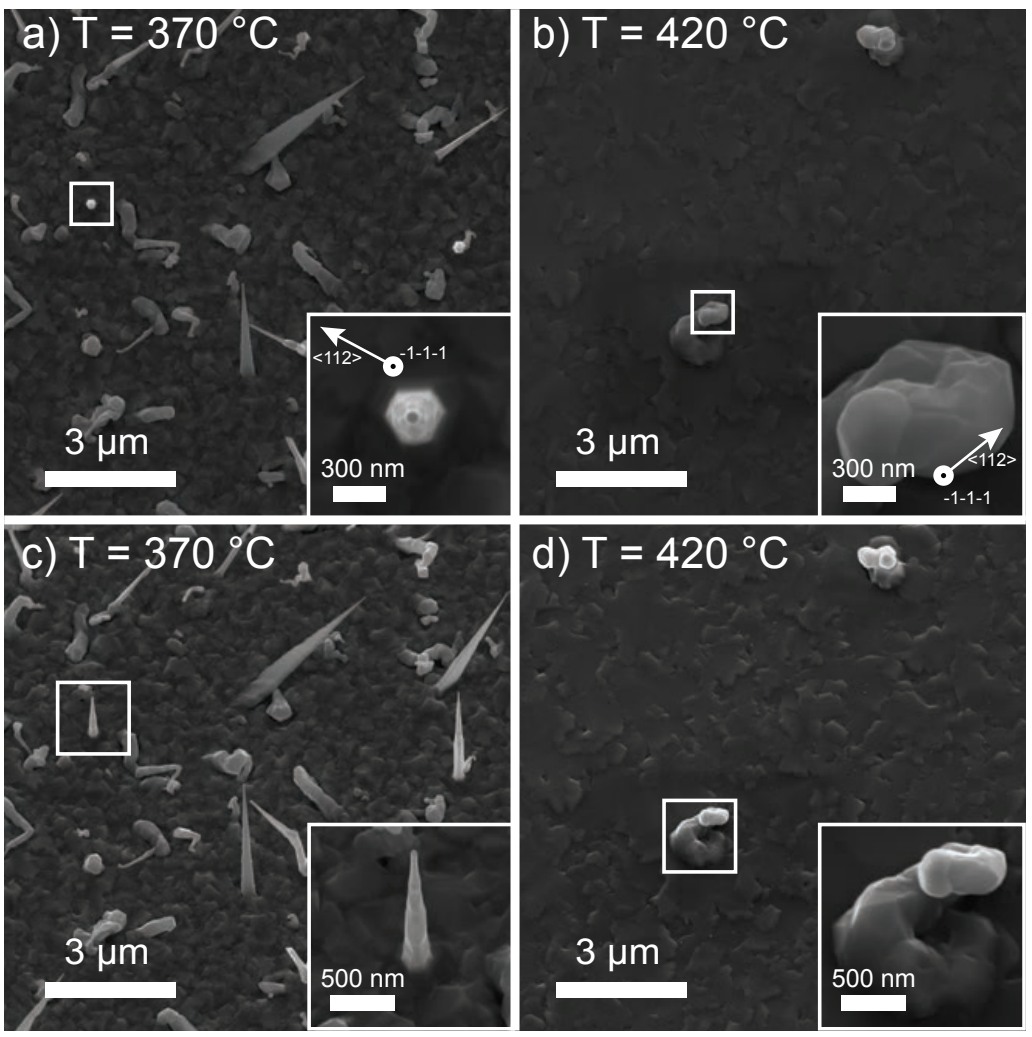

Figure 5.9: Results for sample H and sample I at 370°C and 420°C, respectively, with a low V/III ratio. a) shows a top view image of sample H with an inset of a vertical nanowire. In c) the same area as seen in a) is imaged with 20° tilt, with an inset of the same vertical nanowire. b) shows sample I in top view with an inset of one of the curly nanowires. d) shows the same area as b) but with 20° tilt with an inset of the same curly nanowire.

For both sample B and sample D vertical nanowires seemed to nucleate from mainly small particles compared to the curly nanowires surrounding them, see Figure 5.5 b)

and 5.7 a) and e). For that reason we lowered the Ag thickness to 0.5 nm in order to shift the particle size distribution towards smaller diameters [63, 64, 65]. To increase the possibility of a quick In supersaturation of the particle the In flux was increased to $5.1*10^{18}$ atoms/m^{2}s and the As_2 pressure lowered to $5*10^{-6}$ Torr. Under these conditions growth was performed at two different temperatures, 370°C and 420°C, sample H and I. These temperatures were chosen since they seemed most promising based on the results obtained from sample E-G. Images of the growths for the two temperatures can be seen in Figure 5.9. At 370°C the results are similar to sample D. Both curly, vertical and inclined nanowires are present. The vertical nanowires have {112} facets at the base of the nanowire, which is identified from the substrate orientations. However the facets are changing during growth, see inset in Figures 5.9 c) and d). When increasing the temperature to 420°C most of the nanowires disappear. Instead a low density of curly nanowires grow, see inset in Figures 5.9 b) and d). We relate the absence of growth at the higher temperature 420°C to a lack of As_2 during growth. This is consistent with the previous observations for sample B and C. The higher temperature will result in more As_2 evaporating from the substrate and thereby less As_2 contributing to nanowire growth. The lower As_2, which is giving In a longer diffusion length, also explains the smoother surface for sample H compared to E which are both grown at 420°C.

Crystal structure of Ag-seeded InAs nanowires

TEM has been conducted on samples D and H. These samples were selected since they had high densities of both vertical and inclined nanowires over a large area. For each sample 4-5 nanowires have been imaged with high resolution. Based on the SEM imaging there is a wide variety of nanowires and this is confirmed in the TEM where both samples exhibit straight, kinked, WZ and ZB nanowires. All WZ nanowires on both samples have grown in the <0001>direction. All imaged WZ nanowires consists mainly of WZ with some stacking faults and a few ZB segments. Figure 5.10 shows an image of a typical WZ nanowire. The nanowire shown in Figure 5.10 is from sample H but share a high similarity with WZ nanowires imaged from sample D.

The variety of the ZB nanowires from both sample D and H is greater than the WZ nanowires and no typical ZB nanowire could be distinguished. Figure 5.11 depicts a ZB nanowire (nanosail) with a deformed Ag particle in the top. Deformation of the Ag particle is something we have encountered before for the Ag-seeded GaAs nanowires and the change is due to the Ag in the particle reacting with S or O. The degradation or tarnishing of Ag nanoparticles in ambient air is well known and has been studied earlier [132, 133, 134]. The nanowire shown in Figure 5.11 has grown close to $<31\bar{1}>$ growth direction. We have also imaged nanowires grown in the <220> direction (not shown) on both sample D and H. We can, however, not exclude that more growth directions exist.

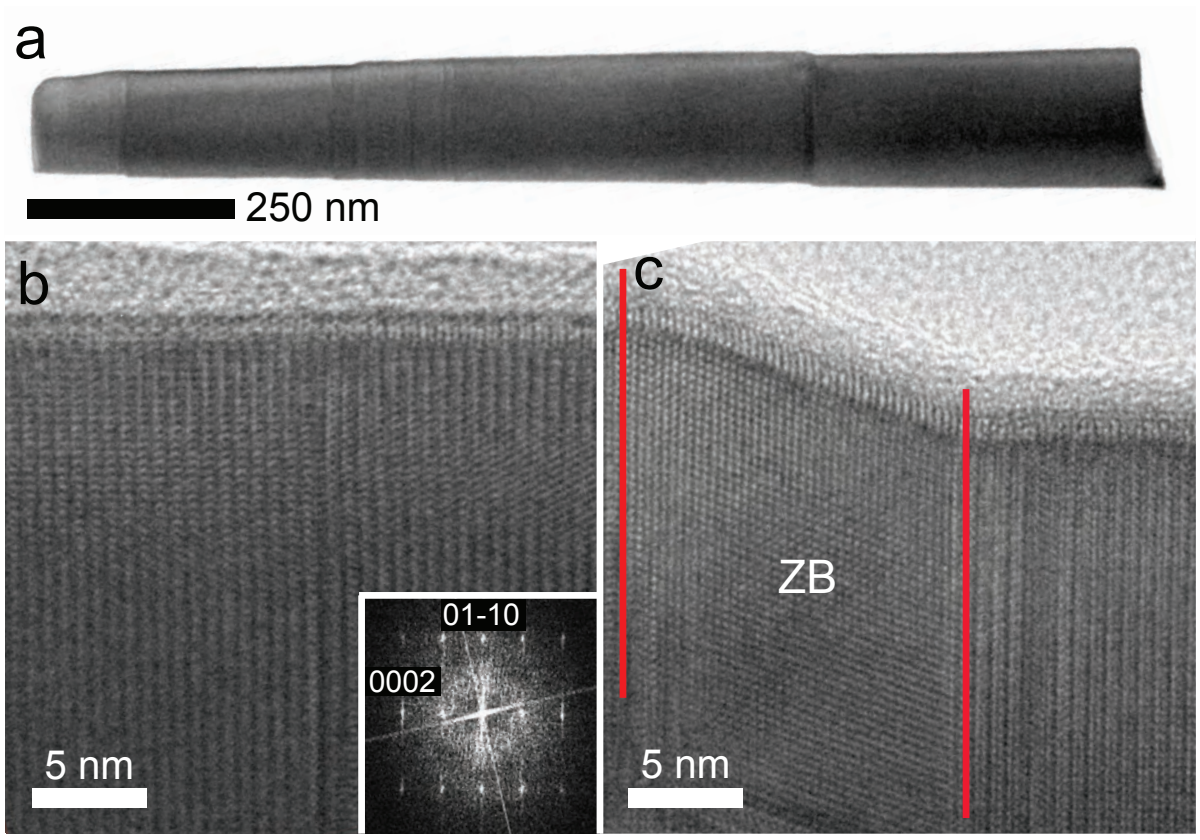

Figure 5.10: WZ nanowire from sample H. a) TEM image of a typical WZ nanowire, b) High resolution image over the WZ lattice and the corresponding FFT. c) one of the short ZB sections (between the red lines) found in the nanowire. The nanowire is imaged along the zone axis $[2\bar{1}\bar{1}0]$. Image acquired jointly with Sara Martí Sánchez.

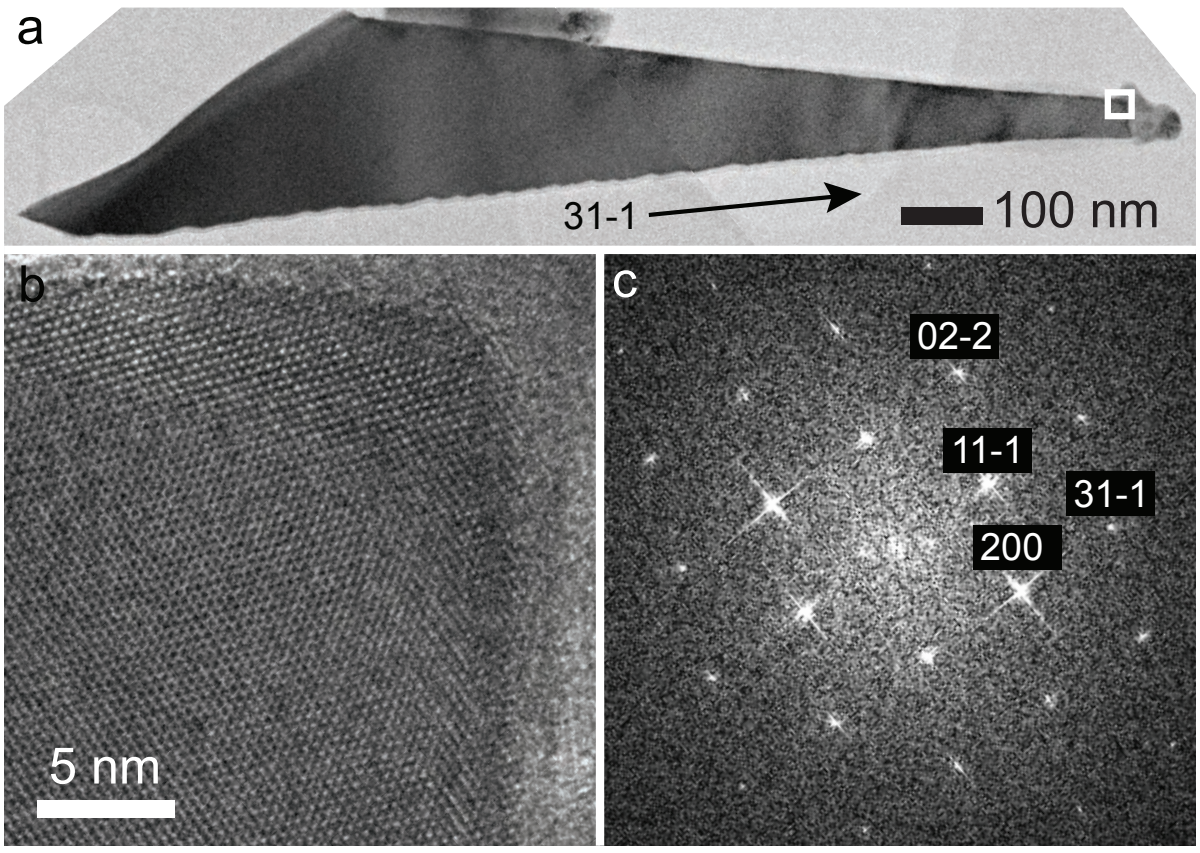

Figure 5.11: a) overview over one of the different ZB nanowires from sample D. The top of the nanowire shows a particle that has undergone a reaction with S. The black arrow indicates the $<31\bar{1}>$ direction which is closest to the growth direction for the low index planes. b) A high magnification image of the white square close to the top in a). The ZB crystal structure is clearly visible. c) the corresponding FFT of image b). The nanowire is imaged along the zone axis [011]. Image acquired jointly with Sara Martí Sánchez.

XEDS in ADF-STEM mode has been performed on nanowires with particles. Two examples of such wires can be seen in Figure 5.12. The nanowire in Figure 5.12 a) is the same nanowire as in Figure 5.11 from sample D and b) shows the particle in the top

of a curly nanowire from sample H. The higher intensity of the particle in the STEM image shows the higher atomic number in the particle and XEDS (not shown) confirmed that the particles consisted of Ag. Most particles also contained S. Due to the change of morphology of the Ag particles no reliable quantification of the composition of the particle was performed. XEDS on the stem of the nanowires showed no detectable amount of Ag in the InAs nanowire.

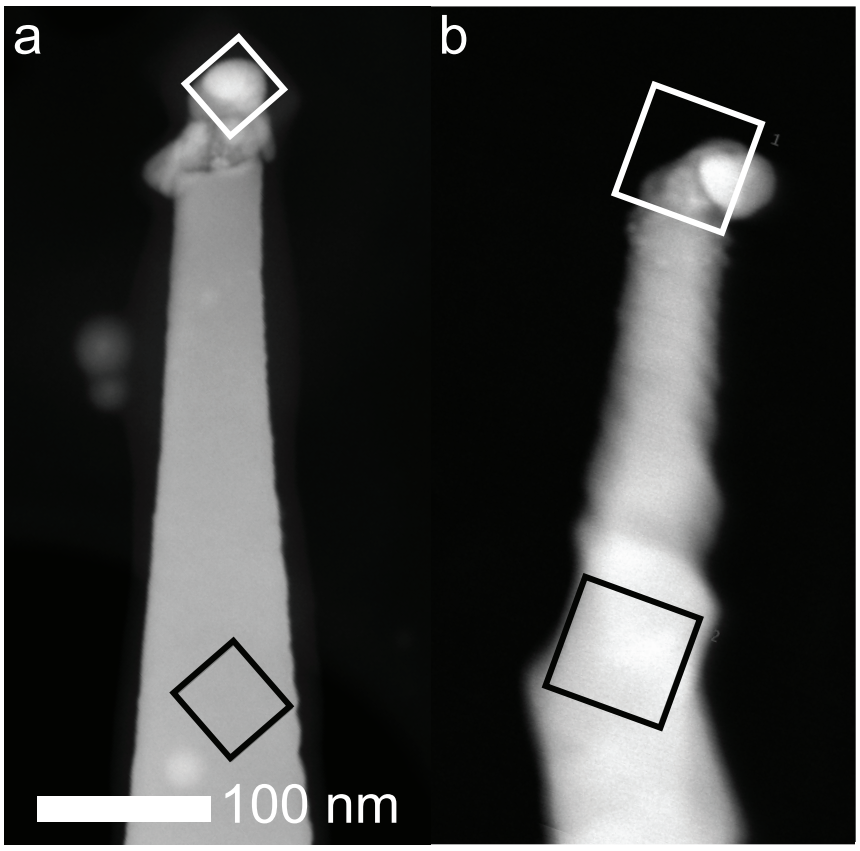

Figure 5.12: ADF-STEM images over two nanowires from sample D and H respectively, a) the ZB nanowire also presented in Figure 5.11 and b) a curly nanowire. The squares in the images indicate where XEDS spectra have been acquired. XEDS (not shown) at the brighter particles confirm the presence of Ag. On most spectra on the particle, S is also present due to a reaction with Ag. Image acquired jointly with Sara Martí Sánchez.

5.3.3 Discussion for Ag-seeded InAs nanowire growth

Temperature

Earlier reports with Ag-seeded InAs nanowires on Si substrates obtained their best results at 505°C [35]. They also report a low density of nanowire growth at 560°C and a cut-off temperature at 600°C. Pan et al. [35] relate the higher cut-off temperature for Ag-seeded InAs nanowires compared to the Au-seeded counterparts to the higher melting point of the Ag-In alloy compared to the Au-In alloy. In contrast to the results for Pan et al. our growth window (370°C - 445°C) for Ag-seeded InAs nanowires is very similar to the growth window for MBE when using Au as a seed particle [129, 130, 131].

The cease of nanowire growth when increasing the temperature can in general depend on one or several of three suggested mechanisms: First, the increased kinetic energy of the group III atoms can increase their desorption rates [47] and thus decrease the effective In flux and subsequentally lower the supersaturation of the Ag particle, thereby preventing nanowire nucleation. Second, Ag reacts with the substrate in a way that prevents the nanowire from from nucleation. Third, the cease of nanowire growth might depend on the seed particle transitioning from solid to liquid phase, as established by Dick et al. [56]

for Au-seeded MOVPE growth. The exact cause for the cease of nanowire growth and instead appearance of pits at higher temperatures is hard to discern solely based on the experiments performed in this work. What is apparent is that already during annealing Ag reacts and forms an alloy with the substrate, creating pits. During growth these pits are not filled but rather enlargened and the particles disappear. Triangular pits during annealing of InAs substrates in the vicinity of Au have been reported before [135, 136] and are attributed to an increased As evaporation in proximity to the Au. Dubrovskii et al. [136] report a prolonged nucleation time for these particles since they become buried in the substrate before the growth is started.

In MBE growth it is known that at higher temperatures an overpressure of As_x needs to be kept in order to prevent the As species in the substrate from evaporating and leaving the group III species to form metallic droplets due to the non-stoichmetric conditions formed. This phenomenon happens when the temperature goes above the congruent evaporation temperature for the substrate, see [137] and references therein. Although Veresegyhazy et al. [138] do not use the phrase congruent evaporation temperature they report that Au lowers the temperature at which the As evaporates from the substrate and thereby catalyzes decomposition of the substrate during annealing. The pits formed in our annelaing experiments show that a similar phenomenon happens with Ag.

Consequently it is reasonable to assume that Ag, in the same way as Au, locally decreases the congruent evaporation temperature for InAs and in the annealing experiments the excess In probably forms an alloy with the Ag. The evaporation of As from the InAs will hinder or decrease the layer growth locally resulting in pits instead of nanowire growth at higher temperatures. However even if the Ag particles had not decomposed the substrate the local In or As fluxes might still be too low to supersaturate the particle and induce nanowire growth. The results by Pan et al. [35] show that it is possible to grow Ag-seeded InAs nanowires at higher temperatures than 445°C on other substrates than InAs, further adding to the suspicion that the substrate-particle interaction is one of the main effects for the limited growth window in our experiments. For our first temperature series we have used the maximum As_2 pressure available in our system. It is, however, probably possible to increase the temperature growth window by increasing the As_2 pressure since the congruent evaporation temperature is reported to increase with an increased As_4 pressure [137].

Phase of the particle

Looking at the Ag-In phase diagrams [139] reveals no interesting phase transistions (as in solid to liquid) at 470°C unless we have a seed particle consisting of at least 40 at% In. To have a pure liquid particle the In content needs to be as high as 57 at%. Considering that Pan et al. [35] reported an In content of 13-25 at% in the Ag particle at higher V/III ratios than ours a pure liquid particle seems unlikely. For the Ag-As phase diagram there is a new phase ζ appearing at 446°C [32] which could be of interest. The Ag-As phase diagram also has a eutectic point at 540°C. Unfortunately we can't say whether or not As is inside the Ag particle during growth. However since Pan et al. [35] do not report any As content we assume that it is low if it exists. This means that neither the ζ phase nor the eutectic point have any impact on the growth of the InAs nanowires. It is known that the size of nanoparticles can alter melting temperatures [47] and although not included in the scope of this work, it would be interesting to perform RHEED experiments similar

to Harmand et al. [140] and Tchernycheva et al. [100] in order to determine whether the growth is following a VLS or VSS growth mode. However based on the phase diagrams we reach the same conclusion as Pan et al. [35] that all of our nanowire growth takes place in a VSS mode.

Crystal structure

All WZ nanowires have grown in the <0001> direction while all ZB nanowires have grown in other directions than the common <111> directions. We therefore argue that the vertical nanowires are adopting a WZ crystal structure while inclined and curly nanowires adopt a ZB crystal structure. This is similar to the Ag-seeded GaAs nanowires when all nanowires were vertically grown on (111)B substrates, hence grown in the [111]B direction, the nanowires exhibited a WZ crystal structure. All nanowires grown in the [100] direction, however, exhibited a ZB crystal structure. This phenomena is further supported by the fact that WZ/ZB swithing mainly occurs in the <111> direction [69]. Conversely nanowires nucleating in other directions than <111> would not easily switch to the WZ crystal structure. If the nanowire grew in a <111>B direction the WZ phase was favoured over the ZB phase implying a high group III supersaturation [53] for both growths D and H despite their different V/III ratios of 30 and 8, respectively. During SEM investigations of sample D and H both samples show a six facetted structure with {112} facets in the bottom of the nanowire. The facetting is then observed to switch along the length of the nanowire. Since our vertical nanowires have crystallized in the WZ crystal structure the facets correspond to $\{01\bar{1}0\}$ in the bottom of the nanowire. For Au-seeded GaAs nanowire growth it has previously been reported that $\{01\bar{1}0\}$ type nanowires change into $\{2\bar{1}10\}$ type nanowires when radial growth takes place [141]. In our case we always find the $\{01\bar{1}0\}$ type facetting in the bottom of the nanowire at the low temperatures. This indicates that even though we obtain radial growth on the nanowire the $\{01\bar{1}0\}$ facets are stable enough not to switch to $\{2\bar{1}10\}$ during radial growth. However, increasing the temperature resulted in both $\{01\bar{1}0\}$ and $\{2\bar{1}10\}$ facetted nanowires implying that for our growth parameters the surface energy difference is small enough for both types to co-exist.

5.4 Conclusions for Ag-seeded InAs nanowire growths

We have shown that it is possible to grow Ag-seeded InAs nanowires on InAs substrates. For the experimental conditions tested here the best results were obtained with a high As_2 pressure and a high In flux. Lower As_2 pressures or In fluxes resulted to a large extent in curly nanowires. The temperature growth window with a high As_2 pressure and In flux is similar to MBE grown Au-seeded InAs nanowires. Ag-seeded InAs nanowires can grow in the temperature range 370°C to 445°C and the nanowires are most probably growing with a VSS growth mechanism. We propose that the cease of nanowire growth at 470°C is due to a substrate-particle interaction caused by an increased evaporation of the substrate species close to the metal particle. Vertical nanowires obtained a WZ crystal structure while inclined nanowires resulted in a ZB crystal structure. Although the control of Ag-seeded InAs nanowires on InAs(111)B is far from the controlled growth using Au, our results together with Pan et al. [35] and Meyer-Holdt et al. [36] show that Ag is indeed a promising material for InAs nanowire growth in MBE.

Chapter 6

TEM on InAs and GaAs nanowires for investigation of the forbidden LO mode with Raman spectroscopy

This chapter is adapted from a soon to be submitted paper with the title-in-work "Raman Spectroscopy in the detection of stacking fault density in InAs and GaAs nanowires" [142]

6.1 Introduction

One of the main advantages with nanowires is the controlled crystal structure that can be achievied during growth [68]. A common way to investigate the crystal structure of semiconductor nanowires is by TEM. TEM is an excellent method to get in depth information regarding the purity of the crystal structure and the position and types of defects within the nanowire. TEM can, however, be very time consuming and is dependent on an electron transparent sample, therefore alternative ways of evaluating the purity of the crystal structure are of interest. One technique that has proven sensitive to stacking faults (SFs) and crystal defects (in this text meaning any interruption of the WZ crystal structure) within semiconductor nanowires is Raman spectroscopy [143, 144]. Raman spectroscopy is a non-destructive method which also has the advantage that measurements can be conducted on nanowires lying on a substrate. This makes it possible to use Raman spectroscopy to measure on nanowires integrated in devices, something that is not possible with TEM. If not being careful TEM also has the drawback that the properties of the nanowire might be altered while irradiated with the electron beam [145]. This chapter presents the results from our investigation on how the LO mode in Raman spectroscopy can depend on the crystal defects, more specifically the number of defects, in WZ InAs and GaAs nanowires grown in the <0001> direction. In the investigation we have first performed TEM on InAs and GaAs nanowires, followed by Raman spectroscopy on exactly the same nanowires. Our main focus has been on InAs nanowires but to be able to compare the two different systems we also performed measurements on GaAs nanowires.

6.1.1 Raman spectroscopy on nanowires

Raman spectroscopy employs inelastic light scattering within a material to probe optical phonons. In semiconductors, Raman spectroscopy can also reveal properties such as crystal structure, electronic states, composition and more [146]. The basic principle behind Raman spectroscopy is: a material is irradiated with a laser beam, the inelastic response is sampled and the difference in frequency (Raman shift) of the measured peaks corresponds to a phonon mode. For III-V semiconductors in the ZB form the optical phonon modes are the longitudinal (LO) and the transverse (TO) modes.

Which of the LO or TO modes or if both modes are present can be theoretically predicted by Raman selection rules and for WZ GaAs and InAs nanowires grown along the <0001> direction the LO mode is forbidden [147]. Even so the LO mode in both InAs and GaAs WZ (although not pure WZ) nanowires have been detected [144, 147, 148]. The origin of forbidden LO modes in nanowires have been explained in different ways: a) phonons near the Brillouin zone center contribute to the spectra [149], b) the change of crystal structure and formation of new facets along the nanowire [144] and c) resonance effects [147, 150]. If the forbidden LO mode appears due to crystal defects within WZ nanowires the intensity should depend on the density of SFs/crystal defects. That the Raman spectra can be affected by SFs/crystal defects has already been shown for GaAs [144] and Si [143].

6.2 Method

The InAs nanowires were grown with MOCVD at Lund University. During growth the AsH_3 was repeatedly changed in order to grow nanowires with a graded density of SFs. In the bottom, the nanowire should be pure WZ, with an increasing density of SFs towards the Au particle. The GaAs nanowires measured were Ag-seeded GaAs nanowires grown with MBE at 600°C (the same kind as seen in Figure 4.13 in chapter 4) and we deliberately measured on the nanowires with an increasing SF density towards the facetted top. A Si TEM grid with nine regularly spaced holes covered with a 50nm thick Si_3N_4 film was used. The nanowires were physically transferred to the TEM grid by simply scratching the grid on the nanowire substrate. The relatively small imaging area on the grid together with a relatively low density of nanowires on the TEM grid made it possible to mark and keep track of single nanowires in the TEM and the Raman spectroscopy setup. This is shown in Figure 6.1 where a) shows a schematic image over the Si TEM grid, b) shows a low resolution image over the whole TEM grid and c) shows an overview image over one of the rectangular holes with three nanowires marked.

We first analyzed the nanowires with a Philips CM20 TEM operated at 200 kV. The crystal structures of the pure WZ parts of the nanowires were determined with selected area diffraction (SAD) and images with a magnification of 100-350kX were acquired. To increase the contrast of the SFs the nanowires were tilted slightly off the zone axis. For the InAs nanowires images were acquired at five different positions, at the bottom, at 1/4, 1/2 and 3/4 of the nanowire length and in the top of the nanowire. For the GaAs nanowires images were acquired so that the whole nanowire could be stitched together. Raman spectroscopy was performed with a μ-Raman setup in back-scattering geometry. We used the excitation lines 514.5 and 488 nm from an argon-ion laser (CVI Melles-Griot 35MAP431-200) and the 632.8 nm excitation line from a HRR170-HeNe laser,

respectively. For each nanowire a number of Raman spectra were collected along the length of the nanowire. We also performed a line scan with 100 nm in step size. Before the Raman measurements, the backside of the TEM grids were covered with either 5 nm Al (GaAs sample) or 3 nm Al followed by 0.5 nm Au (InAs sample). This was done in order to increase the heat transport away from the sample since the heat can affect the measurements. From SEM or TEM images we measured the position for the Raman spectroscopy. Based on these measurements we identified the areas measured with Raman specroscopy in the acquired TEM images and subsequently calculated the number of SFs/crystal defects on that specific site. For the GaAs nanowires and the lower parts of the InAs nanowires the Raman spectroscopy and SF/crystal defect density calculations were performed at the same site. For the upper parts of the InAs nanowires these sites were approximated from the obtained TEM images. We also performed high resolution imaging with a JEOL 3000F microscope operating at 300kV. Based on the results from the low magnification images and the Raman spectroscopy data we targeted interesting regions and performed a full mapping over one of the InAs nanowires.

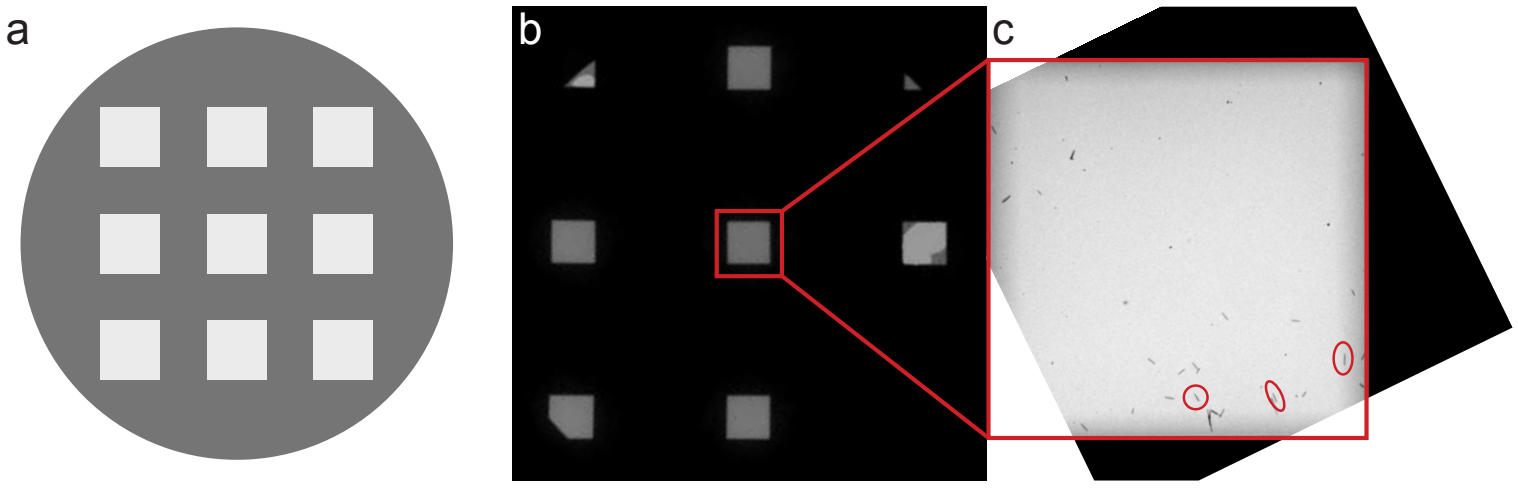

Figure 6.1: Illustration over the Si TEM grid with a Si_3N_4 film deposited with InAs nanowires. a) schematic image over the Si TEM grid. b) low resolution TEM image over the grid. c) overview image over one of the grid holes with the nanowires marked.

6.3 Results

6.3.1 InAs nanowires

Crystal Structure

In general the nanowire could be divided into three different segments. The lower part of the nanowire only had a few SFs in the very bottom. Further up an almost pure WZ crystal structure was revealed, see Figure 6.3 c). On these two segments SAD showed that all five measured nanowires had the WZ crystal structure. After $\sim$0.6μm of the nanowire length the change in AsH_3 flow resulted in a high density of SFs/crystal defects and further up along the nanowire the density of SFs/crystal defects are increasing, see Figure 6.3 b). For each nanowire we measured the position of the Raman measurement and from the TEM images acquired with the CM20 we calculated the SF/crystal defect density. For the lower part of the InAs nanowires the location of the Raman measurement and calculated TEM area are matched. For the upper part the position is approximate based on the acquired TEM images. (For the GaAs nanowires the Raman measurements

and the TEM positions are matched.)

As mentioned in the method 6.2 we also performed a full mapping of one of the InAs nanowires. For this purpose HR imaging of the full length of the InAs nanowire was performed. The deposited metal on the TEM grid had formed small metal particles in different shapes, see Figure 6.2. The metal particles, behind the nanowire, made it possible to stitch the different TEM images together even at very high densities of crystal defects. Based on this we calculated the number of SFs/crystal defects at each 50 nm section along the whole nanowire. In this calculation each consistent ZB segment or SF is regarded as one crystal defect. We added the 50 nm sections together to get a number of the crystal defect density of 250 nm sections (size of the Raman beam), with 100 nm intervals to match the Raman line scan. TEM imaging of this InAs nanowire also showed that close to the Au particle the crystal structure exhibited so many SFs/crystal defects/ ZB sections that it was hard to discern if the nanowire was WZ or ZB. Close to the top of the nanowire ZB segments of at least 6 atom rows were present and most probably shorter sections of higher order polytypes exist as well. We also noted that the nanowires exhibited a clear transition region between the relatively pure WZ segment and the high SF/crystal defect density region. This transition region displayed a prominent kink which included a more extended ZB region or regions, see Figure 6.4 d) or Figure 6.6 b). For the mapped nanowire two smaller kinked regions were also present.

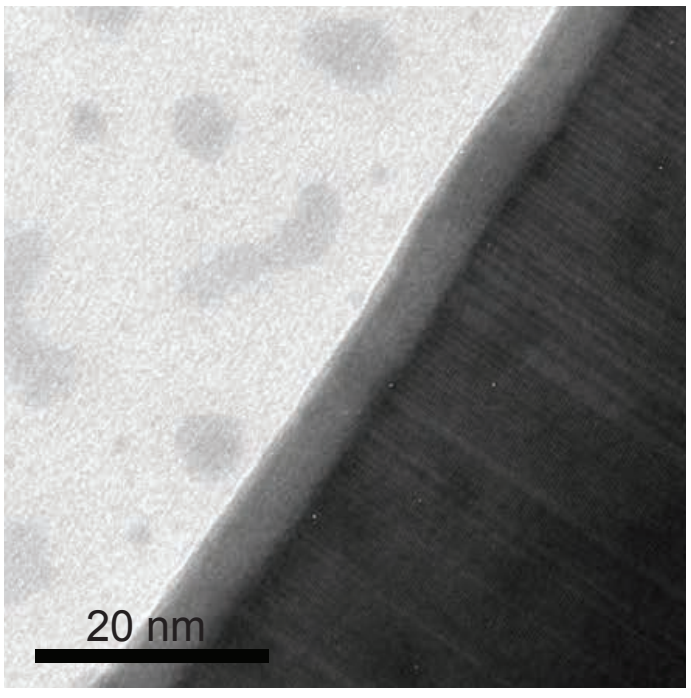

Figure 6.2: TEM image with the metal particles spread on the TEM grid used to identify the position of the image on the nanowire.

Raman spectroscopy

Two Raman spectra recorded at the excitation wavelength 514.5 nm are seen in Figure 6.3 d) and e). The spectrum in d) is collected at a high SF density region while the spectrum in e) is collected at a low SF density region. In both spectra the LO peak is colored green for illustration and the spectrum collected at an area with a higher density of SFs has a higher intensity of the forbidden LO mode.

Both the TEM and Raman spectroscopy results from the mapping of the InAs nanowire are shown in Figure 6.4. HR images of the three different regions are presented in c)-e). c) shows a high SF density region, d) the kink and e) the pure WZ region. Red arrows mark short ZB sections where $(11\bar{1})$ microfacets have formed. f) shows the number

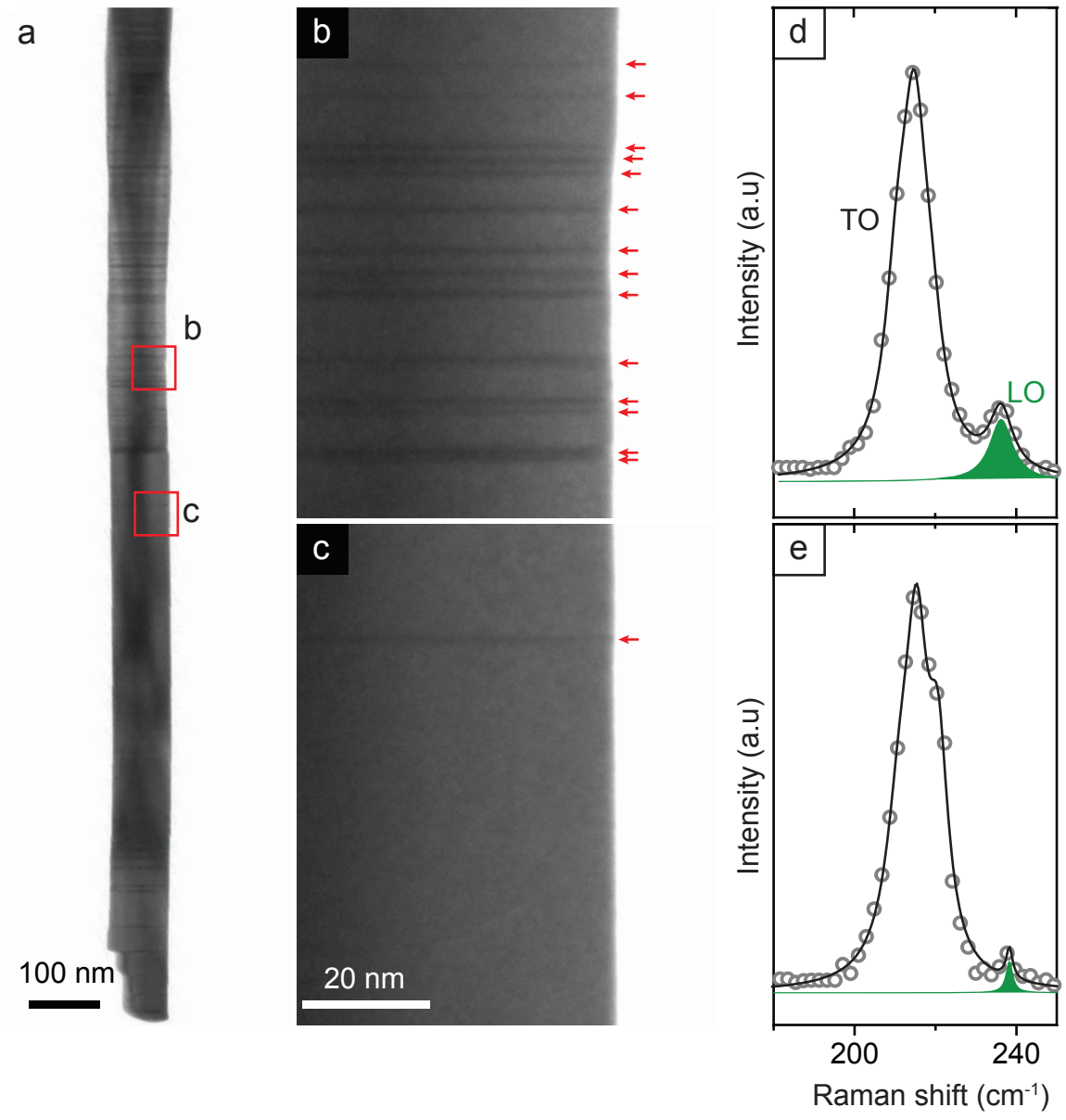

Figure 6.3: a) TEM image over the lower half of a typical InAs nanowire. b) higher magnification TEM image of the region marked b) in image a) showing a nanowire region with multiple SFs. c) higher magnifiaction TEM image of the area marked c) from image a) depicting a nanowire region with an almost pure WZ segment. The red arrows in b) and c) indicate the SFs/crystal defects. d) and c) Raman spectra acquired at a high SF density region and a low SF density region, respectively. The black lines are the Raman spectra collected with a parallel polarization and an excitation energy of 514.5 nm. The green areas show the deconvoluted LO peaks. Partly adapted from reference [142].

of SFs throughout the nanowire. As seen in f) the density of SFs/crystal defects is increasing along the nanowire. The intensity map of the normalised LO peak, from a 488 nm perpendicularly polarized excitation energy, is seen in Figure 6.4 a), the LO mode intensity is low in the bottom of the nanowire and is increasing towards the top, following the SF density. In the intensity map in a) we could see a small section with a higher LO mode intensity compared to its surroundings, this area is marked with a white d. Comparing the intensity map with the TEM overview in b) this section corresponds to the kink which displays elongated ZB sections and $(11\bar{1})$ microfacets. g) shows the LO mode intensity versus the number of SFs. As predicted by a) and b) the intensity of the LO mode is increasing with the SF density.

A similar trend is seen in all nanowires investigated. Figure 6.5 a) and b) shows the LO intensity versus the number of SFs/crystal defects for five different nanowires. For this quantification the number of SFs/crystal defects is estimated from TEM images with a lower magnification compared to the mapped nanowire, thus the lower number of SFs/

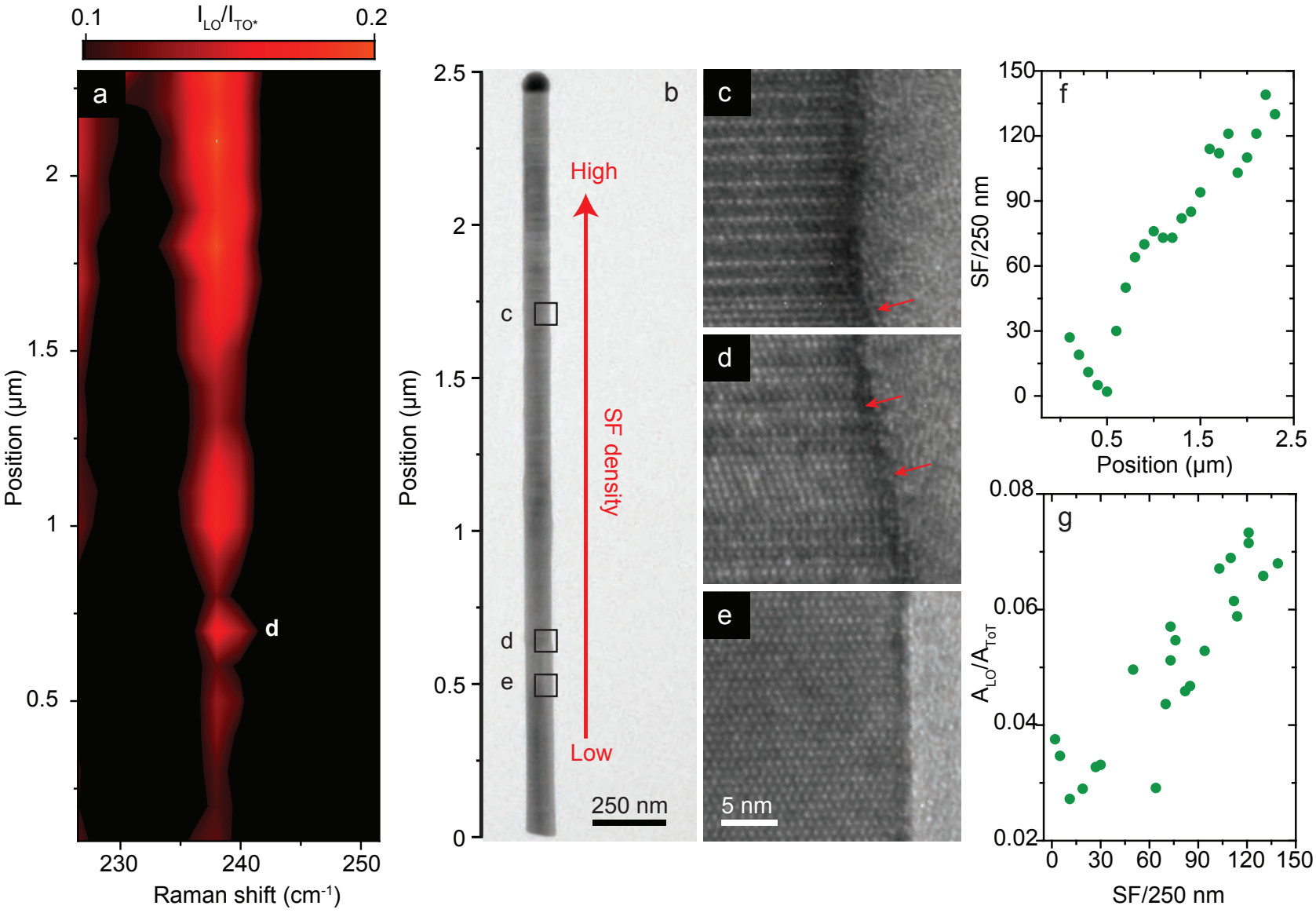

Figure 6.4: a) intensity map of the LO mode along the nanowire imaged in b), note the increase of the LO mode at the area marked with d. b) overview image over the nanowire. The red arrow indicates the direction of an increasing SF density. c) HR image over a region with a high density of stacking faults. d) HR image over the kink in this nanowire. The red arrows in both c) and d) indicate some of the short $(11\bar{1})$ surfaces formed due to short ZB sections. e) HR image over SF free region. Each of the areas in c)-d) are marked in image b) with black squares. f) calculated SFs/crystal defects along the length of the nanowire. g) relative intensity of the LO peak (normalised to the total area of the spectrum) relative the number of SFs. TEM images acquired by Sebastian Lehmann in the $[2\bar{1}\bar{1}0]$ zone axis. Partly adapted from reference [142].

crystal defects. While the exact number is uncertain the indicated trend should still be valid. Both excitation wavelengths, 514.5 and 488 nm, show similar increase with the number of SFs for both parallel and perpendicular polarization. We did, however, notice four data points, marked with black arrows in Figure 6.5 a) and b) which displayed a notably higher LO mode intensity. These data points belong to the same nanowire and to find the origin of this increase of LO mode intensity we further investigated the crystal structure for this particular nanowire with focus on the previosly mentioned kink. Figure 6.6 shows the results. In comparison to the nanowire presented in Figure 6.4 this nanowire shows a relatively long ∼20 nm ZB segment with an extended $(11\bar{1})$ microfacet.

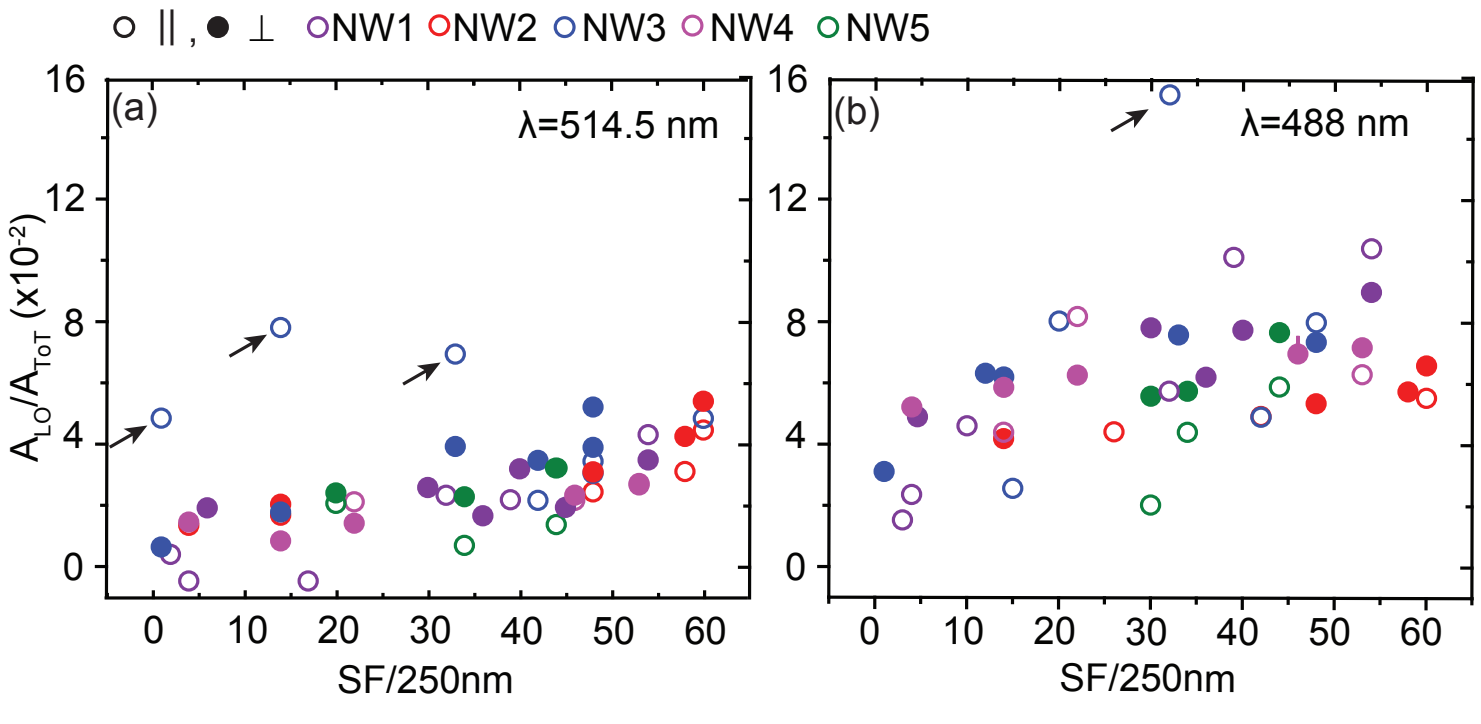

Figure 6.5: a) and b) LO peak intensity versus number of SFs in InAs nanowires at the excitation energy 514.5 nm and 488 nm, respectively. Black arrows in a) and b) point at Raman data from a nanowire with a more pronounced kink. Each color in the spectra represents one nanowire (five in total). Filled or empty circles shows the parallel or perpendicular polarization, repectively. Partly adapted from reference [142].

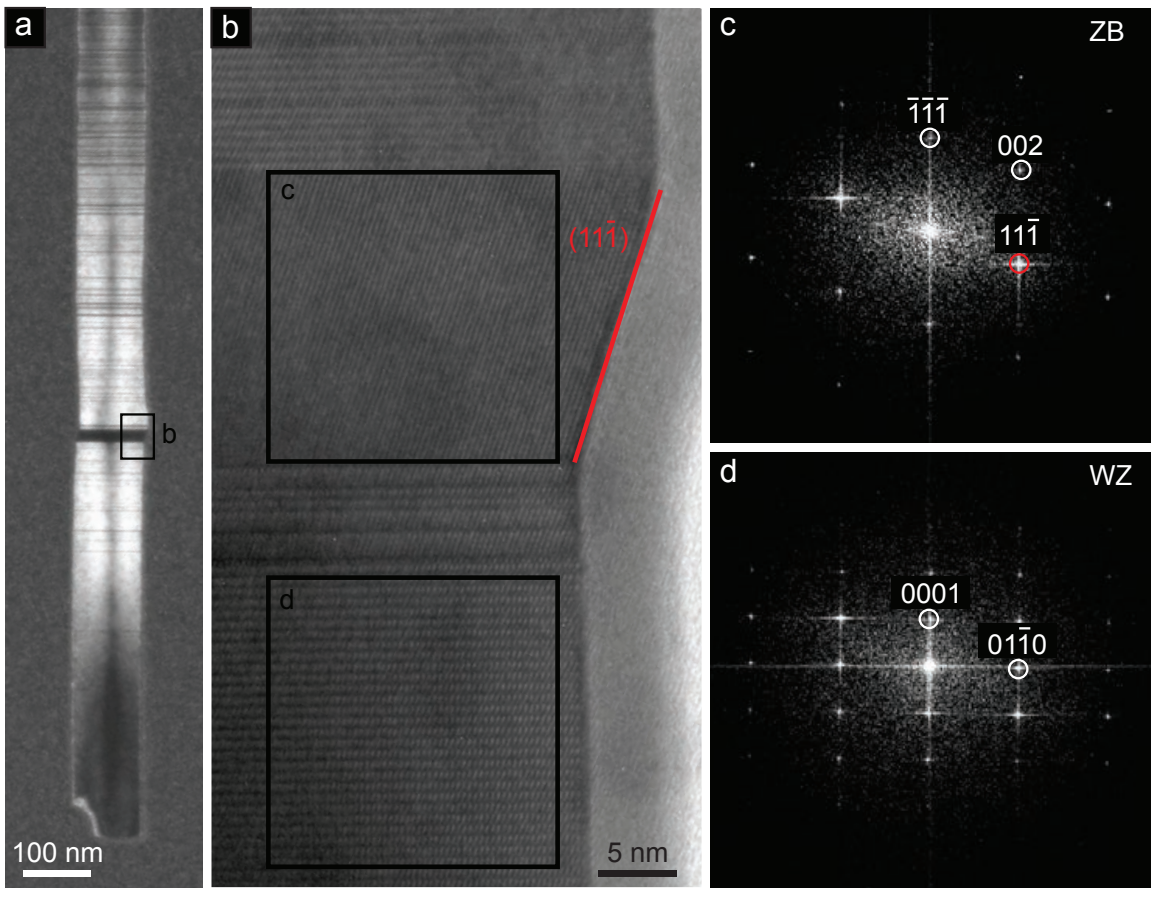

Figure 6.6: TEM images over the nanowire with a long ZB segment in the kink. a) DF image using the diffraction spot (01$\bar{1}$0), hence ZB regions turn out dark. b) HR image over the kink marked in a). The kink consists of a long ZB segment, the (11$\bar{1}$) facet formed is highlighted with a red line. Below the kink is a pure WZ crystal structure. c) and d) the corresponding FFTs for the areas marked in b), the red ring in c) corresponds to the (11$\bar{1}$) direction. The images are acquired in the [2$\bar{1}\bar{1}$0] zone axis by Sebastian Lehmann. Partly adapted from reference[142].

This is similar to the mapped nanowire whose LO mode intensity map showed an increase at the kinked region with multiple $\{11\bar{1}\}$ microfacets. We thus conclude that the increased LO intensity is due to the $\{11\bar{1}\}$ microfacets, where the LO mode is allowed [144].

6.3.2 GaAs nanowires

Crystal Structure

For the GaAs nanowires we used the type of nanowire presented in Figure 6.7 a). As mentioned in chapter 4 the lower half of these nanowires consists of pure WZ. After half the nanowire length single SFs occur. The density of the SFs is increasing closer to the triangular top which consists of pure ZB. See Figure 6.7 a) and f) for TEM overview image and the triangular top with a ZB crystal structure, respectively. The angles of the top facets relative the $(\bar{1}\bar{1}\bar{1})$ plane, measured in TEM images, are $\sim 36°$ and $\sim 20°$. We note that several planes have an angle around 36° relative the $(\bar{1}\bar{1}\bar{1})$ plane, such as $(\bar{1}\bar{1}0)$ at 35.3°, $(\bar{2}\bar{3}0)$ at 36.8°, $(\bar{3}\bar{4}0)$ and $(\bar{1}\bar{1}\bar{4})$ at 36.3°. Of these planes the $(\bar{1}\bar{1}0)$ is most likely since it is a low index plane with low energy. That the three top facets for this particular triangular shape consist of $\{\bar{1}\bar{1}0\}$ planes have been reported earlier [151, 152]. The SF density for the GaAs nanowires was considerably lower than for the InAs nanowires. For the areas measured with Raman spectroscopy the SF density was less than 25 SFs/250 nm. The lower SF density and the slightly shorter nanowires ($\sim 2.5\mu$m for InAs and $\sim$1.6μm for GaAs) made it possible to stitch the TEM images together so that all SF density calculations were performed at the same sites as the Raman measurements.

Raman spectroscopy

For the GaAs nanowires we performed similar Raman measurements as on the InAs nanowires. In this case we used the excitation energies 488, 514.5 and 632.8 nm. Of these excitation wavelengths at least 632.8 nm has previously been reported to have a resonance Raman spectroscopy induced LO peak [153]. The results from our Raman measurements are seen in Figure 6.7 b) and c). In b) two Raman spectra with both the TO and forbidden LO modes are observed. The purple spectrum is acquired at a high SF density region and the green spectrum is acquired at a SF free region, both areas marked in 6.7 a) with a purple and a green ring respectively. The LO peak intensity is higher in the purple spectrum acquired at the high SF density region although a clear LO peak is detected in the SF free WZ region of the nanowire as well. The LO peak integrated area, normalised to the total spectrum area, versus the number of SFs/crystal defects is presented in Figure 6.7 c). For all three excitation energies as well as for both polarizations at 632.8 nm the LO mode intensity is increasing with the density of SFs. In general the overall SF density is lower in the GaAs nanowires than the InAs which can explain why the LO mode increase is not as pronounced as for the InAs. Since each GaAs nanowire displays such a long segment of pure WZ multiple data points from the Raman measurements are acquired at zero SFs. Both in Figure 6.7 b) and d) the zero SF spectra still show a relatively low LO peak for the excitation energies 514.5 nm and 632.8 nm, showing that for GaAs the detected forbidden LO mode is not purely due to formation of $\{11\bar{1}\}$ facets but also due to for example Resonance Raman spectroscopy effects. This is further supported by Ketterer et al. who report Resonance Raman spectroscopy on

GaAs nanowires at the excitation wavelength 632.8 [153]. For the peak at 488 nm the LO mode intensity is close to zero at the pure WZ part of the nanowire, indicating that the increase of the LO mode is mainly due to the SFs and not due to resonance effects.

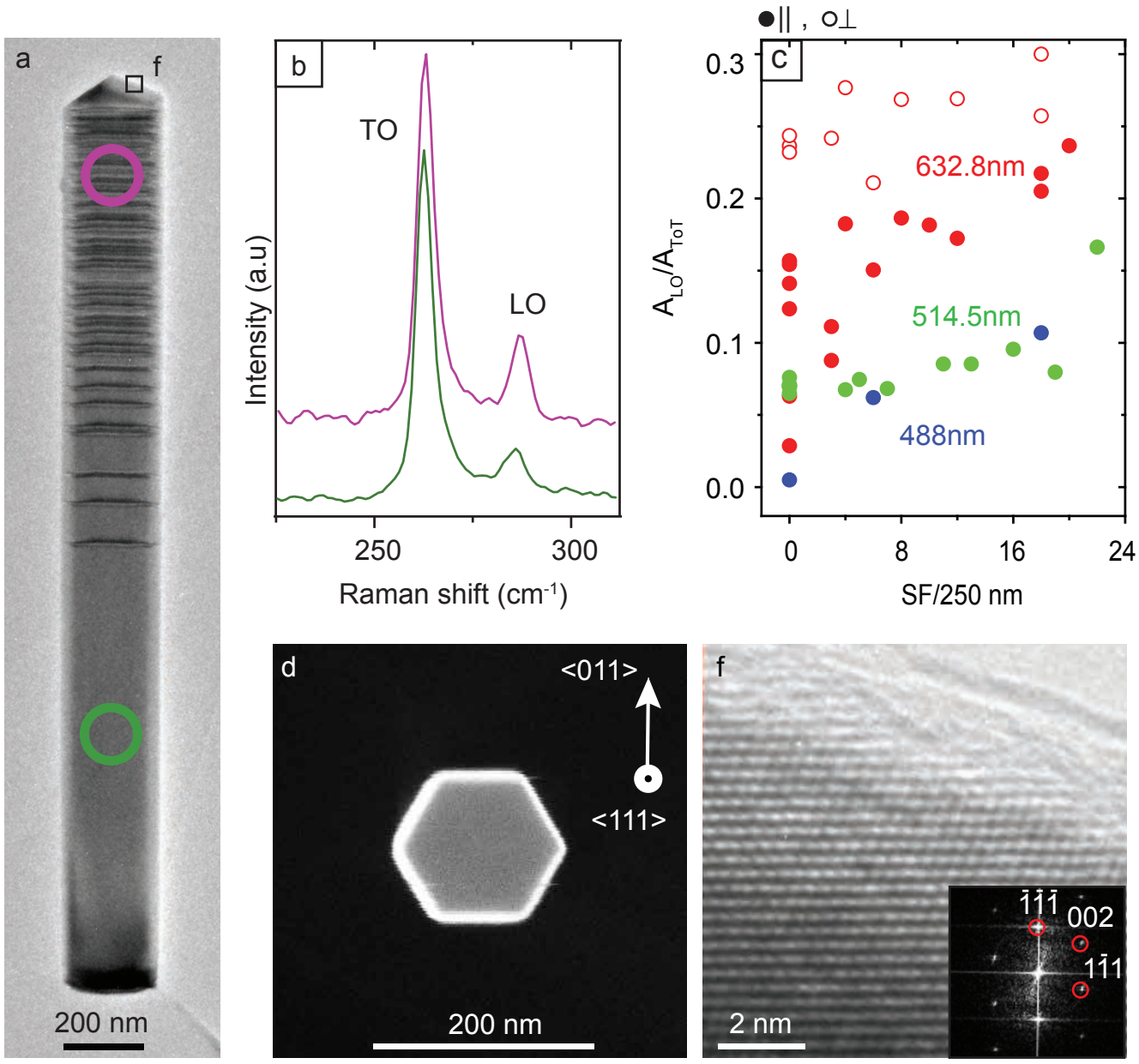

Figure 6.7: a) TEM overview over a facetted nanowire, the SFs start around half way and increase in density closer to the top. b) Raman measurements with the excitation wavelength 514.5 nm on the indicated areas in a), purple (high density of SFs) and green (no SFs). c) normalised LO peak intensity versus SF density. Open circles indicate parallel polarization while closed circles indicate perpendicular polarization. d) top view SEM image of a GaAs nanowire showing the {011} facets. f) HR TEM image from the triangular top showing the ZB crystal structure. Inset in f) corresponding FFT with the typical ZB crystal structure. Partly adapted from reference [142].

6.3.3 Conclusions

We have performed TEM and Raman spectroscopy on InAs and GaAs nanowires to explore the correlation between SFs/crystal defects and the intensity of the forbidden LO mode. By comparing low SF density regions and high SF density regions from the same nanowire we also removed any implications that could arise due to differences in size of the nanowires. We could show that an increase in the number of SFs and crystal defects increased the intensity of the LO mode in both InAs and GaAs nanowires. Based on the experiments from a longer ZB region in one of the InAs nanowires we hypothesize that the main contribution to the increased intensity of the forbidden LO mode on [0001] grown

InAs nanowires is due to small microfacets of {111} planes formed in correlation with SFs/crystal defects, and on {111} planes the LO mode is not forbidden. We have shown that it is possible to detect changes in defect density along the nanowire based on the forbidden LO mode intensity of WZ nanowires. However based on these measurements we cannot conclude whether a single SF can be detected, and if so that would probably need a calibration which might need to include the size of the nanowires [154].

Chapter 7

Summary and Outlook

This work has mainly been focused on the formation of GaAs and InAs nanowires from a Ag particle. This instead of the conventional techniques such as Au-seeded and SC nanowires. We have performed a thorough growth study on Ag-seeded GaAs nanowires and screened the basic growth parameters for Ag-seeded InAs nanowires.

For the GaAs nanowires experiments have been performed on both GaAs(111)B and GaAs(100) substrates and the basic growth parameters (temperature, As pressure and Ga flux) have been optimized to achieve good nanowire growth. For GaAs(111)B our vertical yield of 100% and an almost pure WZ crystal structure shows that Ag can be used to grow nanowires of the same quality as Au. The cooling neck on our nanowires shows that precipitation of Ga and/or As does occur after the growth has been stopped. This makes it difficult to make any conclusive arguments regarding the phase of the particle based on post-growth XEDS measurements. For the GaAs(100) substrates we have a vertical yield of 45-50%. Although this is far from a perfect yield the results are promising. Especially since we have not performed any optimization by, for example, including nucleation steps or pre-treatment of the substrate.

On InAs substrates we first performed annealing experiments with a 10 nm thin Ag film to confirm particle formation when the substrate is exposed to the normal heating steps performed in an MBE. We then changed the basic growth parameters to find successful growth of Ag-seeded InAs nanowires. We present growth of Ag-seeded InAs nanowires at the lower temperatures 370°C-445°C although the nanowires still grow in different directions and include both straight and curly nanowires. These results are still quite far from the positioned controlled growth of Au-seeded InAs [130, 155, 156] or SC InAs [157] nanowires. Even reaching the yield of vertical nanowires from earlier reports with Ag as seed particle for InAs nanowires on other substrates [35, 36] requires some more experiments. However our results can most probably be further improved upon and Ag seems to be a promising seed material for nanowires in general.

In the last chapter we have investigated how the LO mode in Raman spectroscopy depends on the SF/crystal defect density. We conclude that increased LO mode intensity in InAs nanowires appears mainly due to $\{11\bar{1}\}$ facets formed in correlation to SFs and short ZB segments. For GaAs the appearence of the forbidden LO mode at the excitation wavelengths 632.8 and 514.5 nm is observed even in the absence of SFs, although we still observe an increase of the LO mode intensity with an increasing amount of SFs.

With the increasing possibilities to use nanowires within different applications [158] the demands on the nanowires will probably also increase. Properties such as controlled growth in different crystal directions, nanowire-substrate combinations and perfect material transitions in nanowire heterostructures will probably become more important with the development of different applications. To meet new demands on nanowires tuning Au-seeded nanowire growth and self catalyzed growth will be important. However by testing different materials as seed particles the possibilities of controlling and gaining new nanowire properties can increase. Although research with other seed materials might not solve all the current (or coming) obstacles that we encounter, our hope is that it will increase our general understanding on how and why nanowires grow and this kowledge might make it easier to solve any future encounters. With more and more materials being systematically tested (such as: Ag [31, 35, 36], Pd [22, 87, 116], Mn [29, 114], Sn [88, 89], Fe [23] and Cu [28, 159]) the possibility to draw conclusions from the materials tested and find better alternatives will increase. We have also suggested the possibility to tune the particle for the application [31]. Other seed-particles than Au, self catalyzed nanowires or removal of the seed particle will also allow for full integration of nanowires in the Si-based semiconductor industry.

References

[1] M. T. Borgstrom, J. Wallentin, M. Heurlin, S. Falt, P. Wickert, J. Leene, M. H. Magnusson, K. Deppert, and L.Samuelson. Nanowires with promise for photovoltaics. *IEEE Journal of Selected Topics in Quantum Electronics*, 17(4):1050–1061, 2011.

[2] Y. Zhang, J. Wu, M. Aagesen, and H. Liu. III-V nanowires and nanowire optoelectronic devices. *Journal of Physics D: Applied Physics*, 48(463001), 2015.

[3] X Liu, YZ. Long, L. Liao, XF. Duan, and ZY. Fan. Large-scale integration of semiconductor nanowires for high-performance flexible electronics. *ACS Nano*, 6(3):1888–1900, 2012.

[4] C. Zhang and X. Li. IIIV nanowire transistors for low-power logic applications: A review and outlook. *IEEE Transactions on Electron Devices*, 63(1):223–234, 2016.

[5] P. Offermans, M. Crego-Calama, and S. H. Brongersma. Gas detection with vertical InAs nanowire arrays. *Nano Letters*, 10(7):2412–2415, 2010.

[6] J. Du, D. Liang, H. Tang, and X. P.A. Gao. InAs nanowire transistors as gas sensor and the response mechanism. *Nano Letters*, 9(12):4348–4351, 2009.

[7] J. Sim, K. Kim, S. Song, and J. Kim. Suspended GaN nanowires as NO_2 sensor for high temperature applications. *2013*, 138(8):2432–2437, RSC Publishing.

[8] T. Berthing, S. Bonde, C. B. Sørensen, P. Utko, J. Nygrd, and K. L. Martinez. Intact mammalian cell function on semiconductor nanowire arrays: New perspectives for cell-based biosensing. *Small*, 7(5):640–647, 2011.

[9] C. N Prinz. Interactions between semiconductor nanowires and living cells. *Journal of Physics: Condensed Matter*, 27(2015):233103, 2015.

[10] H. G. Lee, H. C. Jeon, and T. W. Kang. Gallium arsenide nanorods grown by molecular-beam-epitaxy. *Applied Physics Letters*, 78(21):3319–3321, 2001.

[11] V. G. Dubrovskii, G. E. Cirlin, I. P. Soshnikov, A. A. Tonkikh, N. V. Sibirev, Yu. B. Samsonenko, and V. M. Ustinov. Diffusion-induced growth of GaAs nanowhiskers during molecular beam epitaxy: Theory and experiment. *Physical Review B*, 71(20):205325, 2005.

[12] A. I. Persson, B. J. Ohlsson, S. Jeppeson, and L. Samuelsson. Growth mechanism for GaAs nanowires in CBE. *Journal of Crystal Growth*, 272(1–4):167–174, 2004.

[13] K. Hiruma, H. Murakoshi, M. Yasawa, and T. Katsuyama. Self-organized growth of GaAs/InAs heterostructure nanocylinders by organometallic vapor phase epitaxy. *Journal of Crystal Growth*, 163(3):226–231, 1996.

[14] W. Seifert, M. Borgstrom, K. Deppert, K. A. Dick, J. Johansson, M. W. Larsson, T. Martensson, N. Skold, C. P. T. Svensson, B. A. Wacaser, L. R. Wallenberg, and Lars Samuelson. Growth of one-dimensional nanostructures in movpe. *Journal of Crystal Growth*, 272(1–4):211–220, 2004.

[15] G. Biasiol and L. Sorba. Molecular beam epitaxy: Principles and applications. In R. Fornari and L. Sorba, editors, *Crystal growth of materials for energy production and energy-saving applications*, pages 66–83. International Study School, 2001.

[16] K. A. Dick and P. Caroff. Metal-seeded growth of III-V semiconductor nanowires: towards gold-free synthesis. *Nanoscale*, 6:3006–3021, 2014.

[17] A. J. Tavendale and S. J. Pearton. Deep level, quenched-in defects in silicon doped with gold, silver, iron, copper or nickel. *Journal of Physics C: Solid State Physics*, 16:1665–1673, 1983.

[18] E. Koren, G. Elias, A. Boag, E. R. Hemesath, L. J. Lauhon, and Y. Rosenwaks. Direct measurements of individual deep traps in single silicon nanowires. *Nano Letters*, 11(6):2499–2502, 2011.

[19] S. A. Fortuna and X. Li. Metal-catalyzed semiconductor nanowires: a review on the control of growth directions. *Semiconductor Science and Techonology*, 25(2):024005, 2010.

[20] HY. Xu, Y. Wang, YN. Guo, ZM. Liao, Q. Gao, H. H. Tan, C. Jagadish, and J. Zou. Defect-free <110>Zinc-Blende structured InAs nanowires catalyzed by palladium. *Nano Letters*, 12(11):5744–5749, 2012.

[21] S. Heun, B. Radha, D. Ercolani, G. U. Kulkarni, F. Rossi, V. Grillo, G. Salviati, F. Beltram, and L. Sorba. Pd-assisted growth of InAs nanowires. *Crystal Growth and Design*, 10(9):4197–4202, 2010.

[22] R. Perumal, ZX. Cui, P. Gille, J-C. Harmand, and K. Yoh. Palladium assisted heteroepitaxial growth of an InAs nanowire by molecular beam epitaxy. *Semiconductor Science and Technology*, 29(11):115005, 2014.

[23] I. Regolin, V. Khorenko, W. Prost, F. J. Tegude, D. Sudfeld, J. Kstner, G. Dumpich, K. Hitzbleck, and H. Wiggers. GaAs whiskers grown by metal-organic vapor-phase epitaxy using Fe nanoparticles. *Journal of Applied Physics*, 101(5):054318, 2007.

[24] Z-A. Li, C. Moller, V. Migunov, M. Spasova, M. Farle, A. Lysov, C. Gutsche, I. Regolin, W. Prost, and F-J. Tegude. Planar-defect characteristics and cross-sections of <001>, <111>, and <112>inas nanowires. *Journal of Applied Physics*, 109(11):114320, 2011.

[25] H. Fonseka, P. Caroff, J. Wong-Leung, A. S. Ameruddin, H. H. Tan, and C. Jagadish. Nanowires grown on InP (100): Growth directions, facets, crystal structures, and relative yield control. *ACS Nano*, 8(7):6945–6954, 2014.

[26] U. Krishnamachari, M. Borgstrom, B. J. Ohlsson, N. Panev, L. Samuelson, and W. Seifert. Defect-free InP nanowires grown in [001] direction on InP (001). *Applied Physics Letters*, 85(11):2077–2079, 2004.

[27] J. Wang, S. R. Plissard, M. Verheijen, L-F Feiner, Alessandro Cavalli, and E. P. A. M. Bakkers. Reversible switching of InP nanowire growth direction by catalyst engineering. *Nano Letters*, 13(8):3802–3806, 2013.

[28] K. Hillerich, D. S. Ghidini, K. A. D. Kimberly, K. Deppert, and J. Jonasson. Cu particle seeded InP-InAs axial nanowires heterostructures. *Rapid Research Letters*, 7(10):850–854, 2013.

[29] F. Martelli, S. Rubini, M. Piccin, G. Bais, F. Jabeen, S. De Franceschi, V. Grillo, E. Carlino, F. DAcapito, F. Boscherini, S. Cabrini, M. Lazzarino, L. Businaro, F. Romanato, and A. Franciosi. Manganese-induced growth of GaAs nanowires. *Nano Letters*, 6(9):2130–2134, 2006.

[30] Y. C. Chou, C. Y. Wen, M. C. Reuter, D. Su, E. A. Stach, and FM. Ross. Controlling the growth of Si/Ge nanowires and heterojunctions using silver-gold alloy catalysts. *ACS Nano*, 6(7):6407–6415, 2012.

[31] C. Lindberg, A. Whiticar, K. D. Dick, N. Skold, J. Nygard, and J. Bolinsson. Silver as seed particle material for GaAs nanowires - dictating crystal phase and growth direction by substrate orientation. *Nano Letters*, 16(4):2181–2188, 2016. http://pubs.acs.org/doi/ipdf/10.1021/acs.nanolett.5b04218.

[32] M. T Baren. The Ag-As (silver arsenic) system. *Bulletin of Alloy Phase Diagrams*, 11(2):113–116, 1990.

[33] H. Okamoto. Au-Ga (gold-gallium). *Journal of Phase Equilibria and Diffusion*, 34(2):174–175, 2013.

[34] K. S. Dick. A review of nanowire growth promoted by alloys and non-alloying elements with emphasis on Au-assisted III-V nanowires. *Progress in Crystal Growth and Characterization of Materials*, 54(3–4):138–173, 2008.

[35] D. Pan, MQ. Fu, XU. Yu, XL. Wang, LJ. Zhu, SH Nie, SL. Wang, Q. Chen, P. Xiong, S. von Molnar, and JH. Zhao. Controlled synthesis of phase-pure InAs nanowires on Si(111 by diminishing the diameter to 10 nm. *Nano Letters*, 14(3):1214–1220, 2014.

[36] J. Meyer-Holdt, T. Kanne, J. E. Sestoft, A. Gejl, LJ Zeng, E. Johnson, J. Nygard E. Olsson, and P. Krogstrup. Ag-catalyzed InAs nanowires grown on transferable graphite flakes. *Nanotechnology*, 27(36):365603, 2016.

[37] A. T. Vogel, J. de Boor, M. Becker, J. V. Witteman, S. L. Mensah, P. Werner, and V. Schmidt. Ag-assisted CBE growth of ordered InSb nanowire arrays. *Nanotechnology*, 22(1):015605, 2011.

[38] S. T. Boles, C. V. Thompson, and E. A. Fitzgerald. Influence of indium and phosphine on Au-catalyzed InP nanowire growth on Si substrates. *Journal of Crustal Growth*, 311(5):1446–1450, 2009.

[39] J. V. Witteman, W. Munchegesang, S. Senz, and V. Schmidt. Silver catalyzed ultrathin silicon nanowires grown by low-temperature chemical-vapor-deposition. *Journal of Applied Physics*, 107:096105, 2010.

[40] M. Dutta, L. Thirugnanam, K. Sato, and N. Fukata. Diameter-controlled growth and impurity doping of silver colloid-seeded silicon microwires to nanowires for the realization of solar cell materials. *Materials Express*, 3(1):85–91, 2013.

[41] X. Duan and C. M. Lieber. General synthesis of compound semiconductor nanowires. *Advanced Materials*, 12(4):298–302, 2000.

[42] A. V. Bjørlig. Ag catalysed InAs nanowire growth and scanning electron microscopy. Bachelor thesis, Copenhagen University, 2015. I co-supervised the project.

[43] M. A. Herman and H. Sitter. *Molecular Beam Epitaxy Fundamentals and Current Status*. Springer Series in Materials Science 7. Springer Verlag Berlin Heidelberg, Druckhaus Beltz, 6944, Hemsbach/Bergstr., 1989.

[44] M. H. Madsen. *Indium Arsenide Nanowires - Fabrication, Characterization and Biological Applications*. Phd thesis, Copenhagen University, 2012.

[45] P. Laukkanen, J. Sadowski, and M. Guina. Surface studies by low-energy electron diffraction and reflection high-energy-electron diffraction. In *Semiconductor Research Experimental Techniques*, volume 150 of *Springer Series in Material Science*, chapter 1. Springer Berlin Heidelberg, 2012.

[46] B. Junno, S. Jeppesen, M.S. Miller, and L. Samuelsson. A comparison of RHEED reconstruction phases on (100) inas, gaas and inp. *Journal of Crystal Growth*, 164(1–4):66–70, 1996.

[47] D. L. Smith. *THIN-FILM DEPOSITION*. Mc Graw Hill, 1221 Avenue of the Amercas, New York NY, 10020, USA, 1995.

[48] I. V. Markov. *Crystal Growth for Beginners: Fundamentals of Nucleation, Crystal Growth and Epitaxy*. World Scientific Publishing Co. Pte. Ltd., 5 Toh Tuck Link, Singapore, 596224, 2003.

[49] E. Clouet. Modeling of nucleation processes. *ASM Handbook*, 22A:203–219, 2009.

[50] F. Glas, J. C. Harmand, and G. Patriarche. Why does wurtzite form in nanowires of III-V Zinc-Blende semiconductors? *Physical Review Letters*, 99(14):146101, 2007.

[51] R. S. Wagner and W. C. Ellis. Vapor-liquid-solid mechanism of single crystal growth. *Applied Physics Letters*, 4(5):89–90, 1964.

[52] E. I. Givargizov. Fundamental aspects of VLS growth. *Journal of Crystal Growth*, 31:20–30, 1975.

[53] F. Glas, J-C. Harmand, and G. Patriarche. Nucleation antibunching in catalyst-assisted nanowire growth. *Physical Review Letters*, 104(13):135501, 2010.

[54] P. Krogstrup, S. Curiotto, E. Johnson, M. Aagesen, J. Nygard, and D. Chatain. Impact of the liquid phase shape on the structure of III-V nanowires. *Physical Review Letters*, 106(12), 2011.

[55] A. I. Persson, M. W. Larsson, S. Stenstrom, B. J. Ohlsson, L. Samuelsson, and L. R. Wallenberg. Solid-phase diffusion mechanism for GaAs nanowire growth. *Nature Materials*, 3(10):677–681, 2004.

[56] K. A. Dick, K. Deppert, T. Martensson, L. Samuelsson B. Mandl, and W. Seifert. Failure of the vapor-liquid-solid mechanism in Au-assisted MOVPE growth of InAs nanowires. *Nano Letters*, 5(4):761–764, 2005.

[57] B. A. Wacaser, K. A. Dick, J. Johansson, M. T. Borgstrom, K. Deppert, and L. Samuelsson. Preferential interface nucleation: An expansion of the VLS growth mechanism for nanowires. *Advanced Materials*, 21(2):153–165, 2009.

[58] C. Y. Wen, J. Tersoff, K. Hillerich, M. C. Reuter, J. H. Park, S. Kodambaka, E. A. Stach, and F. M. Ross. Periodically changing morphology of the growth interface in Si, Ge, and GaP nanowires. *Physical Review Letters*, 107(2):025503, 2011.

[59] Y. C. Chou, K. Hillerich, J. Tersoff, M. C. Reuter, and F. M. Ross K. A. Dick. Atomic-scale variaibility and control of III-V nanowire growth kinetics. *Science*, 343(6168):281–284, 2014.

[60] F. Lenrick, M. Ek, K. Deppert, L. Samuelsson, and L. R. Wallenborg. Straight and kinked InAs nanowire growth observed in situ by transmission electron microscopy. *Nano Research*, 7(8):1188–1194, 2014.

[61] D. Jacobsson, F. Panciera, J. Tersoff, M. C Reuter, S. Lehmann, S. Hofmann, K. A. Dick, and F. M. Ross. Interface dynamics and crystal phase switching in GaAs nanowires. *Nature*, 531(7594):317–322, 2016.

[62] M. E. Messing anf K. Hillerich, J. Joahnsson, K. Deppert, and K. A. Kimberly. The use of gold for fabrication of nanowire structures. *Gold Bulletin*, 42(3):172–181, 2009.

[63] M. C. Plante, J. Garret, S. C. Ghosh, P. Kruse, H. Scriemer, T. Hall, and R. R. LaPierre. The formation of supported monodisperse Au nanoparticles by UV/ozone oxidation process. *Applied Surface Science*, 253(4):2348–2354, 2006.

[64] H-Y. Xu, Y-N. Guo, W. Sun, Z-M. Liao, T. Burgess, H-F. Lu, Q. Gao, h. H. Tan, C. Jagadish, and J. Zou. Quantitative study of GaAs nanowires catalyzed by Au-film of different thicknesses. *Nanoscale Research Letters*, 7(589):1–6, 2012.

[65] K. Hiruma, K. Haraguchi, M. Yazawa, Y. Madokora, and T. Katsuyama. Nanometre-sized GaAs wires grown by organo-metallic vapour-phase epitaxy. *Nanotechnology*, 17(11):S369–S375, 2006.

[66] S. M. Sze. *Semiconductor Devices Physics and Technology*. John Wiley & Sons Inc, 111 River Street, Hoboken NJ 07030, second edition, 2002.

[67] L. E. Smart and E. A. Moore. *Solid State Chemistry test - test - test*. Taylor & Francis Group LLC, 6000 Broken Sound Parkway, NW Suite 300, Boca Raton, FL 33487-2742, third edition, 2005.

[68] P. Caroff, J. Bolinsson, and J. Johansson. Crystal phases in III-V nanowires: From random toward engineered polytypism. *IEEE Journal of Selected Topics in Quantum Electronics*, 17(4):829–846, 2011.

[69] K. A. Dick, P. Caroff, J. Bolinsson, M. E. Messing, J. Johansson, K. Deppert, L. R. Wallenberg, and L. Samuelsson. Control of IIIV nanowire crystal structure by

growth parameter tuning. *Semiconductor Science and Technology*, 25(2 SI):024009, 2010.

[70] C. B. Carter D. B. Williams. *Transmission Electron Microscopy*. Springer Science and Business Media LCC, 233 Spring Street New York, NY, 10013, USA, second edition, 2009.

[71] P. W. Hawkes. The correction of electron lens aberration. *Ultramicroscopy*, 156:A1–A64, 2015.

[72] R. F. Egerton. *Physical Principles of Electron Microscopy An Introduction to TEM, SEM and AEM*. Springer Science+Business Media, Inc., 233 Spring Street, New York, NY 10013, USA, 2005.

[73] H. J. Joyce, Q. Gao, H. H., C. Jagadish, Y. Kim, M. A. Fickenscher, S. Perera, T. B. Hoang, L. M. Smith, H. E. Jackson, J. M. Yarrison-Rice, X. Zhang, and J. Zou. High purity GaAs nanowires free of planar defects: Growth and characterization. *Advanced Functional Materials*, 18(23):3794–3800, 2008.

[74] H. Shtrikman, R. Popovitz-Biro, A. Kretinin, and M. Heiblum. Stacking-faults-free Zinc Blende GaAs nannowires. *Nano Letters*, 9(1):215–219, 2009.

[75] H. Shtrikman, R. Popovitz-Biro, A. Kretinin, L. Houben, M. Heiblum, M. Bukaa, M. Galicka, R. Buczko, and Pera Kacman. Method for suppression of stacking faults in wurtzite III-V nanowires. *Nano Letters*, 9(4):1506–1510, 2009.

[76] G. E. Cirlin, V. G. Dubrowskii, Yu. B. Samsonenko, A. D. Bouravleuv, K. Durose, Y. Y. Proskuryakov, Budhikar Mendes, L. Bowen, M. A. Kaliteevski, R. A. Abram, and Dagou Zeze. Self-catalyzed, pure zincblende GaAs nanowires grown on si(111) by molecular beam epitaxy. *Physical Review B*, 82:035302, 2010.

[77] P. Krogstrup, R. Popovitz-Biro, E. Johnson, M. H. Madsen, J. Nygrd, and H. Shtrikman. Structural phase control in self-catalyzed growth of GaAs nanowires on silicon (111). *Nano Letters*, 10(11):4475–4489, 2010.

[78] D. Spirkoska, Arbiol, A. Gustafsson, S. Conesa-Boj, F. Glas, I. Zardo, M. Heigoldt, M. H. Gass, A. L. Bleloch, S. Estrade, M. Kaniber, J. Rossler, F. Peiro, J. R. Morante, G. Abstreiter, L. Samuelson, and A. Fontcuberta i Morral. Structural and optical properties of high quality zinc-blende/wurtzite gaas nanowire heterostructures. *Physical Review B*, 80(24):245325, 2009.

[79] J. Johansson, J. Bolinsson, Martin Ek, Philippe Caroff, and Kimberly A. Dick. Combinatorial approaches to understanding polytypism in III-V nanowires. *ACS Nano*, 6(7):6142–6149, 2012.

[80] ZY. Lu, Z. Zhang, PP. Chen, SX. Shi, LC. Yao, C. Zhou, XH. Zhou, J. Zou, and W. Lu. Bismuth-induced phase control of GaAs nanowires grown by molecular beam epitaxy. *Applied Physics Letters*, 105(16):162102, 2014.

[81] D. L. Dheeraj, G. Patriarche, H. Zhou, T. B. Hoang, A. F. Moses, S. Grnsberg, A. T. J. van Helvoort, B-O. Fimland, and H. Weman. Growth and characterization of wurtzite GaAs nanowires with defect-free zinc blende GaAsSb inserts. *Nano Letters*, 8(12):4459–4463, 2008.

[82] K. Ikejiri, J. Noborisaka, S. Hara, J. Motohisa, and T. Fukui. Mechanism of catalyst-free growth of GaAs nanowires by selective area MOVPE. *Journal of Crystal Growth*, 298:616–619, 2007.

[83] S. A. Fortuna, JG. Wen, I. S. Chun, and XL. Li. Planar GaAs nanowires on GaAs(100) substrates: Self-aligned, nearly twin-defect free, and transfer-printable. *Nano Letters*, 8(12):4421–4427, 2008.

[84] C. Zhang, X. Miao, P. K. Mohseni, W. Choi, and XL. Li. Site-controlled VLS growth of planar nanowires: Yield and mechanism. *Nano Letters*, 14(12):6836–6841, 2014.

[85] Z. H. Wu, X. Mei, D. Kim, M. Blumin, and H. E. Ruda. Growth, branching, and kinking of molecular-beam epitaxial <110>GaAs nanowires. *Applied Physics Letters*, 83(16):3368–3370, 2003.

[86] GW. Zha, MF. Li, Y. Yu, LJ. Wang, JX. Xu, XJ. Shang, HQ Ni, and ZC. Niu. Strain-driven synthesis of self-catalyzed branched GaAs nanowires. *Applied Physics Letters*, 102(16):163115, 2013.

[87] R. T. Hallberg, S. Lehmann, M. E. Messing, and K. A. Dick. Palladium seeded GaAs nanowires. *Journal of Material Research*, 31(2):175–185, 2016.

[88] Marcus Tornberg, E. K Mrtensson, R. R. Zamani, S. Lehmann, K. A. Dick, and S. G. Ghalamestani. Demonstration of Sn-seeded GaSb homo- and GaAsGaSb heterostructural nanowires. *Nanotechnology*, 27(17):175602, 2016.

[89] R. Sun, N. Vainorius, D. Jacobsson, M-E. Pistol, S. Lehmann, and Kimberly A Dick. Sn-seeded GaAs nanowires grown by MOVPE. *Nanotechnology*, 27(21):215603, 2016.

[90] Y. Nomura, Y. Morishita, S. Goto, Y. Katayama, and T. Isu. Surface-diffusion length of Ga adatoms on (111)b surfaces during molecular-beam epitaxy. *Applied Physics Letters*, 64(9):1123–1125, 1994.

[91] N. J. Kadhim and D. Mukherjee. Growth defects associated with MBE deposited GaAs layers. *Vacuum*, 55(3–4):249–253, 1999.

[92] Alexander M. Whiticar. Alternative seed particles for iii-v nanowire arrays. Master thesis, Copenhagen University, 2016.

[93] J. Johansson, B. A. Wacaser, K. A. Kimberly, and W. Seifert. Growth related aspects of epitaxial nanowires. *Nanotechnology*, 17(11):S355–S361, 2006.

[94] L. E. Froberg, W. Seifert, and J. Johansson. Diameter-dependent growth rate of InAs nanowires. *Physical Review B*, 76(15):153401, 2007.

[95] S. A. Dayeh and S. T. Picraux. Direct observation of nanoscale size effects in Ge semiconductor nanowire growth. *Nano Letters*, 10(10):4032–4039, 2010.

[96] V. G. Dubrovskii. Group V sensitive vapor-liquid-solid-growth of Au-catalyzed and self-catalyzed III-V nanowires. *Journal of Crystal Growth*, 440:62–68, 2016.

[97] J. C. Harmand, G. Patriarche, N. Péré-Laperne, M-N. Mérat-Combes, L Travers, and F. Glas. Analysis of vapor-liquid-solid mechanism in Au-assisted GaAs nanowire growth. *Applied Physics Letters*, 87(20):203101, 2005.

[98] J. Bolinsson, P. Caroff, B. Mandl, and K. A Dick. Wurtzitezincblende superlattices in InAs nanowires using a supply interruption method. *Nanotechnology*, 22(26):265606, 2011.

[99] J. B. Hannon, S. Kodambaka, F. M. Ross, and R. M. Tromp. The influence of the surface migration of gold on the growth of silicon nanowires. *Nature*, 440(7080):69–71, 2006.

[100] M. Tchernycheva, J. C. Harmand, G. Patriarche, L. Travers, and G. E. Cirlin. Temperature conditions for GaAs nanowire formation by Au-assisted molecular beam epitaxy. *Nanotechnology*, 17(16):4025–4030, 2006.

[101] H-Y. Xu, Y-N. Guo, Z-M. Liao, W. Sun, Q. Gao, H. H. Tan, C. Jagadish, and J. Zou. Catalyst size dependent growth of Pd-catalyzed one-dimensional InAs nanostructures. *Applied Physics Letter*, 102(20):203108, 2013.

[102] H. Okamoto. Ag-Ga (silver-gallium). *Journal of Phase Equilibria and Diffusion*, 29(1):111, 2008.

[103] S. G. Ghosh, P. Kruse, and R. R. LaPierre. The effect of GaAs(100) surface preparation on the growth of nanowires. *Nanotechnology*, 20(11):115602, 2009.

[104] V. Grillo. Advances in stem-cell. a free software for tem and stem analysis and simulations: Probe deconvolution in STEM-HAADF. *Microscopy and Microanalysis*, 17(S2):1292–1293, 2011. http://tem-s3.nano.cnr.it/?page_id.

[105] S. Breuer, M. Hilse, A. Trampert, L. Geelhaar, and H. Riechert. Vapor-liquid-solid nucleation of GaAs on Si(111): Growth evolution from traces to nanowires. *Physical Review B*, 82(7):075406, 2010.

[106] S. Breuer, M. Hilse, L. Geelhar, and H. Riechert. Nucleation and growth of Au-assisted GaAs nanowires on gaas(111)b and Si(111) in comparison. *Journal of Crystal Growth*, 323(1):311–314, 2011.

[107] H. J. Joyce, J. Wong-Leung, Q. Gao, H. Hoe Tan, and C. Jagadish. Phase perfection in zinc blende and wurtzite III-V nanowires using basic growth parameters. *Nano Letters*, 10(3):908–915, 2010.

[108] K. A. Dick1, J. Bolinsson, M. E. Messing, J. Johansson S. Lehmann, and P. Caroff. Parameter space mapping of InAs nanowire crystal structure. *Journal of Vacuum Science & Technology B*, 29(4):04D103, 2011.

[109] P. Caroff, K. A. Dick, J.Johansson, M. E. Messing, K.Deppertand, and L.Samuelson. Controlled polytypic and twin-plane superlattices in IIIV nanowires. *Nature Nanotechnology*, 4(1), 2008.

[110] Th. Grap, T. Rieger, Ch. Blömers, Th. Schäpers, D. Grützmacher, and M. I. Lepsa. Self-catalyzed VLS grown InAs nanowires with twinning superlattices. *Nanotechnology*, 24(33):335601, 2013.

[111] K. A Dick, Z. Geretovszky, A. Mikkelsen, L. S. Karlsson, E. Lundgren, J-O. Malm, J. N. Andersen, L. Samuelson, W. Seifert, and B. A. Wacaser. Improving InAs nanotree growth with composition-controlled AuIn nanoparticles. *Nanotechnology*, 17(5):1344–1350, 2006.

[112] J-H. Kang, Y. Cohen, Y. Ronen, M. Heiblum, R. Buczko, P. Kacman, R. Popovitz-Biro, and H. Shtrikman. Crystal structure and transport in merged InAs nanowires MBE grown on (001) InAs. *Nano Letters*, 13(11):5190–5195, 2013.

[113] P. Krogstrup, N. L. B. Ziino, W. Chang, S. M Albrecht, E. Johnson M. H. Madsen, J. Nygard, C. M. Marcus, and T. S. Jespersen. Epitaxy of semiconductor-superconductor nanowires. *Nature Materials*, 14(4):400–406, 2015.

[114] F. Martellia, S. Rubinib, F. Jabeenb, L. Felisarib, and V. Grillo. On the growth of InAs nanowires by molecular beam epitaxy. *Journal of Crystal Growth*, 323(1):297–300, 2011.

[115] S. J. May, J.-G. Zheng, B. W. Wessels, and L. J. Lauhon. Dendritic nanowire growth mediated by a self-assembled catalyst. *Advanced Materials*, 17(5):598–602, 2005.

[116] S. Heun, B. Radha, D. Ercolani, G. U. Kulkarni, F. Rossi, V. Grillo, G. Salviati, F. Beltram, and L. Sorba. Coexistence of vapor-liquid-solid and vapor-solid-solid growth modes in Pd-assisted InAs nanowires. *SMALL*, 6(17):1935–1941, 2010.

[117] K. Sarkar, M. Palit, P. Banerji, S. Chattopadhyay, N. N. Halder, P. Biswas, B. Nagabhusana, and S. Chowdhury. Silver catalyzed growth of $In_xGa_{1-x}As$ nanowires on Si(001) by metal-organic chemical vapor deposition. *CrystEngComm*, 17(44):8519–8528, 2015.

[118] V. Y. Aristov. Electron specroscopy study of noble metal (Au, Cu, Ag)-InAs(110) interfaces at 10-300K. *Physica Scripta*, T39:333–338, 1991.

[119] V. Y. Aristov, G. Le Lay, L. T. Vinh, K. Hricovini, and J. E. Bonnet. Giant band bending induced by Ag on InAs(110) surfaces at low temperature. *Physical Review B*, 47(4):2138–2145, 1993.

[120] C. Mariani. A high-resolution photoemission study of confined metal system on InAs(110). *Surface Science*, 454:417–427, 2000.

[121] O. Akhaven. Silver nanocube crystals on titanium nitride buffer layer. *Journal of Physics D: Applied Physics*, 42(10):105305, 2009.

[122] Y. Suzuki, Y. Ojima, Y. Fukui, H. Fazyia, and K. Sagisaka. Post-annealing temperature dependence of infrared absorption enhancement of polymer on evaporated silver films. *Thin Solid Films*, 515(5):3073–3078, 2007.

[123] YM. Bai, J. Wang, ZG. Yin, NF Chen, XW. Zhang, Z. Fu, JX. Yao, N. Li, HY. He, and MN. Guli. Ag nanoparticles preparation and their light trapping performance. *Science China-Technological Sciences*, 56(1):109–114, 2012.

[124] C. Tong, J. Yun, E. KozarskyWayne, and A. Anderson. Nanoplasmonic enhanced ZnO/Si heterojunction metal-semiconductor-metal photodetectors. *Journal of Electronic Material*, 42(5):889–893, 2013.

[125] H. Nasser, Z. M. Saleh E. Özkol, M. Günoven, A. Bek, and R. Turan. Fabrication of Ag nanoparticles embedded in Al:ZnO as potential light-trapping plasmonic interface for thin film solar cells. *Plasmonics*, 8(3):1485–1492, 2013.

[126] C. G. Granqvist and R. A. Buhrman. Size distribution for supported metal-catalysts - coalescence growth versus ostwald ripening. *Journal of Catalysts*, 42(3):477–479, 1976.

[127] A. K. Datye, Q. Xu, K. C. Kharas, and J. M. McCarty. Particle size distributions in heterogeneous catalysts: What do they tell us about the sintering mechanism? *Catalysis Today*, 111(1–2):59–67, 2006.

[128] C. B. M. Andersson, U. O. Karlsson, M. C Hakansson, L. O. Olsson, L. Ilver, J. Kanski, P. O. Nilsson, and P. E. S. Persson. Sputtered and annealed InAs $\bar{1}\bar{1}\bar{1}$: an unreconstructed surface. *Surface Science*, 307:885–889, 1994.

[129] M. Tchernycheva, L. Travers, G. Patriarche, F. Glas, J.-C. Harmand G. E. Cirlin, and V. G. Dubrovskii. Au-assisted molecular beam epitaxy of InAs nanowires: Growth and theoretical analysis. *Journal of Applied Physics*, 102(9):094313, 2007.

[130] M. H. Madsen, P. Krogstrup, E. Johnson, S. Venkatesan, E. Mühlbauer, C. Scheu, C. B. Sörensen, and J. Nygård. Experimental determination of adatom diffusion lengths for growth of InAs nanowires. *Journal of Crystal Growth*, 364:16–22, 2013.

[131] B. J. Babu and K. Yoh. Effect of As/In-flux on the growth of InAs nanowire by molecular beam epitaxy. *Journal of Crystal Growth*, 323(1):301–303, 2011.

[132] W. Cao and H. E. Elsayed-Ali. Stability of Ag nanoparticles fabricated by electron beam lithography. *Materials Letters*, 63(26):2263–2266, 2009.

[133] J. L. Elechiguerra, L. Larios-Lopez, C. Liu, D. Garcia-Gutierrez, A. Camacho-Bragado, and M. J. Yacaman. Corrosion at the nanoscale: The case of silver nanowires and nanoparticles. *Chemistry of Materials*, 17(24):6042–6052, 2005.

[134] T. W. H. Oates, M. Losurdo, S. Noda, and K. Hinrichs. The effect of atmospheric tarneshing on the optical and structural properties of silver nanoparticles. *Journal of Physics D-Applied Physics*, 46(14):145308, 2013.

[135] S. A. Dayeh, E. T. Yu, and D. Wang. Excess indium and substrate effects on the growth of InAs nanowires. *SMALL*, 3(10):1683–1687, 2007.

[136] V. G. Dubrovskii, N. V. Sibirev, Y. Berdnikov, U. P. Gomes, D. Ercolani, V. Zannier, and L. Sorba. Length distributions of Au-catalyzed and In-catalyzed InAs nanowires. *Nanotechnology*, 27(37):375602, 2016.

[137] Z. Y. Zhou, C. X. Zheng, W. X. Tang, D. E. Jesson, and J. Tersoff. Congruent evaporation temperature of GaAs(001) controlled by As flux. *Applied Physics Letters*, 97(12):121912, 2010.

[138] R. Veresegyhazy, I. Mojzes, and B. Pecz. Comparative mass spectrometic study of A^{III}-B^{V} compounds covered with a gold layer. *Vacuum*, 36(7–9):547–549, 1986.

[139] H. Okamoto. Ag-In (silver-indium). *Journal of Phase Equilibria and Diffusion*, 27(5):536–537, 2006.

[140] J.C. Harmand, M. Tchernycheva, G. Patriarche, L. Travers, F. Glas, and G. Cirlin. GaAs nanowires formed by Au-assisted molecular beam epitaxy: Effect of growth temperature. *Journal of Crystal Growth*, 301:853–856, 2007.

[141] M. C. Plante and R. R. LaPierre. Au-assisted growth of gaas nanowires by gas source molecular beam epitaxy: Tapering, sidewall faceting and crystal structure. *Journal of Crystal Growth*, 310(2):356–363, 2008.

[142] R. Tanta, C. Lindberg, S. Lehmann, J. Bolinsson, M. R. Carro-Temboury, K. A. Dick, T. Vosch, T. Sand Jespersen, and J. Nygård. Raman spectroscopy in the detection of stacking fault density in InAs and GaAs nanowires. To be submitted.

[143] F. J. Lopez, E. R. Hemesath, and L. J. Lauhon. Ordered stacking fault arrays in silicon nanowires. *Nano Letters*, 9:2774–2779, 2009.

[144] I. Zardo, , S. Conesa-Boj, F. Peiro, J. R. Morante, J. Arbiol, E. Uccelli, G Abstreiter, and A. Fontcuberta i Morral. Raman spectroscopy of wurtzite and zinc-blende GaAs nanowires: Polarization dependence, selection rules, and strain effects. *Physical Review B*, 80:245324, 2009.

[145] D. C. Bell, Y. Wu, C. J. Barrelet, S. Gradečak, J. Xiang, B. P. Timko, and C. M. Lieber. Imaging and analysis of nanowires. *Microscopy Research and Technique*, 64(5–6):373–389, 2004.

[146] I. Zardo, G. Abstreiter, and A. Fontcuberta i Morral. Raman spectroscopy on semiconductor nanowires. In P. Prete, editor, *Nanowires*, pages 227–254, 2010.

[147] M. Möller, M. M. de Lima, A. Cantarero, L. C. O. Dacal, J. R. Madureira, F. Iikawa, T Chiaramonte, and M. A. Cotta. Polarized and resonant raman spectroscopy on single InAs nanowires. *Physical Review B*, 84:085318, 2011.

[148] i. Zardo, S. Yazji, N. Hörmann, S. Hertenberger, S. Funk, S. Mangialardo, S. Morkötter, , G. Koblmüller, P. Postorino, and G. Abstreiter. E1(A) electronic band gap in wurtzite InAs nanowires studied by resonant raman scattering. *Nano Letters*, 13:3011–3016, 2013.

[149] N. G. Hörmann, I. Zardo, S. Hertenberger, S. Funk, S. Bolte, M Döblinger, G. Koblmüller, and G. Abstreiter. Effects of stacking variations on the lattice dynamics of InAs nanowires. *Physical Review B*, 84:155301, 2011.

[150] Wang Peng, F. Jabeen, B. Jusserand, J. C. Harmand, and M. Bernard. Conduction band structure in wurtzite gaas nanowires: A resosnant raman scateering study. *Applied Physics Letters*, 100:073102, 2012.

[151] T. Rieger, M. I. Lepsa, Thomas Schäper, and D. Grützmacher. Controlled wurtzite inclusions in self-catalyzed zinc blende III-V semiconductor nanowires. *Journal of Crystal Growth*, 378:506–510, 2013.

[152] F. Jabeen, V. Grillo, S. Rubini, and F. Martelli. Self-catalyzed growth of GaAs nanowires in cleaved Si by molecular beam epitaxy. *Nanotechnology*, 19:275711, 2008.

[153] B. Ketterer, M. Heiss, M. J. Livrozet, A. Rudolph, E. Reiger, and A. Fontcuberta i Morral. Determination of the band gap and the split-off band in wurtzite GaAs using raman and photoluminescence excitation spectroscopy. *Physical Review B*, 83:125307, 2011.

[154] I.H. Campbell and P.M. Fauchet. The effects of microcrystal size and shape on the one phonon raman spectra of crystalline semiconductors. *Solid State Communications*, 58:739–741, 1986.

[155] M. T. Björk L. E. Jensen, S. Jeppesen, A. I. Persson, B. J. Ohlsson, and L. Samuelson. Role of surface diffusion in chemical beam epitaxy of InAs nanowires. *Nano Letters*, 4(10):1961–1964, 2004.

[156] Kimberly A. Dick, Knut Deppert, L. S. Karlsson, W. Seifert, L. R. Wallenberg, and L. Samuelson. Position-controlled interconnected InAs nanowire networks. *Nano Letters*, 6(12):2842–2847, 2006.

[157] B. Mandl, A. W. Dey, J. Stangl, , M. Cantoro, L.-E. Wernersson, G. Bauer, L. Samuelson, K. Deppert, and C. Thelander. Self-seeded, position-controlled InAs nanowire growth on Si: A growth parameter study. *Journal of Crystal Growth*, 334(1):51–56, 2011.

[158] P. Yang, R. Yan, and M. Fardy. Semiconductor nanowire: What's next? *Nano Letters*, 10(5):1529–1536, 2010.

[159] Kimberly A. Dick, Knut Deppert, L. S. Karlsson, W. Seifert, L. R. Wallenberg, and L. Samuelson. Position-controlled interconnected InAs nanowire networks. *Nano Letters*, 6(12):2842–2847, 2006.

Appendix A

Lists over the different samples of Ag-seeded GaAs nanowire growths included in this thesis

Table A.1: First As pressure and and Ga flux test on (100) substrates

Sample	Ag thickness (nm)	Annealing time (min)	Growth T (°C)	As-pressure (Torr)	V/III ratio	Growth time (min)
Qdev130	2	20	400	$1.2 * 10^{-5}$	19	30
Qdev131	2	25	400	$1.2 * 10^{-5}$	25	30
Qdev132	2	20	400	$6 * 10^{-6}$	9	30
Qdev134	2	30	400	$6 * 10^{-6}$	13	30

Table A.2: The samples included in the temperature series on (100) substrates

Sample	Ag thickness (nm)	Annealing time (min)	Growth T (°C)	As-pressure (Torr)	V/III ratio	Growth time (min)
Qdev132	2	20	400	$6 * 10^{-6}$	9	30
Qdev247	1	10	550	$6 * 10^{-6}$	9	30
Qdev216	1	10	575	$6 * 10^{-6}$	9	60
Qdev219	1	10	600	$6 * 10^{-6}$	9	60

Table A.3: The samples included in the temparature series on (111)B substrates

Sample	Ag thickness (nm)	Annealing time (min)	Growth T (°C	As-pressure (Torr)	V/III ratio	Growth time (min)
Qdev168	1	10	400	$6 * 10^{-6}$	9	30
Qdev169	1	10	450	$6 * 10^{-6}$	9	30
Qdev170	1	10	500	$6 * 10^{-6}$	9	30
Qdev247	1	10	550	$6 * 10^{-6}$	9	30
Qdev172	1	10	600	$6 * 10^{-6}$	9	30

Table A.4: The samples included in the As series on (111)B substrates

Sample	Ag thickness (nm)	Annealing time (min)	Growth T (°C	As-pressure (Torr)	V/III ratio	Growth time (min)
Qdev171	1	10	550	$2.4 * 10^{-6}$	4	30
Qdev247	1	10	550	$6 * 10^{-6}$	9	30
Qdev273	1	10	550	$1.2 * 10^{-5}$	19	30

Table A.5: The samples included in the Ga pressure on (100) substrates

Sample	Ag thickness (nm)	Annealing time (min)	Growth T (°C)	As-pressure (Torr)	V/III ratio	Growth time (min)
Qdev330	2	10	T≈ 580	$6 * 10^{-6}$	9	30
Qdev335	2	10	T≈ 580	$6 * 10^{-6}$	8	30

Table A.6: The samples included in the time series on (100) substrates

Sample	Ag thickness (nm)	Annealing time (min)	Growth T (°C)	As-pressure (Torr)	V/III ratio	Growth time (min)
Qdev383	1	10	T≈ 575	$6 * 10^{-6}$	7	4
Qdev384	1	10	T≈ 575	$6 * 10^{-6}$	7	20
Qdev337	1	10	T≈ 575	$6 * 10^{-6}$	7	60

Table A.7: The samples that TEM have been executed on presented in this thesis. The sample marked with * is cooled down without and As overpressure.

Sample	Ag thickness (nm)	Annealing time (min)	Growth T (°C)	As-pressure (Torr)	V/III ratio	Growth time (min)
Qdev178	1	10	600	$6 * 10^{-6}$	9	60
Qdev216	1	10	575	$6 * 10^{-6}$	9	60
Qdev218	1	10	600	$6 * 10^{-6}$	9	60
Qdev266*	1	10	600	$6 * 10^{-6}$	9	45

Appendix B

A list over Ag-seeded InAs nanowire growths

Table B.1: A full list over the growths that has been executed for Ag-seeded InAs nanowires. All annealing have been executed at 550 C except for Qdev248 and Qdev249 which has been annealed at 580 C. Qdev 249 have also been up to 620 C. Samples with both (111)B wafer and (100) wafers have been glued to a GaAs wafer before growth.

Sample	Ag thickness (nm)	Growth T (°C)	As-pressure (Torr)	V/III ratio	Growth time (min)	(111)B	(100)
Qdev211	2	520	$1.5 * 10^{-5}$	30	30	Small NW region	Small NW region
Qdev212	2	470	$1.5 * 10^{-5}$	30	30	No NW	No NW
Qdev213	2	420	$1.5 * 10^{-5}$	30	30	No NW	No NW
Qdev228	2	420	$1.5 * 10^{-5}$	25	60	No NW	Small NW region
Qdev229	2	420	$1.5 * 10^{-5}$	39	60	Small NW region	Small NW region
Qdev229	10	420	$1.5 * 10^{-5}$	39	60	Straight and curly NW:s	-
Qdev230	2	420	$1.5 * 10^{-5}$	61	60	No NW	No NW
Qdev231	2	420	$1.5 * 10^{-5}$	121	60	Small curly NW region	Small curly NW region
Qdev248*	2	500	$1.5 * 10^{-5}$	39	30	No NW	No NW
Qdev249*	2	580	$1.5 * 10^{-5}$	39	30	No NW	No NW
Qdev300	2	420	$7 * 10^{-6}$	18	30	Curly and a few straight NW	-
Qdev301	2	420	$7 * 10^{-6}$	35	30	Mostly curly NW	-
Qdev302	2	370	$1.5 * 10^{-5}$	30	30	Tapered vertical, straight and curly NWs	-
Qdev348	1	445	$1.5 * 10^{-5}$	30	30	Non tapered vertical, straight and curly NW	-
Qdev349	1	420	$1.5 * 10^{-5} As_4$	60	30	Straight and curly NWs	-
Qdev366	0.5	370	$5 * 10^{-6}$	8	30	Tapered vertical, straight and curly NWs	-
Qdev367	2	370	$1.5^{*}10^{-5}$	30	30	Tapered vertical, straight and curly NWs	-
Qdev385	0.5	420	$5^{*}10^{-6}$	8	30	Curly nanowires	-

Appendix C

Annealing of Ag on InAs substrates

Table C.1: Annealing of Ag on InAs substrates

Sample	Substrate orientation	Ag-thickness (nm)	Time T increase (min)	Annealing T °C	Annealing time (min)	As pressure (Torr)
Qdev190	(111)B	10	13	550	0	$1.2 * 10^{-5}$
Qdev191	(111)B	10	12	550	5	$1.2 * 10^{-5}$
Qdev199	(111)B	10	12	550	15	$1.3 * 10^{-5}$
Qdev282	(111)B	2	<60	550	-	$1.5 * 10^{-5}$

Appendix D

Additional Ag-seeded InAs nanowire growths

For the In series presented in D.1 all InAs substrates were glued to GaAs(100) substrates before growth. None of the samples showed nanowire growth all over the substrate; if nanowires did grow it was only on parts of the wafer. Qdev228 has the V/III ratio of 25, Qdev229 has the V/III ratio of 39, Qdev230 has the V/III ratio of 61 and Qdev231 has the V/III ratio of 121. All samples have the high As_2 pressure $1.5 * 10^{-5}$ Torr, a Ag-film thickness of 2 nm, a growth temperature of 420°C and have been annealed at 550°C for 2 min. In figure D.1 each growth is represented with four images, two for each wafer. The top image shows the area with nanowire growth, the bottom image shows the area without nanowire growth. As mentioned earlier we believe that the reason for nanowire growth on only a small part of the sample is due to insufficient removal of the oxide. After this In series either a higher annealing temperature of 580°C was used (Qdev248 and Qdev249) or growth was executed on full quarter wafers in order to avoid such problems. All samples with full quarter wafers show consistent results throughout the sample. Assuming that the nanowire growth regions are Ag-seeded InAs where the oxide have disappeared, Figure D.1 shows that straight nanowires grow with at least the V/III ratio between 25 and 36. From sample E (Qdev213) we also know that straight nanowires grow for the V/III ratio of 30. When the V/III ratio is increased to 121 (Qdev231) almost only curly nanowires grow. So with a high As_2 pressure a lack of In occurs for at least the high V/III ratio of 121. Due to the lack of nanowire growth on Qdev230 it is impossible to say anything about the V/III ratio of 61. While instead looking at the wafer structure there is a difference in the trend between the InAs(111)B and InAs(100) wafers. All (111)B wafers show triangular structures. For the lowest V/III ratio of 25 to the higher V/III ratio of 39 the roughness of the surface increases. When increasing the V/III ratio even more to 61 the roughness disappears and instead a smooth surface with apparent triangles appear. Increasing V/III ratio further to 121 causes the density of the triangles to decrease even more. Thus there is a peak in the surface roughness for Qdev229 at the V/III ratio of 39. Instead looking at the (100) wafers another trend is shown. For the low V/III ratio of 25 quite large rectangular pits appear. For each increase of the V/III ratio the rectangular pits become smaller and occure at a higher density.

For Qdev229 a (111)B substrate with a 10 nm thick Ag-film was also grown, see figure D.2. For this sample all three kinds of nanowires (inclined, vertical and curly) were

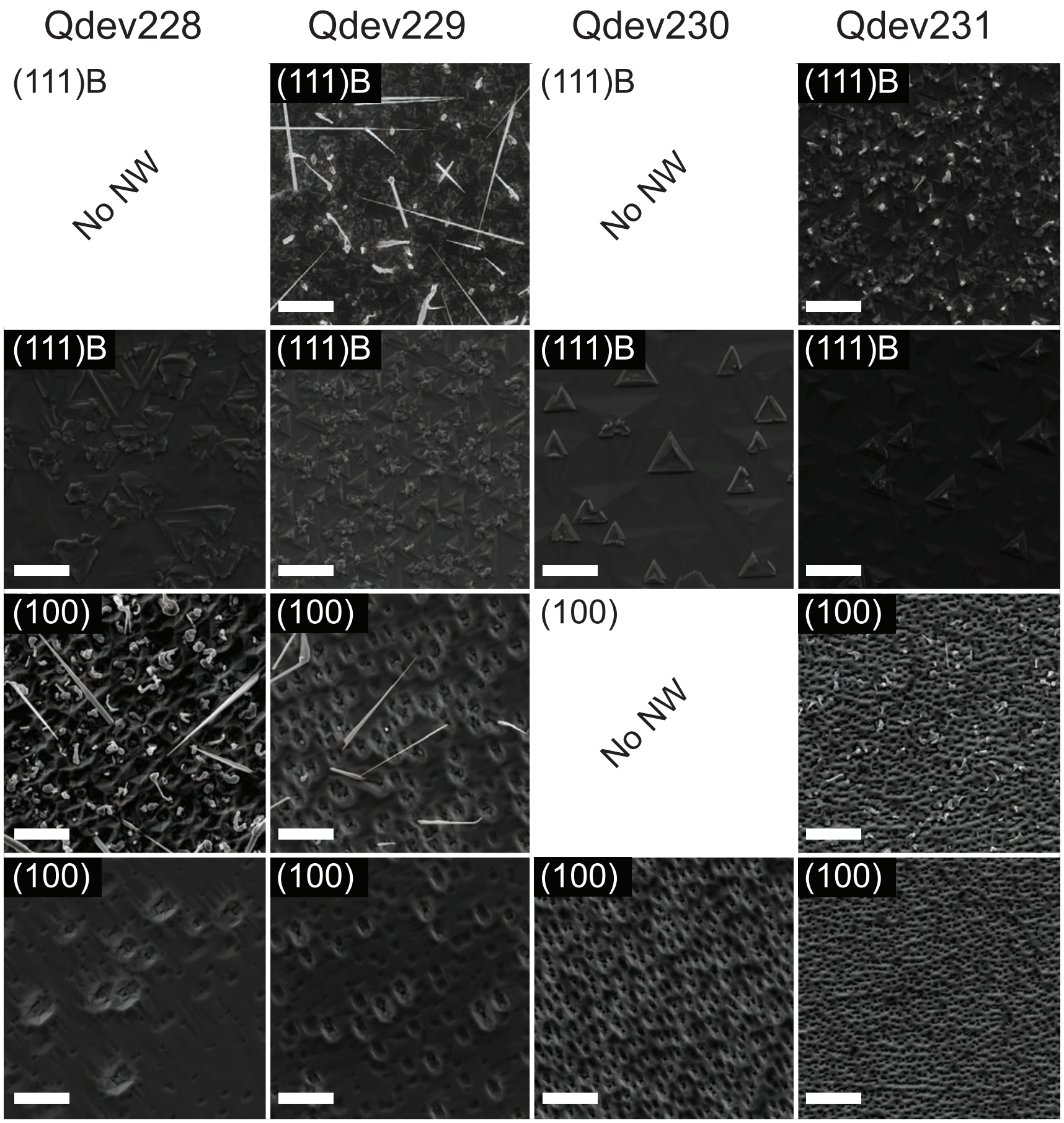

Figure D.1: Images from the In series, most samples are not included in the presentation above. Qdev228 have the V/III ratio of 25, Qdev 229 have the V/III ratio of 39, Qdev 230 have the V/III ratio of 61 and Qdev131 have the V/III ratio of 121. All samples are grown with a high As_2 pressure at $1.5 * 10^{-5}$ Torr. For each sample four images are presented, two images for each wafer. The two upper images show the (111)B wafer and the two lower images show the (100) wafer. The upper of those two images shows the area where nanowire growth occurs, if nanowires exist. The lower image shows an area without any nanowires. All scalebars are 5μm. In this series the two lower V/III ratios of 25 and 39 yield straight nanowires. At 61 unfortunately there is no nanowire growth at all. At the extreme V/III ratio of 121 mostly curly nanowires grow.

present on all parts of the sample covered with Ag.

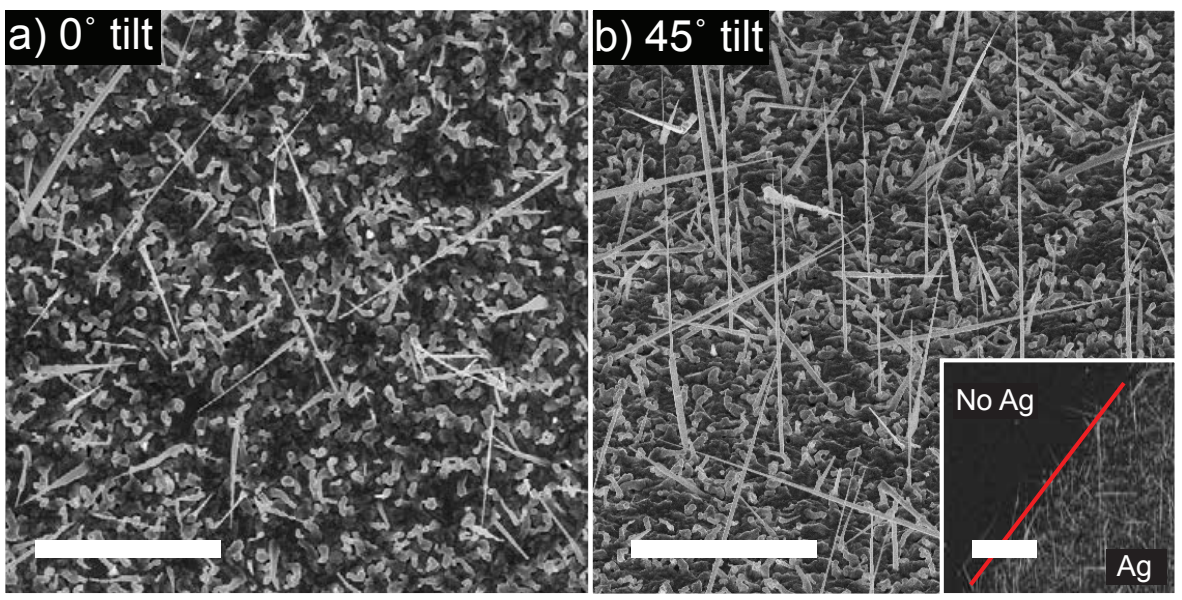

Figure D.2: shows Qdev229 with 10 nm Ag deposited before growth. This sample shows all three kinds of nanowires (curly, inclined and vertical) all over the sample where Ag has been deposited. a) shows a top view image, b) shows 45° tilt, inset in b) shows the difference between an area deposited with Ag and an area without Ag. No growth of nanowires occurs where Ag has not been deposited. The scalebars in a) and b) are 10μm while the scalebar in the inset is 20 μm.

Appendix E

Car temperature versus pyrometer temperature

In order to use the MBE when the pyrometer was down a relation between the pyrometer temperature and the car temperature was calculated. This was done for one single sided polished wafer and three double sided polished wafers (one for each of the holders 3, 4 and 5). The single sided polished wafer had the specification SWI-8753 and the double side polished wafer had the specification SWI-8211-2, both from Semiconductor Wafer Inc. The graph labeled "all values" in Figure E.1 take all measured points into account. The graph labeled "selected values" is only based on the values where the pyrometer has been allowed to stabilise.

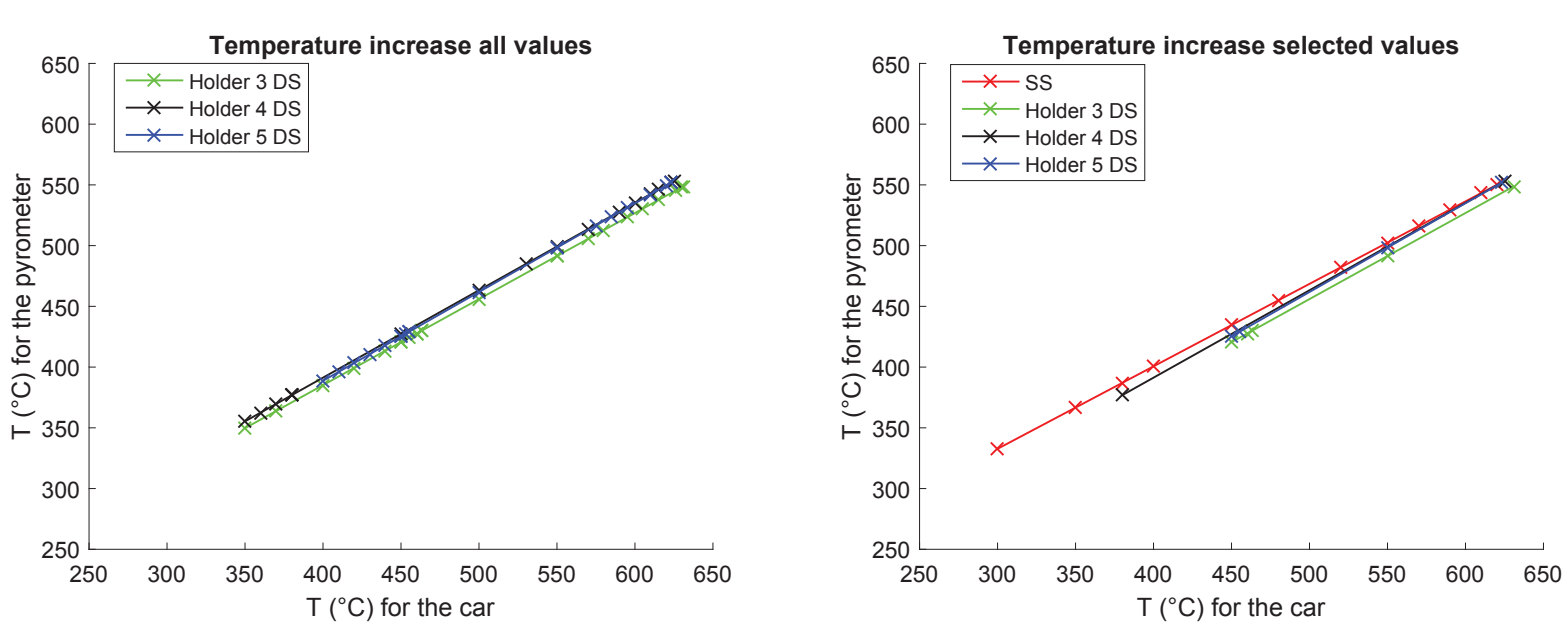

Figure E.1: Temperature calibration for one single sided polished (111)B InAs wafer (red line) and a temperature calibration for the MBE holders 3, 4 and 5 for double sided polished InAs wafers (blue, green and black).

Table E.1: Calculated temperature relation between the car and the pyrometer, k and m are the extracted values for the linear regressions. The different values at 370, 420, 550 and 570 are the calculated values for the different holders.

Sample	k	m	370°C	420°C	550°C	570°C
SS selected	0.68	129	355	429	620	649
Holder 3	0.71	102	379	449	621	661
Holder 3 selected	0.76	71	393	459	622	656
Holder 4	0.72	103	370	440	633	648
Holder 4 selected	0.74	90	379	446	630	649
Holder 5	0.73	96	374	443	648	648
Holder 5 selected	0.75	84	383	450	649	651

Table E.2: Summary for the temperature relation between the car and the pyrometer. The columns show the intervals between the different wafers and the different holder for the double sided substrates.

	370°C	420°C	550°C	570°C	diff 370°C	diff 420°C	diff 550°C	diff 570°C
Summary	370-379	440-449	621-633	649-656	8	9	12	7
Summary selected	379-393	622-630	622-633	648-661	14	12	7	13

Appendix F

EBL recipe

This Appendix presents the EBL recipe used to prepare the patterned substrates in Chapter 5.

F.1 Spinning of resist

1. Spin resist Nano^{TM} 6% copolymer from Micro Chem on the substrate with the speed of 4000 rpm for 45 s.
2. Bake substrate at hot plate 185°C for 90 s.
3. Spin resist Nano^{TM} 2% PMMA (polymethyl methacrylate) from Micro Chem on the substrate with the speed of 4000 rpm for 45 s.
4. Bake substrate at 185°C for 90 s.

F.2 Illumination of the sample

1. Exposure of the sample was done in a Raith eLINE system from Raith Nanofabrication.

F.3 Development

1. Develop substrate in MIBK:IPA 1:3 for 45 s.
2. Rinse in two IPA baths.
3. Check that pattern look good.

F.4 Deposition of metal

1. The sample is ashed in a costum buildt microwave to remove resist residues at the developed areas. The asher was set to remove 10 nm of resist.
2. The sample is soaked in buffered HF for 10 s to remove native oxide and rinsed in two water baths.
3. Blow dry substrate with nitrogen. 4. The sample is directly loaded into a custom made AJA electron beam evaporation chamber with a thermionic gun for deposition of

metal.

F.5 Lift off

1. Lift off in 60°NMP for 55 min
2. Rinse in a new NMP beaker at 60°
3. Rinse in acetone
4. Rinse in Methanol
5. Rinse in IPA
6. Blow dry with nitrogen

"New opinions are always suspected, and usually opposed, without any other reason but because they are not already common"

– John Locke